

Non-contact AFM and STM
studies of molecular systems on
weakly interacting surfaces

Can't touch this!

Cover: Photo of the bottom of the (old) cryostat including radiation shields.

Printed by: BOXPress || proefschriftmaken.nl

ISBN: 978-94-6295-334-5

Non-contact AFM and STM studies of molecular systems on weakly interacting surfaces

Can't touch this!

Contactloze AFM en STM studie van moleculaire systemen op oppervlakken met zwakke wisselwerking

Verboden aan te raken!

(met een samenvatting in het Nederlands)

Proefschrift

ter verkrijging van de graad van doctor aan de Universiteit Utrecht op gezag van de rector magnificus, prof.dr. G.J. van der Zwaan, ingevolge het besluit van het college voor promoties in het openbaar te verdedigen

op woensdag 23 maart 2016

des middags te 12.45 uur

door

Joost van der Lit

geboren op datum 21 maart 1986 te Bilthoven

Promotor: Prof.dr. D.A.M. Vanmaekelbergh

Copromotor: Dr. I. Swart

And then the man, he steps right up to the microphone

And says at last just as the time bell rings

‘Goodnight, now it’s time to go home’

Table of Content

1.	Introduction	9
2.	The design and construction of a liquid nitrogen cryostat	23
3.	Sub-molecular resolution imaging of molecules by AFM: Pauli versus Coulomb	31
4.	Suppression of electron-vibron coupling in graphene nanoribbons contacted via a single atom	43
5.	Bending and buckling of narrow armchair graphene nanoribbons via STM manipulation	57
6.	Modelling the self-assembly of organic molecules on weakly interacting surfaces	65
7.	Summary	81
	Samenvatting in het Nederlands	84
	List of publications	88
	Acknowledgements	90

1

Introduction

1.1 General introduction

The visualization of atoms in real space is one of the most remarkable achievements of Scanning Tunneling Microscopy (STM) and Atomic Force Microscopy (AFM) [1–6]. These techniques rely on an atomically sharp probe tip to interact with a sample below. A large variety of tip-sample interactions can nowadays be measured. Frequency modulated AFM (FM-AFM), a branch of non-contact AFM [7] is a technique that is specifically suited in sensing forces at the (sub)atomic scale. It is this technique, combined with STM, that play a central role in this thesis.

The development of new materials requires a detailed understanding of the relation between the atomic and electronic structure of the molecules or crystals under investigation. The push towards smaller devices has led to a limit where active elements in machines or devices can be the size of single molecules [8–10] or have a thickness of a single atomic layer [11]. In such systems one atom can really make a difference. In chemistry, small atomic catalytic clusters play an important role in the production of, for instance, (synthetic) fuels [12,13]. The exact shape of these clusters determine, to a large extent, their catalytic activity. It is thus vital to know the exact atomic structure of a material to understand its properties.

Atomically well-defined surfaces and interfaces are a key aspect of nearly all nanoscale devices and in heterogeneous catalysis. Techniques, such as XPS, Auger, LEED, SERS and other, can selectively probe interfacial properties. However, many of these techniques lack the high spatial resolution required to study individual molecules or clusters. One way of obtaining a detailed understanding of the atomic structure of a surface or processes taking place at an interface is through the combination of FM-AFM and STM [14]. The first is able to resolve the atomic structure of many atomically flat materials, including individual molecules, while the second gives direct access to local electronic properties. In this thesis I explore the relation between the atomic structure and electronic properties of molecules on weakly interacting metal surfaces using high resolution STM and FM-AFM at cryogenic temperatures.

This thesis is roughly divided in three parts. The first part describes work that furthers the understanding of the contrast forming mechanism of sub-molecular AFM. This work helps to exploit the potential of FM-AFM in the future by showing the importance of the electrostatic force component for the imaging contrast.

In the next part of this thesis, it is shown how one atom can make a difference in the electronic properties of a technological relevant material. Semi conducting armchair terminated graphene nanoribbons (GNR) are grown on an atomically flat gold surface. The atomic structure of the GNR is verified by atomically resolved FM-AFM. Subsequently, by controllably removing a single hydrogen atom, the electronic properties are modified. This change is measured by combined AFM and STM measurements, before and after the modification. In the next chapter, the GNR are bend and buckled to investigate the stability of the electronic properties under strain. This research impacts the possible application of these materials in future electronics.

In the final part of this thesis, the self-assembly of small molecules on weakly interacting surfaces is investigated using STM combined with Monte Carlo simulations. 2D molecularly functionalized surfaces have tunable properties useful in catalysis, electronics

and protection against chemicals [15]. A model is provided that can predict the experimentally observed structures and quantify their thermodynamic stability.

1.2 Outline of this thesis

In the second chapter of this thesis the fabrication of an improved liquid nitrogen (LN_2) tank for our low temperature STM/AFM will be presented. Details about the construction and design are discussed. In the third chapter, the impact of the electrostatic force contribution on the contrast in FM-AFM images of molecules is investigated. Some context for this work will be given in paragraph 1.5 since the work relates to a recent debate on the interpretation of AFM images.

The fourth and fifth chapter describe combined AFM/STM work that I performed on atomically precise armchair graphene nanoribbons (ac-GNR). These chapters describe the influence of various kinds of manipulations on the electronic structure of this material. Specifically, the fourth chapter deals with the effects associated with creating atomic contacts to macroscopic leads. The fifth chapter describes the influence of bending and buckling of the ac-GNR, using the tip of the STM.

Chapter six presents work done on assemblies of molecules on a weakly interacting metal surface. A molecular mechanics model that allows for the accurate prediction of different (meta)stable phases of these molecules on a surface is described. The 2D molecular phases that we observe are discussed in terms of their thermodynamic stability.

1.3 The Scanning Tunneling Microscope

The scanning tunneling microscope is based on the quantum mechanical tunneling of electrons between a tip and a substrate electrode. In the 1920's tunneling was put forward as the reason behind alpha decay of atoms and is described as the ability of a particle to penetrate a classically forbidden region. The first electron tunneling current was measured in a metal-insulator-metal device in 1960 by Giaever [16]. However, it took until 1982 for Binnig, Rohrer, Gerber and Weibel to realize a microscope based on electron tunneling through a vacuum gap [4,17]. Their efforts led to a Nobel prize in 1986 [18].

The theoretical background of the tunneling phenomenon will not be discussed here. Instead, the reader is referred to available textbooks [19,20]. It will suffice to show some important results from the derivations in these texts. The first and most important result is the exponential dependance of the electron tunneling current over a vacuum gap with distance. The tunneling current falls off exponentially between two electrodes (tip and surface) with a decay constant κ of $\sim 1 \text{ \AA}^{-1}$ according to

$$I = I_0 \text{Exp}(-\kappa d) \quad (1.1).$$

The decay constant κ increases with increasing barrier height of the tunneling barrier and depends on the work function of the material that is is being probed. The exponential dependence of the tunneling current implies that when the tip-surface distance d is increased by one Ångstrom, the tunneling current decreases 10-fold.

The most common mode of STM operation is called 'constant current mode' and this is what is typically referred to when 'an STM image' is shown. Atomically resolved images of a surface can be obtained by raster scanning an atomically sharp STM tip over a sample

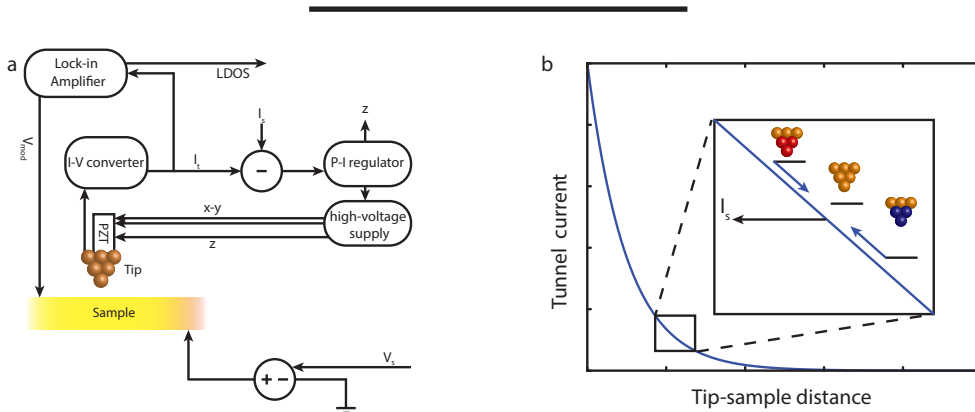


Figure 1.1. a. Schematic of the STM feedback regulator. A bias is applied to the sample and the current through the tip is amplified. The current signal is fed to a comparator that generates an error signal. The error signal gets passed through a P-I regulator to drive the z-piezo via the high voltage supply. The high-voltage supply also provides signals for the xy-scanning motion. The current signal can also be fed to the lock-in amplifier to measure the dI/dV signal. b. Tunneling response as a function of distance showing the exponential dependance. Inset illustrates the response of the tip to an increase/decrease in tip-sample distance resulting in a correction to maintain I_s .

while using a regulator to maintain a constant current by adjusting the tip height. Typical currents that are used in STM are between 10 fA and 100 nA. The schematic of a typical STM setup is shown in figure 1.1a. The STM tip is connected to a piezo tube (PZT), which produces the xyz scanning movement with sub-atomic precision. The tunneling current is amplified $10^7 - 10^{13}$ times by an operational-amplifier (op-amp) in order to be processed. The op-amp converts the current to a voltage that is compared to the reference current set point, I_s , which is also expressed as a voltage. The error signal is input to a proportional-integral (P-I) regulator that controls the tip-sample distance via the piezo elements. The regulator will reduce the 'error' by adjusting the scanner z position. This regulation is straight forward since the current to distance response is monotonic, meaning the current will always increase when the distance decreases (fig. 1.1b). Not all scanning probe microscopes (SPM's) have a monotonic response with respect to distance as will be shown later. The speed at which the tip can be scanned over the surface depends, among many things, on the response time of the P-I regulator.

A second important relation is that between the tunneling current at a given voltage and the density of states of the tip and the surface,

$$I(V) \propto \int_{E_f}^{eV} \rho_{tip}(E_f + \epsilon) \rho_{sample}(E_f - eV + \epsilon) |M_{ts}|^2 d\epsilon \quad (1.2)$$

The tunneling current (I) is dependent on the density of states (DOS) of tip (ρ_{tip}) and sample (ρ_{sample}), weighted by the tunneling matrix (M_{ts}). The latter is adopted from Bardeen [21] and describes the orbital overlap between all the states involved in the tunneling process. The bias, eV , is applied to the sample, shifting its Fermi level with respect to that of the tip (fig. 1.2a). The total current is an integral over all available states between E_f and the applied bias V . One of the assumptions that is made by Bardeen is to take ρ_{tip} as a constant. Hence, provided that ρ_{tip} is constant over the energy range of interest, one can directly probe the local density of states (LDOS) of the sample by recording the differential

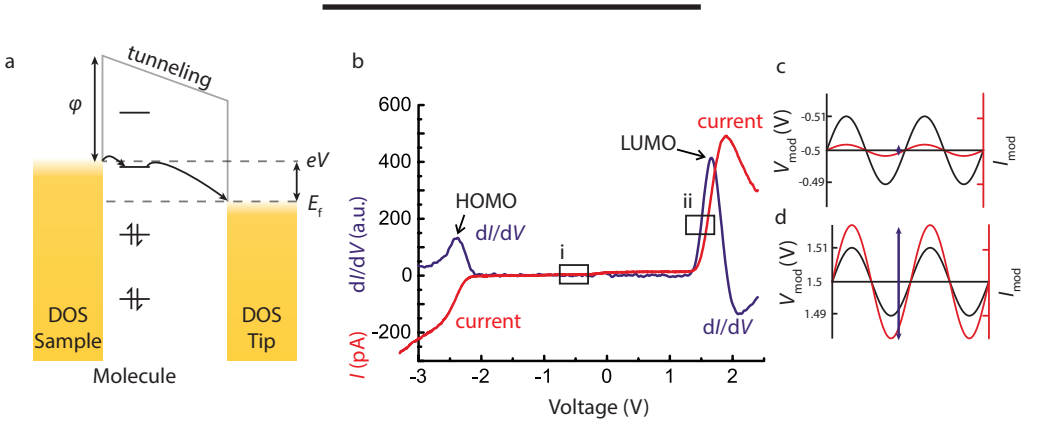


Figure 1.2. a. The schematic of a double barrier tunneling junction. A molecule placed on a surface provides additional tunneling pathways that can be probed using STS. b. $I(V)$ and corresponding $dI/dV(V)$ curve recorded over a pentacene molecule on Cu(111)/2ML NaCl. HOMO and LUMO state are visible as peaks in the dI/dV . c. A graph showing the V_{mod} (10 mV) applied by the LA around -0.5 V (position i in a) and the corresponding I_{mod} . The LA output is proportional to amplitude of I_{mod} (blue arrow). d. same as c, but for position ii at 1.5 V. Since the $I(V)$ is increasing here a larger I_{mod} is detected. The spectrum in b is taken from [22].

conductance (dI/dV) at a constant tip-sample distance as a function of voltage (fig 1.2b, left). These kinds of measurements are called Scanning Tunneling Spectroscopy (STS). In case of a clean metal surface an STS measurement gives a linear, Ohmic, response in a bias window smaller than the workfunction of the surface. In this thesis, the main focus is on the electronic properties of molecules adsorbed on the surface. The energy levels of a molecule in the tip-surface junction are probed in a similar fashion. Once the potential of the sample becomes equal to or greater than that of filled/empty state of the molecule, electrons tunnel resonantly, causing an increase in the current.

The energy levels of a molecule can be disturbed by chemical bonding to the substrate. To avoid this, weakly interacting surfaces should be used when measuring the properties of individual molecules. This is typically done by placing molecules on a Au(111) surface or surfaces covered by a thin insulating film [22–29]. As a result, the intrinsic molecular orbitals of an individual molecule can be probed using STM. Consequently, electrons experience an extra potential barrier between the molecule and sample. The tip/molecule/surface system can be seen as a double barrier tunnel junction. Electron transport can now result in (temporary) charging of a molecule, which needs to be taken into account when interpreting the position of the energy levels of individual molecules on a surface.

STS is typically performed during a STM experiment using lock-in techniques to increase the signal to noise ratio. Briefly, a lock-in amplifier (LA) produces a bias oscillation (V_{mod}) that induces a current modulation (I_{mod}) in the tip-sample junction. The modulating current signal, which is phase shifted with respect to the output V_{mod} , is input to the LA and results in an output signal that is proportional to dI/dV (the actual output is the amplitude of I_{mod}). For most STS spectra recorded in this thesis, a V_{mod} with an amplitude of 15 mV and a frequency (f_{mod}) < 300 Hz is used. The f_{mod} has to be smaller than the bandwidth of the STM op-amp to prevent attenuation of the signal. An example of a typical $I(V)$ and corresponding $dI/dV(V)$ curve is shown in figure 1.2b. To illustrate the working principle of the LA, I will compare the current modulation in response to a V_{mod} of the $I(V)$ curve at -0.5 V (fig. 1.2c) and 1.5 V (fig. 1.2d). The amplitude of the current modulation at -0.5 V will be small since the $I(V)$ curve is flat in this region. However, at 1.5 V, when almost in resonance with an electronic state of a molecule, $I(V)$ is very steep leading to a large current modulation. The LA output is proportional to the I_{mod} amplitude (vertical arrow in figure 1.2c/d) and can be plotted as function of bias to give an STS spectrum showing the electronic states of a molecule (fig. 1.2b. blue curve).

The combination of STS and STM is a key element in this thesis. It enables visualization of the spatial extent of an electronic state related to the local atomic configuration. This is done by recording the intensity of the LA output as function of position at a given bias. This can be done in constant current or constant height mode. The first enables easy imaging of large, corrugated structures due to the inclusion of a feedback mechanism. However, considering the complex relation between tip-sample distance, current, LDOS and the P-I regulator, a constant current measurement might result in the imaging of artifacts. An example relevant for this thesis is shown in figure 1.3. The images are acquired at a bias voltage corresponding to tunneling through the Highest Occupied Molecular Orbital (HOMO) on the end of a narrow strip of graphene placed on Au(111). Figure 1.3a was recorded in constant current mode, while figure 1.3b was acquired in constant height mode. The 3 \AA height step when going from the surface onto the graphene in constant current mode results in features at the edges of the ribbon that are not trivial to relate to the spatial extension of the HOMO. For this reason all the STS maps, or dI/dV maps, in this thesis are

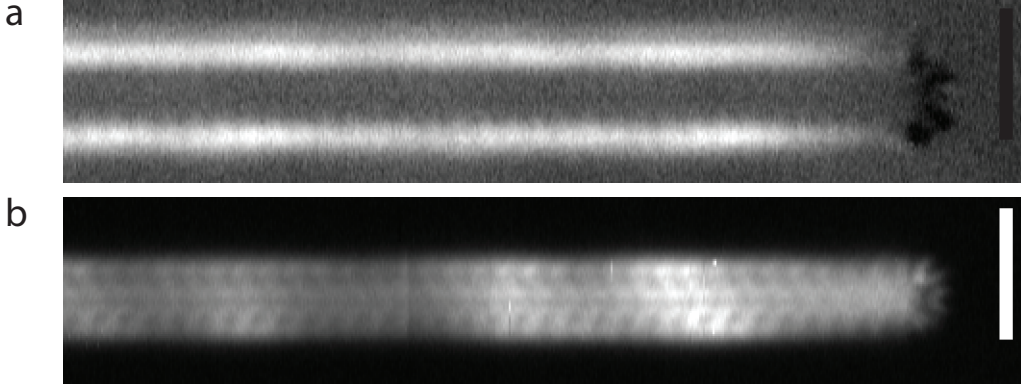


Figure 1.3. a. Spatially mapped dl/dV signal of GNR at -0.8 V in constant current mode. b. Same as (a), but recorded in constant height mode. $V_{\text{mod}}(714 \text{ Hz}, 10 \text{ mV}_{\text{rms}})$, scale bar 1 nm .

recorded at a constant height above the sample.

1.4 The Atomic Force Microscope

One of the major drawbacks of STM is the requirement of (semi)-conducting samples. In addition, atomic resolution is not always possible since an STM measurement is only sensitive to the LDOS of a surface or sample, which does not necessarily represent its atomic structure. An alternate method was proposed based on using the forces the tip experiences while in close proximity to the surface as a feedback signal. Due to the more complex nature of the problem it took until 1986 for the first AFM to be build [5].

The first AFM was operated by dragging a tip, attached to a soft cantilever, over a surface. The deflection of the cantilever was measured by placing a STM needle on top of the AFM cantilever. This mode of operation is referred to as contact-mode. Later, the deflection of the cantilever was measured using a laser beam that is reflected off the cantilever onto a detector. Because of many reasons, the most important being the large influence the tip has on the surface while in contact-mode, dynamic AFM modes were soon developed [5,7]. In these, the cantilever is deliberately oscillated at its resonance frequency in close proximity to, but not in contact with, the surface. For this reason, dynamic AFM is also referred to as non-contact AFM (nc-AFM). The forces gradient $\delta F_{ts}/\delta z$ acting on the cantilever and tip oscillating perpendicular to the surface result in a shift of its resonance frequency (Δf) [30] according to

$$\Delta f = -\frac{f_{\text{res}}}{2k} \frac{\delta F_{ts}}{\delta z} \quad (1.3)$$

f_{res} and k are the resonance frequency and stiffness of the free cantilever, and A the oscillation amplitude. $\langle F_{ts} \rangle$, the average force per oscillation cycle, is calculated by integrating dF_{ts}/dz (the force gradient) over one oscillation. The two main branches of nc-AFM are frequency modulated AFM (FM-AFM) [7] and amplitude modulated AFM (AM-AFM) [6]. In AM-AFM a change in oscillation amplitude at f_{res} due to the shifting of the resonance frequency is used as measure for tip-sample interactions. In FM-AFM the Δf is directly measured by subtracting the measured frequency from f_{res} during an experiment. FM-AFM

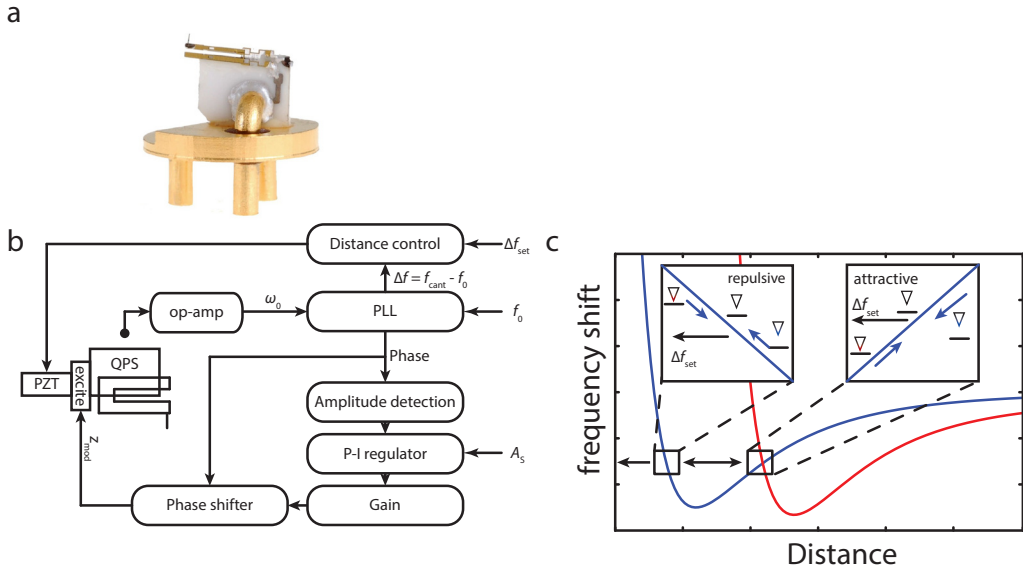


Figure 1.4. a. qPlus sensor mounted on tip holder for Omicron LT-STM/AFM. b. Schematic of the FM-AFM QPS controller system. The QPS generates a current modulation at its resonance frequency. After amplification, this signal, ω_0 , is sent to a PLL for phase and frequency detection. The Δf is used for height regulation in a manner similar to that of STM. The phase signal is used for the oscillation amplitude detection and subsequent regulation to the reference value (A_s). After appropriate attenuation of the resulting signal, a 90° phase shifter will feed the signal back to the z-mod piezo element. Image adopted from the manual of the LT-STM/AFM by Scienta Omicron GmbH.

is the best technique to use in vacuum where cantilever quality factors (Q) are typically high [7].

The choice of oscillation amplitude, A , in eq 1.3 is dependent on the forces that one is interested in [31]. In short, the oscillation amplitude has to be of the same length as the extend of the force. The total force between tip and sample consists of many components, e.g. van der Waals attraction, Pauli repulsion, electrostatic forces, magnetic forces, etc. All of these forces have their own associated length scale. Because in this thesis intra- and inter-molecular interactions are of importance, it requires probing of the repulsive Pauli force [3,32]. This force is caused by the Pauli exclusion principle, which states that no two electrons can occupy the same quantum state. As a consequence, when the electrons of the tip and sample are squeezed together they get forced into (very) high energy states. Pauli repulsion forces are very short range (on the order of an atomic bond length) and thus require small amplitudes to be accurately probed, $A = \sim 1 \text{ \AA}$. To operate in this amplitude regime the cantilever stiffness needs to be very high in order to maintain a stable oscillation.

The requirement mentioned above is met in the qPlus sensor (QPS) design [33]. It is constructed from a quartz tuning fork commonly found in wristwatches (fig. 1.4a). One of the prongs is attached to a (macor) support while the other serves as a holder for any kind of tip. Its high stiffness ($k = 1800 \text{ N m}^{-1}$) allows for stable oscillation, even at sub-Ångstrom

amplitudes. In addition, quartz is a piezoelectric material, meaning that structural deformations (oscillations) result in a surface polarization, allowing for all-electronic determination of the cantilever amplitude and oscillation frequency. If a conducting tip material is chosen STM measurements can be performed simultaneously. Since typical STM op-amp bandwidths, when measuring small currents (<100 pA), are <300 Hz only the average tunneling current during an AFM oscillation will be detected.

In a typical FM-AFM measurement, the Δf is used as a feedback signal, this method is referred to as constant- Δf . The experimental setup is very similar to that of the STM but contains some additional features (fig. 1.4b). The QPS is excited using a small piezo element (Z_{mod} in fig. 1.4b) close to the QPS. The resulting cantilever oscillation, which generates a small oscillating current, is amplified and converted to an oscillating voltage (ω_o) that is fed into a Phase Locked Loop (PLL). The function of the PLL is to keep the phase difference between the input and excitation signals constant. This allows for accurate amplitude measurements (like in a LA) and regulation to a set point amplitude (A_s) via a P-I regulator. In addition, the PLL provides the demodulated cantilever frequency signal for the z-regulator. The z-regulator has two branches in FM-AFM because the tip-sample force can be both attractive and repulsive (non-monotonic behavior) depending on the tip-sample distance (fig. 1.4c, blue). Typically, the tip-sample force follows the well-known Lennard-Jones type curve. At large separations the attractive van der Waals (vdW) force is dominant, while at small separations the repulsive Pauli force dominates. Since the slope of $dF_{ts}(z)/dz$ and hence $\Delta f(z)$ is opposite in both these regimes, the response of the regulator to the error signal has to be reversed (insets fig. 1.4c). Note that since $\Delta f(z)$ is proportional to dF_{ts}/dz even at positive Δf (with negative slope) the total force can still be attractive. However, due to the inversion of the slope these regions are always referred to as ‘the attractive and repulsive regime’.

In the molecular structures that are studied in this thesis the constant- Δf feedback cannot be used. The reason for this is the large difference between tip-sample interactions when moving from a typical metal surface onto a molecule or vice versa. As an example: when a tip is scanned over a metal surface in the attractive regime and it experiences an increase in Δf , the feedback mechanism will decrease the tip-sample distance (fig. 1.4c, blue curve, right inset). Over the molecule, the minimum of the L-J curve is located further away from the surface (fig. 1.4c, red curve). Hence, when the tip starts to scan over the molecule, the sudden change in the tip-sample force may result in an effective transfer to the repulsive branch. The tip response to an increase in Δf is to approach, resulting in an immediate tip-crash over the molecule. For this reason, all the FM-AFM data shown in this thesis is recorded in constant-height mode, i.e. without height regulation.

1.5 Contrast mechanism of sub-molecular atomic force microscopy

In the following, results obtained on molecules with FM-AFM using chemically passivated tips are discussed. Mainly, I will focus on the contrast forming mechanism as it provides background useful for chapter three.

In 2009, a paper by Gross et al. was published in which it was shown that the chemical structure of molecules can be resolved with sub-molecular resolution using FM-AFM [3]. Figure 1.5a shows a constant-height Δf AFM image of pentacene recorded with a CO terminated tip. The 2 key requirements to obtain such images of essentially unperturbed molecules are: (1) the use of chemically passivated tips, and, (2) the use of small oscillation

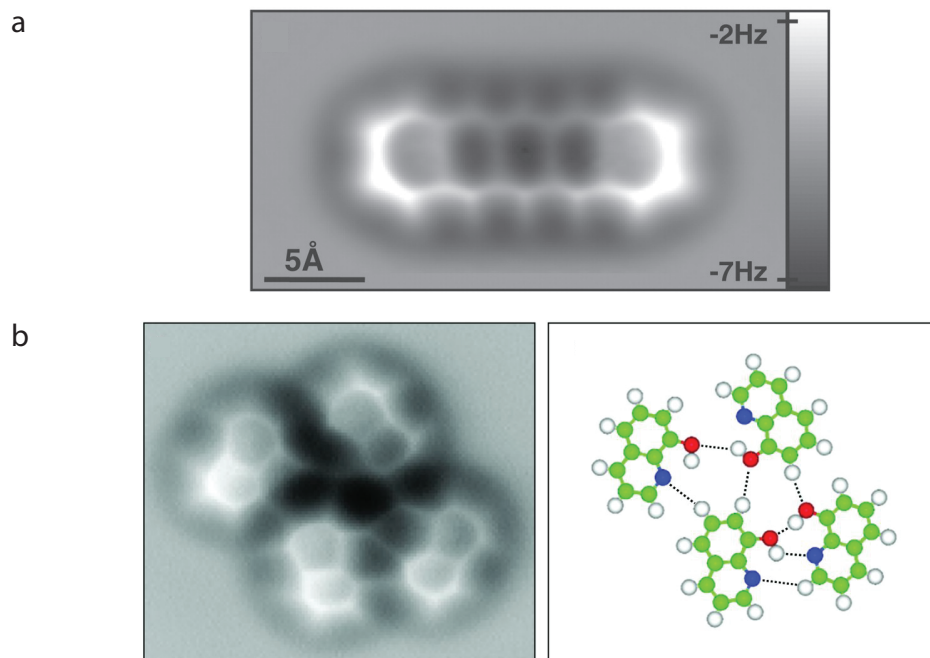


Figure 1.5. a. Constant height Δf image of pentacene recorded with a CO terminated tip. Constant height Δf image of four 8-hydroxyquinoline showing inter molecular contrast recorded with a CO terminated tip. Images taken from [3] and [44].

amplitudes. The reason for using small amplitudes has already been discussed. Because Pauli repulsive force are responsible for the observed contrast on pentacene very small tip-sample distance have to be used. To prevent that the molecules jump from the surface to the tip, chemical passivation is required. Initially, CO passivated tips were used, partly because information was available on how to prepare such tips [34].

Since 2009 several papers have appeared showing sub-molecular resolution on molecules [10,35–41]. In addition to the experimental work, a theoretical understanding of the observed AFM contrast was developed [42]. In the pentacene system the molecule could only be imaged in the Pauli repulsion regime. A clear attractive vdW background (‘the vdW pit’) was measured above pentacene at large distances (negative Δf , attractive regime, black). Only when the tip was brought closer did the atoms appear in a more repulsive contrast (higher Δf but still negative, repulsive regime, white). It was concluded that the sub-molecular contrast was determined by the Pauli repulsion between the electrons of tip and the molecule. The Pauli repulsion contrast will dominate in regions of high electron density, as was proposed by Moll et al. [43,42]. In 2013 Zhang et al. showed AFM images featuring intermolecular contrast, which they interpreted as hydrogen bonds (fig. 1.5b) [44]. Zhang et al. propose that the electron density in the hydrogen bonds is responsible for the intermolecular contrast. This statement is highly controversial since hydrogen bonds are predominantly electrostatic in origin and are thus not expected to contain a lot of electron density.

As more and more AFM images of individual molecules appeared in the literature, it became apparent that the molecules looked distorted [10,35–41]. This distortion is attributed to the flexibility of the CO molecule at the tip apex [43,45,46]. This flexibility was measured by extracting the lateral force experienced by the tip following literature procedures to convert $\Delta f(x,y,z)$ to $F(x,y,z)$ [47–49]. Using these lateral forces the real position of the atoms inside a molecule could be determined. In an attempt to obtain a better understanding of the influence of the tip flexibility, some groups developed simple molecular mechanics models (AFMulators) to account for the tip bending [32,45,46,50]. AFMulators give the possibility to probe, for instance, the influence of CO bending stiffness on the AFM contrast, something that is not easily done in ab-initio DFT calculations. In addition, AFMulators are computationally far less expensive than DFT. The AFMulator used in the work presented in this thesis drastically simplifies the tip-sample junction (fig. 1.6a) [51]. The CO molecule that is attached to the tip, oxygen atom pointing towards the sample, is modeled as a single particle (the so-called probe particle). The carbon atom and the bulk tip are not taken into account since these will only result in an additional vdW background. The force between the tip and the molecule is calculated as a sum over L-J type interactions between the final tip atom and the atoms of the molecule. The bending of the final oxygen atom is modeled by a spring-mass on a sphere. Subsequently, the final tip atom is allowed to relax its position in accordance with these forces. This relaxation is done for many positions above the molecule resulting in a complete $F(x,y,z)$ dataset. This dataset can be converted to Δf to plot 2D slices of data representing the actual experiment [49].

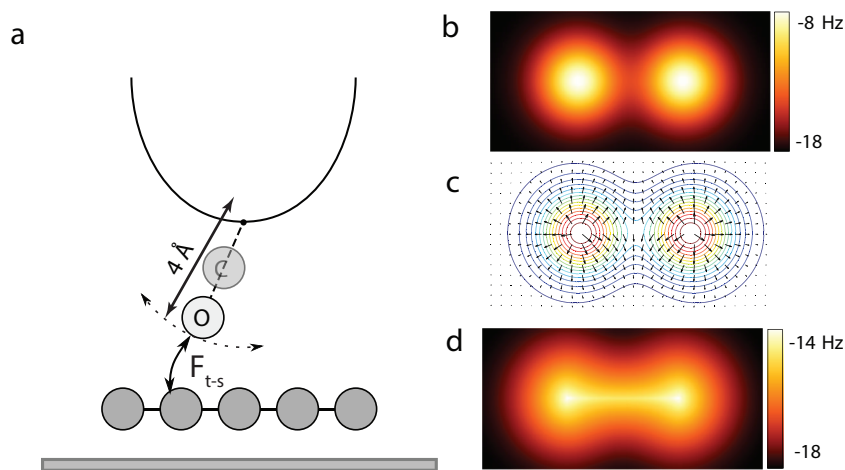


Figure 1.6. a. schematic of the AFMulator model. The only tip atom that is interacting with the sample is the final oxygen atom. This is allowed to relax when moved over the potential energy landscape of the molecule below. b. calculated Δf image of two atoms as two protrusions with an infinitely stiff CO tip, i.e. the oxygen atom does not relax. c. the lateral force component over two atoms with the saddle point in between the two atoms. d. calculated Δf image of two atoms as two protrusions connected by a 'bond'. The stiffness of the tip is set to 0.5 N/m.

In the beginning of 2014 these kind of calculations were able to reproduce the experimental Δf images of pentacene with intramolecular bonds (fig. 1.5a) without actually incorporating the bonds in the model [45]. This result was followed by Hapala et al., who went on to show that even inter-molecular contrast (fig. 1.5b) can be explained by tip relaxations [50]. This conclusion put the observation of “hydrogen bonds” under debate. Finally, at the end of 2014, we showed that inter-molecular contrast can be observed between two adjacent atoms that do not form a hydrogen bond [32]. This proved that not all contrast features observed in Δf images can be directly interpreted as bonds.

From the model it was concluded that whenever two atoms are placed close together a signature similar to that of a bond will appear in the Δf image. To better explain this, let us look at some simple cases. A single atom that is probed by a rigid tip will show as a bump in the $F(x,y)$ plots due to the Pauli repulsion when the tip is close by. Two nearby atoms will show as two bumps in $F(x,y)$ when probed with a rigid tip (fig. 1.6b). The force the final atom experiences at every point above the molecule can be divided into a perpendicular and a lateral component. The lateral component of the force, potted in figure 1.6c, will cause the tip to bend. As a consequences, a saddle point in the force between two atoms will become more pronounced and appear as a ‘bond’ in the Δf (fig. 1.6d). An accurate understanding of the forces between tip and sample are thus of great importance in understanding the sub-molecular contrast observed in FM-AFM.

1.6 References

- [1] G. Binnig, H. Rohrer, C. Gerber, and E. Weibel, *Phys. Rev. Lett.* 50, 120 (1983).
- [2] F. J. Giessibl, *Science* 267, 68 (1995).
- [3] L. Gross, F. Mohn, N. Moll, P. Liljeroth, and G. Meyer, *Science* 325, 1110 (2009).
- [4] G. Binnig, *Appl. Phys. Lett.* 40, 178 (1982).
- [5] G. Binnig, C. F. Quate, and C. Gerber, *Phys. Rev. Lett.* 56, 930 (1986).
- [6] G. Binnig, C. Gerber, E. Stoll, T. R. Albrecht, and C. F. Quate, *Europhys. Lett.* 3, 1281 (1987).
- [7] T. R. Albrecht, P. Grütter, D. Horne, and D. Rugar, *J. Appl. Phys.* 69, 668 (1991).
- [8] J. Henzl, P. Puschnig, C. Ambrosch-Draxl, A. Schaate, B. Ufer, P. Behrens, and K. Morgenstern, *Phys. Rev. B* 85, (2012).
- [9] B. L. Feringa, *Acc. Chem. Res.* 34, 504 (2001).
- [10] F. Mohn, J. Repp, L. Gross, G. Meyer, M. Dyer, and M. Persson, *Phys. Rev. Lett.* 105, (2010).
- [11] A. H. Castro Neto, N. M. R. Peres, K. S. Novoselov, and A. K. Geim, *Rev. Mod. Phys.* 81, 109 (2009).
- [12] J. D. Aiken and R. G. Finke, *J. Mol. Catal. A Chem.* 145, 1 (1999).
- [13] H. Jahangiri, J. Bennett, P. Mahjoubi, K. Wilson, and S. Gu, *Catal. Sci. Technol.* 4, 2210 (2014).
- [14] E. I. Altman, M. Z. Baykara, and U. D. Schwarz, *Acc. Chem. Res.* 48, 2640 (2015).
- [15] J. V Barth, G. Costantini, and K. Kern, *Nature* 437, 671 (2005).
- [16] I. Giaever, *Phys. Rev. Lett.* 5, 147 (1960).
- [17] G. Binnig, H. Rohrer, C. Gerber, and E. Weibel, *Phys. Rev. Lett.* 49, 57 (1982).
- [18] G. Binnig and H. Rohrer, *Rev. Mod. Phys.* 59, 615 (1987).
- [19] C. J. Chen, *Introduction to Scanning Tunneling Microscopy* (2008).
- [20] J. Tersoff and D. R. Hamann, *Phys. Rev. Lett.* 50, 1998 (1983).
- [21] J. Bardeen, *Phys. Rev. Lett.* 6, 57 (1961).
- [22] J. Repp, G. Meyer, S. Stojković, A. Gourdon, and C. Joachim, *Phys. Rev. Lett.* 94, 026803 (2005).
- [23] W.-H. Soe, C. Manzano, A. De Sarkar, N. Chandrasekhar, and C. Joachim, *Phys. Rev. Lett.* 102, 176102 (2009).
- [24] J. van der Lit, M. P. Boneschanscher, D. Vanmaekelbergh, M. Ijäs, A. Uppstu, M. Ervasti, A. Harju, P. Liljeroth, and I. Swart, *Nat. Commun.* 4, 2023 (2013).
- [25] B. Schuler, G. Meyer, D. Peña, O. C. Mullins, and L. Gross, *J. Am. Chem. Soc.* 137, 9870 (2015).
- [26] F. Schulz, M. Ijäs, R. Drost, S. K. Hämäläinen, A. Harju, A. P. Seitsonen, and P. Liljeroth, *Nat. Phys.* 11, 229 (2015).
- [27] P. Järvinen, S. K. Hämäläinen, M. Ijäs, A. Harju, and P. Liljeroth, *J. Phys. Chem. C* 118, 13320 (2014).
- [28] N. Pavliček, I. Swart, J. Niedenführ, G. Meyer, and J. Repp, *Phys. Rev. Lett.* 110, 136101 (2013).

- [29] P. Liljeroth, I. Swart, S. Paavilainen, J. Repp, and G. Meyer, *Nano Lett.* 10, 2475 (2010).
- [30] F. J. Giessibl, *Phys. Rev. B* 56, 16010 (1997).
- [31] F. J. Giessibl, H. Bielefeldt, S. Hembacher, and J. Mannhart, *Appl. Surf. Sci.* 140, 352 (1999).
- [32] S. K. Hämäläinen, N. van der Heijden, J. van der Lit, S. den Hartog, P. Liljeroth, and I. Swart, *Phys. Rev. Lett.* 113, 186102 (2014).
- [33] F. J. Giessibl, *Appl. Phys. Lett.* 73, 3956 (1998).
- [34] L. Bartels, G. Meyer, and K. H. Rieder, *Appl. Phys. Lett.* 71, 213 (1997).
- [35] L. Gross, F. Mohn, N. Moll, G. Meyer, R. Ebel, W. M. Abdel-Mageed, and M. Jaspars, *Nat. Chem.* 2, 821 (2010).
- [36] F. Mohn, L. Gross, and G. Meyer, *Appl. Phys. Lett.* 99, 053106 (2011).
- [37] O. Guillermet, S. Gauthier, C. Joachim, P. de Mendoza, T. Lauterbach, and A. Echavarren, *Chem. Phys. Lett.* 511, 482 (2011).
- [38] N. Pavliček, B. Fleury, M. Neu, J. Niedenführ, C. Herranz-Lancho, M. Ruben, and J. Repp, *Phys. Rev. Lett.* 108, 086101 (2012).
- [39] L. Gross, F. Mohn, N. Moll, B. Schuler, A. Criado, E. Guitian, D. Pena, A. Gourdon, and G. Meyer, *Science* 337, 1326 (2012).
- [40] F. Albrecht, M. Neu, C. Quest, I. Swart, and J. Repp, *J. Am. Chem. Soc.* 135, 9200 (2013).
- [41] D. G. de Oteyza, P. Gorman, Y.-C. Chen, S. Wickenburg, A. Riss, D. J. Mowbray, G. Etkin, Z. Pedramrazi, H.-Z. Tsai, A. Rubio, M. F. Crommie, and F. R. Fischer, *Science* 340, 1434 (2013).
- [42] N. Moll, L. Gross, F. Mohn, A. Curioni, and G. Meyer, *New J. Phys.* 14, 083023 (2012).
- [43] N. Moll, L. Gross, F. Mohn, A. Curioni, and G. Meyer, *New J. Phys.* 12, 125020 (2010).
- [44] J. Zhang, P. Chen, B. Yuan, W. Ji, Z. Cheng, and X. Qiu, *Science* 342, 611 (2013).
- [45] M. P. Boneschanscher, S. K. Hämäläinen, P. Liljeroth, and I. Swart, *ACS Nano* 8, 3006 (2014).
- [46] Z. Sun, M. P. Boneschanscher, I. Swart, D. Vanmaekelbergh, and P. Liljeroth, *Phys. Rev. Lett.* 106, 046104 (2011).
- [47] M. Neu, N. Moll, L. Gross, G. Meyer, F. J. Giessibl, and J. Repp, *Phys. Rev. B* 89, 205407 (2014).
- [48] M. Ternes, C. P. Lutz, C. F. Hirjibehedin, F. J. Giessibl, and A. J. Heinrich, *Science* 319, 1066 (2008).
- [49] F. J. Giessibl, *Appl. Phys. Lett.* 78, 123 (2001).
- [50] P. Hapala, G. Kichin, C. Wagner, F. S. Tautz, R. Temirov, and P. Jelínek, *Phys. Rev. B* 90, 085421 (2014).
- [51] <https://github.com/ProkopHapala/ProbeParticleModel>

2

The design and construction of a liquid nitrogen tank

OLD



NEW



In this chapter I will describe the new liquid nitrogen (LN_2) tank we build for the cryostat of our low temperature microscope. I will start by explaining briefly why we needed a new LN_2 tank and motivate our design choices. Next, I will compare the calculated heat load in the original and new LN_2 tank design to obtain an estimate for the hold time. Last, I will compare the STM noise level of the microscope with the different cryostats. The manufacturer of the low temperature microscope (Omicron GmbH[1]) has expressed interest in commercializing our new LN_2 tank. For this reason only relative improvements with respect to the old cryostat are made.

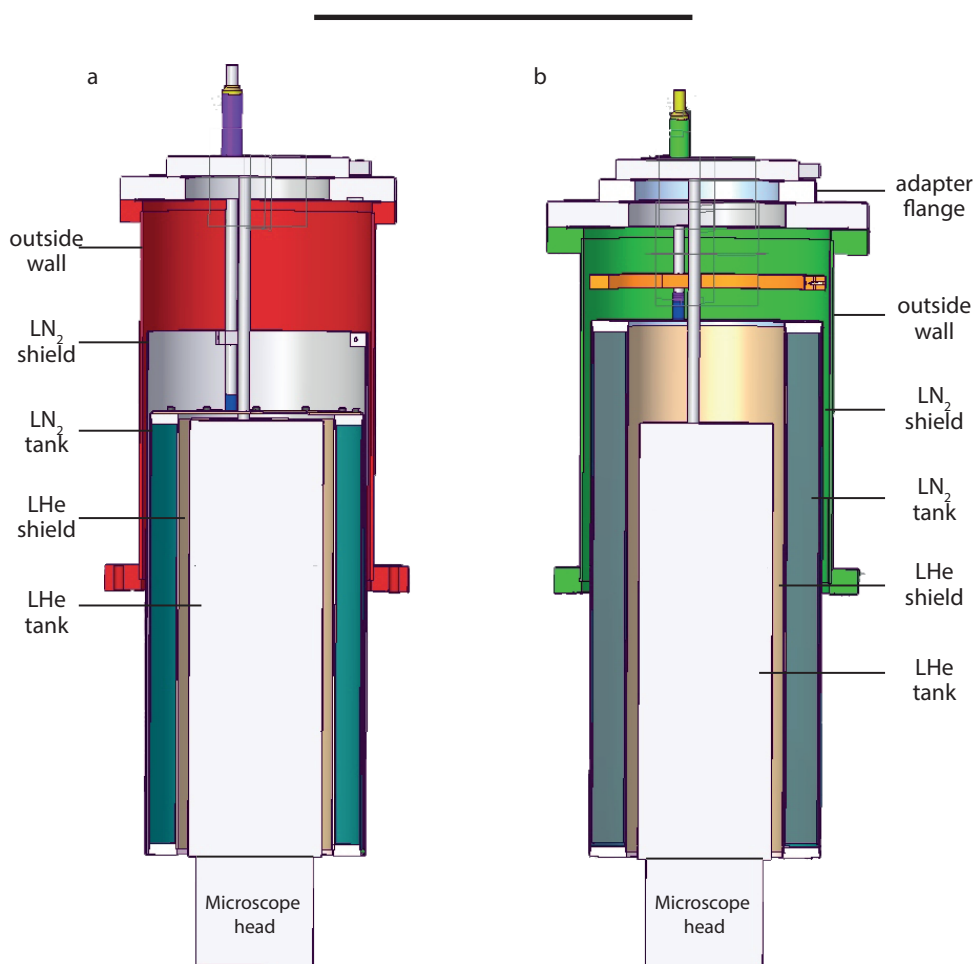


Figure 2.1 A cut through the Omicron LT-STM/AFM double Dewar cryostat. In reality the LHe/ LN_2 tanks are round. a. old cryostat, b. new cryostat. Starting from the outside going in: outer wall (300 K), LN_2 shield (~ 100 K), LN_2 tank (77.3 K), LHe shield (~ 20 K, not shown), LHe tank (4.2 K). All tanks are suspended in the vacuum via three 120° offset tubes (inlet, outlet, sensor). Microscope is placed below LHe tank (not shown).

2.1 Introduction

Our commercial low-temperature STM/AFM microscope has a double Dewar design (fig. 2.1a). The inner liquid helium (LHe) tank is placed inside a LN₂ tank with vacuum in between. The purpose of this is to reduce the radiation heat impinging on the LHe tank, thus increasing the LHe hold time. To further reduce the heat load on the LHe tank, reflective radiation shields are present between the outer vacuum vessel and LN₂ tank and between the LN₂ and LHe tanks. The first is connected to the inlet/outlet/sensor tubes of the LN₂ tank whereas the latter is connected to the tubes of the LHe tank. The original LN₂ tank has a hold time of roughly 48 hours, which is more than 6 hours shorter than the hold time of the LHe. After all LN₂ has evaporated, the heat load on the LHe tank increases, resulting in an increased evaporation rate of the LHe. Hence, the overall hold time – and therefore the amount of measurement time – is limited by the LN₂ tank. The effective measurement time is further reduced by the slow warming up of the LN₂ tank: this results in a measurable increase of the temperature of the microscope head by approx. + 0.1 K, causing additional lateral drift during measurements. These two factors, combined with the finding that the original LN₂ tank has a small cryo-leak, led us to design and built a new LN₂ tank.

2.2 Design requirements:

The overall cryostat should fulfill the following requirements.

1. The new cryostat should allow easier and safer maintenance. The original cryostat is difficult to disassemble without damaging the thin electrical wires controlling the microscope that run along the outside of the LHe tank. The main reason for this is that the diameter of the hole in the top flange of the LN₂ tank is too small to fit the LHe tank including radiation shield through (fig. 2.2a). Disassembling the cryostat meant removing the LHe shield while the LHe tank was still located in between the LN₂ and LHe tank. Since the space between the two tanks is on the order of a centimeter, disassembling the cryostat carried a significant risk (for reference, see the cover of this thesis).
2. The new LN₂ tank should be compatible with our existing setup, i.e. with the LHe tank and the vacuum chamber (fig. 2.2b). This provides several boundary conditions:
 - The inner diameter should not be smaller than the original design in order to fit the LHe tank.
 - The outer diameter, including radiation shield, should be smaller than the bore of the port-aligner that connects the cryostat to the rest of the vacuum system.
 - The vertical position of the LHe tank, mounted on the top flange of the LN₂ tank, should not change in order to maintain access to the microscope.
3. The overall hold time of the cryostat should be limited by the evaporation rate of LHe.
4. The cryostat should be UHV compatible. Leak rate < 10⁻¹⁰ mbar L/s.

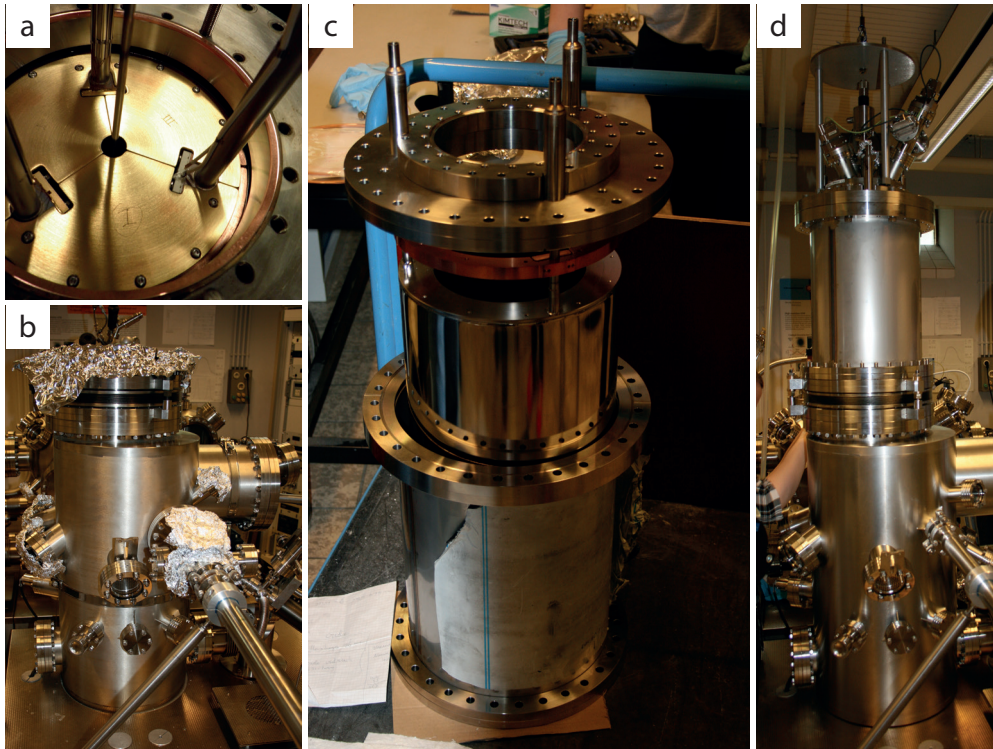


Figure 2.2 a. Bore of the old LN₂ tank top flange with LHe tank + shield lifted up. LHe tank does not fit through the bore with the shield mounted. b. Main vacuum chamber before mounting the cryostat. c. new LN₂ tank standing in the vacuum vessel (without LN₂ shield). The zero-length reducer is mounted on the top flange. d. Setup without electronics after mounting cryostat containing the new LN₂ tank.

2.3 Implementation

I will discuss our approach to meet the design requirements point by point, where I combine our solution to maintain compatibility with the LHe tank together with improving the serviceability.

Maintaining compatibility with the existing equipment: As indicated above, the flange from which the LN₂ tank is suspended should be able to accommodate the top flange of the LHe tank. At the same time, the free bore of this flange should increase to allow us to lift the LHe tank including radiation shield out of the LN₂ tank. This was achieved by introducing a zero-length reducer flange between the flanges on which the LN₂ and LHe tanks are suspended and moving the LN₂ tubes outward (fig. 2.1b and 2.2c). To keep the vertical position of the LHe tank constant, the height of the vacuum vessel holding the cryostat is reduced by the height of the zero-length reducer flange. Finally, the outer diameter of the LN₂ tank, including radiation shield, was chosen to be a few mm smaller than the free bore diameter of the port aligner (13" flange) that connects the cryostat to the rest of the vacuum chamber.

Increasing the hold time of the cryostat: In general, there are two ways to increase the hold time of a cryostat. First by increasing the volume of LN₂ and second by minimizing the heat load onto the LN₂ tank. The latter would result in a decreased evaporation rate. We increased the outer diameter as well as the height of the tank, resulting in a total volume available for LN₂ of 14.13 L. The original tank had a volume of 8.4 L. Hence, the volume is increased by almost 70%.

In addition, we aimed to minimize the heat load onto the cryostat. Under UHV conditions, we only need to consider heat transfer via radiation and thermal conduction. In the following I will calculate the differences in the heat transfer between the old and new cryostat.

Thermal energy is transferred to the LN₂ via the three tubes (inlet, outlet, and sensor) from which the tank is suspended. In the steady state, the amount of thermal energy transferred through a rod via conduction ($Q_{\text{conduction}}$) can be calculated using eq 2.1 [1]:

$$Q_{\text{conduction}} = \kappa(\Delta T) \frac{A}{L} \quad (2.1),$$

where κ is the heat conductivity of the material in [W K⁻¹ m⁻¹], ΔT the temperature difference between the two ends in [K] and A and L are the area and length through which the heat has to flow in meters. The suspension tubes of the LN₂ tank in the old and new design are constructed from stainless steel (316), which has a κ value of 16.3 at room temperature. The expected temperature gradient is also the same for the old and new tank, $\Delta T = 300 - 77.3 = 222.7$ K. The only difference is in the A/L ratio. Because the new LN₂ tank is higher, the tubes will be shorter. To compensate for the smaller L , we decreased the thickness of the tubes, resulting in a smaller A . The calculated heat through the old/new tubes is 1.0 / 0.7 W, i.e. the heat load due to thermal conduction should be approximately 33% lower for the new tank.

As estimate of the power transferred via radiation ($Q_{\text{radiation}}$) can be obtained by using the Stefan-Boltzmann equation eq 2.2:

$$Q_{\text{radiation}} = \sigma \epsilon A T^4 \quad (2.2).$$

Where ϵ is the emissivity of the object, A its surface area, T the temperature, and σ the Stefan-Boltzmann constant ($5.67 \cdot 10^{-8}$ W/(m² K⁴)). By definition, the emissivity of a surface is the percentage of emitted light w.r.t. a true black body of the same temperature. The emissivity is a material property that strongly depends on surface treatment. For example, cold rolled steel has an emissivity of 75-85% while after polishing it can be as low as 7%. In general, the lower the emissivity of a surface, the less heat it will absorb or emit according to Kirchhoffs law [2]. The total heat flow between two random shaped objects at a different temperature is given by eq 2.3 [1]:

$$Q_{\text{radiation}} = A_c \sigma \frac{\Delta T^4}{\frac{1}{\epsilon_c} + \frac{1}{\epsilon_h - 1} \frac{A_c}{A_h}} \quad (2.3).$$

Here, the indices c and h refer to the cold and hot object. ΔT^4 is defined as ($T_h^4 - T_c^4$) because the heat will flow from the hot to the cold object. Because of the complex shape of the cryostat only some of the surfaces will be take into account in order to simplify the calculation. Only heat transfer from the vacuum chamber (300 K) to the LN₂ tank (77-100 K) will be taken into account. The largest surfaces of the LN₂ tank subjected to thermal radiation

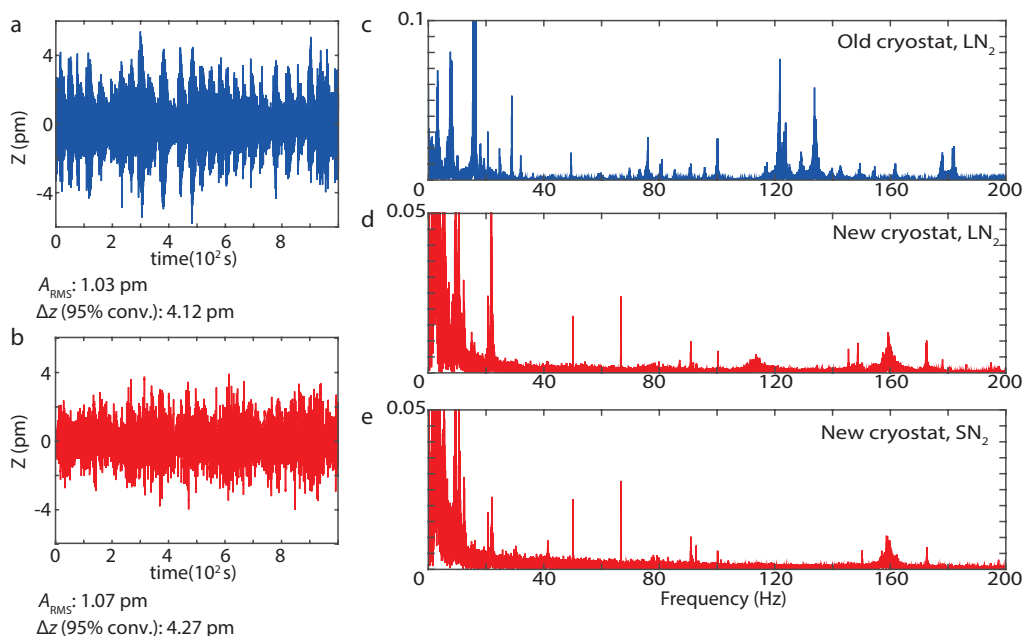


Figure 2.3 a-b. the tip-sample distance as a function of time, $z(t)$, graphs before and after installation of the new LN_2 tank. The height stability has not been affected by the installation of the new tank as can be seen from the A_{rms} values. c. Frequency spectrum of $z(t)$ before installation of the new LN_2 tank. d. Frequency spectrum of $z(t)$ after installation of the new LN_2 tank. e. Frequency spectrum of $z(t)$ (not shown) after installation of the new LN_2 tank, with solid nitrogen (SN_2). Tunneling set points: 1% loop-gain, 0.1 V, I (old/new) 2.5 nA/ 50 pA, τ (old/new) 2.5/ 1 ms.

are the LN_2 shield, LN_2 top plates and the LN_2 cup housing the microscope. As a first approximation I will only take these surface into account. All surfaces have been treated in order to have a low emissivity, e.g. the LN_2 cup has a gold coating to reducing its emissivity to $\sim 4\%$. Using equation 2.3, and the appropriate values of ϵ for all surfaces, we estimate that the heat load on to the new LN_2 tank due to radiation will be approximately 15.3 W, somewhat larger than for the original tank, 13.1 W. This increase is easily understood because of the larger height and outer diameter of the new tank.

Hence, the total heat load on the old and new LN_2 tank is 14.1 W and 16.0 W, respectively. As stated above, the amount of LN_2 in the tank has increased from 8.4 L to 14.1 L. The total amount of energy needed to evaporate all the LN_2 can be calculated using its heat of evaporation (5.56 kJ/mol). We find 2.615 MJ and 4.398 MJ for the old and new tank respectively. Using the estimate of the total heat load given above, the hold time of the LN_2 cryostats should be 51 h and 76 h, respectively. Hence, the hold time of the new LN_2 tank should be 50% larger than that of the old tank. The experimentally determined hold time of the original cryostat was approximately 48 hours, suggesting that the estimates given above are reasonable.

2.4 Performance

Hold time: The new LN₂ tank was placed into the cryostat and mounted into the vacuum chamber in June 2015 (fig. 2.2d). The hold time of the LN₂ tank is measured after filling the cryostat with LHe and LN₂. The hold time of the cryostat was determined after the cryostat had been cold for more than 2 days. After refilling both LN₂ and LHe the cryostat was left until the LHe was empty. At this point only the LHe was refilled. The presence of LN₂ is confirmed by monitoring its boil off. The hold time of the new LN₂ tank is >76 h and the LHe hold time increased to 59 hours(+16%). The LHe hold time of the cryostat is no longer limited by the hold time of the LN₂. In addition, we no longer observe the 0.1K increase in the temperature of the scan head after 48h.

Mechanical stability: Figure 2.3a,b present background corrected $z(t)$ traces, along with the corresponding FFT spectra (fig. c,d), as obtained with the original and new cryostats, respectively. The $z(t)$ traces were obtained with the STM feedback loop enabled (loop gain = 1%, $V = 0.1$ V, $I(\text{old/new}) = 2.5$ nA/ 50 pA and $\tau(\text{old/new}) = 2.5/ 1$ ms) during approximately 15 minutes. With the original cryostat, the root-mean-square (rms) noise amplitude (A_{rms}) was 1.03 pm, whereas with the new cryostat it was 1.07 pm. The width of the 95% confidence interval in height (Δz (95% conv)) was 4.12 versus 4.27 pm. As evidenced by the FFT, for both situations the dominant contribution to the z -background has a frequency of < 20Hz. As an example, the resonance at 3 and 7 Hz are a known resonance coming from the Ornstein building in which the setup is housed. To decouple the setup from the building it is placed on active vibration isolation legs. The results shown above demonstrates that the STM/AFM performance with both cryostats should be comparable. The STM and AFM images shown in chapter 4 are acquired with the new cryostat installed. These images are of similar quality as images obtained with the original cryostat (chapters 5-7).

In collaboration with Omicron GmbH we are also interested in the specific resonances of the LN₂ tank. The resonances of the LN₂ tank are expected between 100-200 Hz. The main source of vibrational excitation to the LN₂ tank is the LN₂ boiling. The boiling of the LN₂ is damped by inserting a low density metal wool inside the tank preventing large bubble formation. To determine which frequencies are related to the LN₂ tank we cancel the mechanical excitation of the tank by freezing the LN₂. This is done by pumping at the exhaust of the LN₂ tank. When the pressure above the LN₂ drops below ~200 mbar, the N₂ is solid (SN₂). The frequency spectrum recorded with SN₂ is shown in figure 2.3e. A drop in intensity of frequency bands centered around 113 Hz is observed. We conclude that these frequencies are related to the mechanical oscillation of the LN₂ tank. The amplitude of the oscillations is low meaning that the contribution of these frequencies to the total oscillation amplitude is small.

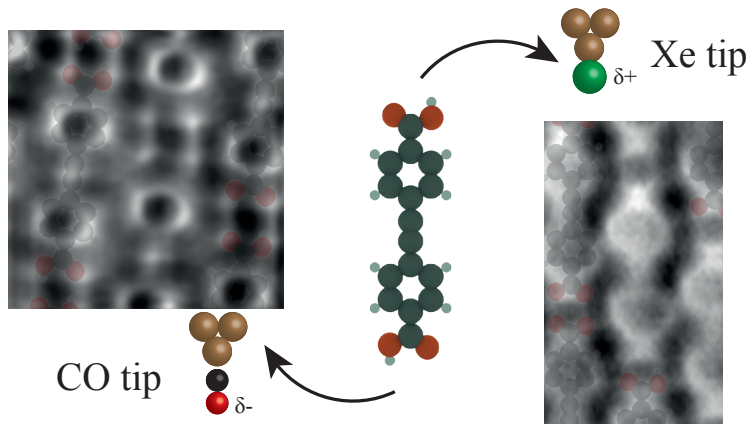
To conclude, we designed and build a new LN₂ tank for the cryostat of a low temperature microscope (Omicron GmbH). The hold time LN₂ tank has increased from 48 to >76 h. In addition, the LHe hold time has also increased to 59 h (+16%). The performance of the microscope before and after the installation has not changed.

2.5 References

- [1] P. von Böckh and T. Wetzel, *Heat Transfer* (Springer Berlin Heidelberg, Berlin, Heidelberg, 2012).
- [2] G. Kirchhoff, *Ann. Der Phys. Und Chemie* **185**, 275 (1860).

3

Sub-molecular resolution imaging of molecules by AFM: Pauli versus Coulomb



Based on

J. van der Lit, F. Di Cicco, P. Hapala, P. Jelinek, I. Swart
Physical Review Letters, *accepted* (2016)

The forces governing the contrast in atomically resolved atomic force microscopy have recently become a topic of intense debate. Here, we show that the electrostatic force is essential to understand the contrast in AFM images of polar molecules. Specifically, we imaged strongly polarized molecules with negatively and positively charged tips. Large differences in the contrast are observed above the polar groups. By taking into account the electrostatic forces between tip and molecule, the observed contrast differences can be reproduced using a molecular mechanics model. We assess the height dependence of the various force components.

3.1 Introduction

The use of FM-AFM as a tool to study molecules has grown tremendously over the past few years. The atomic structure of a single (unknown) molecule can now routinely be identified [1–3]. Even in the case of a complex mixture, the atomic structure of different molecules can be determined [4]. There is increasing interest in extracting quantitative information, such as bond-orders, from AFM experiments [5–7].

Several papers have addressed the forces responsible for the sub-molecular contrast observed in AFM images of molecules [8–13]. It is now well-established that the Pauli repulsion, i.e. the increase in the kinetic energy of electrons that results from orthog-

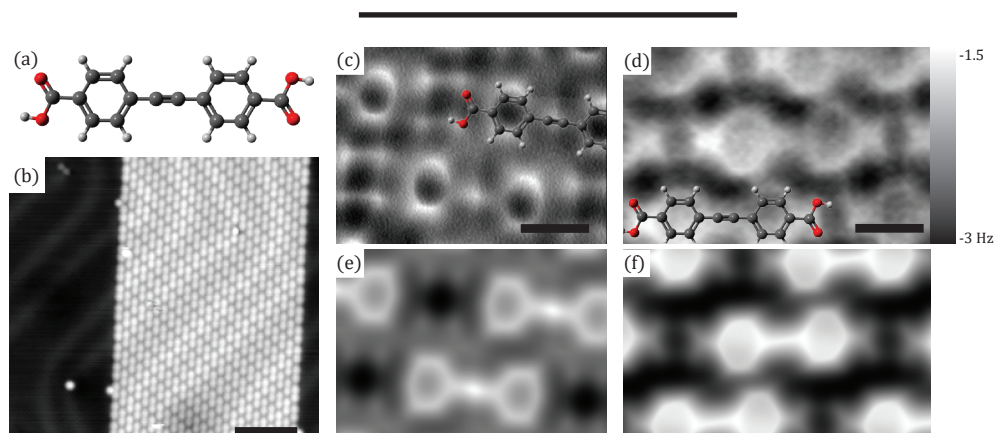


Figure 3.1. BPBA molecules on Au(111) imaged with a CO and a Xe tip. a. Model of BPBA. b. The self-assembled structure of BPBA on Au(111), 0.1V, 10pA, scale bar: 5 nm. c. Constant height Δf image of BPBA recorded with a CO tip at 0 V. The oxygen atoms and triple bond show bright, repulsive contrast while the carbonyl carbon is dark. Image recorded 1 Å below STM set point (0.1V, 10pA), scale bar: 5 Å. d. Constant height Δf image of BPBA recorded with a Xe tip at 0 V. The carboxylic acid appears as a fork with a bright carbon atom, while the oxygen's and triple bond are not clearly visible. Image recorded -2.55 Å below STM set point (0.1V, 10pA), scale bar: 5 Å. e. Simulated Δf image for a CO terminated tip with a $Q_{\text{tip}} = -0.05$ e- and $k_{x-y} = 0.25$ N/m. Bright contrast on oxygen's and central triple bond, as well as dark contrast on carbonyl carbon are reproduced. f. Simulated Δf image for a Xe tip with a $Q_{\text{tip}} = +0.3$ e- and $k_{x-y} = 0.25$ N/m. The fork structure of the carboxylic acid with bright carbon and unclear oxygen's as well as the unclear triple bond are reproduced.

onalization of their wavefunctions due to the overlap of electron clouds of the tip and molecule, is one of the most important force components [11]. In addition, van der Waals (vdW) interactions need to be taken into account. Finally, it is essential to account for the flexibility of the tip [5,8]. This flexibility is responsible for image distortions [14] and can enhance contrast between non-bonded atoms to such an extent that it mimics an apparent bond [8,9].

Thus far, mostly pure hydrocarbons were investigated, although recently also some images of molecules containing heteroatoms were published [1,15–18]. In the latter, the charge distribution can be highly non-homogeneous. For molecules weakly bound to the substrate the use of chemically passivated tips is essential to avoid accidental pick up of the molecule of interest [2]. When molecules are more strongly bound, also more reactive tips can be used [19,20]. Typically, chemical passivation is achieved by adsorbing a single CO molecule on the tip apex. It is known that a CO molecule adsorbed on a metal has a dipole moment [21,22], the size and direction of which is very sensitive to the adsorption geometry. Hence, when such a tip is used to image a polar molecule, the oxygen atom, which has a partial charge, will experience an electrostatic force. Electrostatic forces are known to be important in the imaging of polar substrates [21,23–26]. This raises the question what the influence of electrostatic forces is in AFM imaging of polar molecules with chemically passivated tips.

Here, we investigate how the contrast in AFM images of a molecule with strongly polarized groups (carboxylic acid, triple bond) depends on the charge of the tip. The structure of the molecule, bis-(para-benzoic acid) acetylene (BPBA), is shown in Figure 3.1a. CO and Xe terminated tips were used to create tips with negative and positive charge, respectively [21,27,28]. To minimize the influence of the vdW background, we studied self-assembled structures of BPBA. We find that the oxygen atoms of BPBA, which have a negative partial charge give, a repulsive/attractive contrast with a CO/Xe terminated tip, respectively, while the contrast above the adjacent carbon atom (with partial positive charge) shows the inverse. In addition, the whole carboxylic acid appears more narrow with the Xe tip. Also, the electron rich triple bond appears more repulsive with a CO tip than with the Xe tip. The experimentally observed contrast can only be reproduced in simulations when electrostatic forces are taken into account [27]. Finally, we assess the height dependence of the different force contributions to the contrast.

3.2 AFM imaging with CO and Xe terminated tips

BPBA molecules were evaporated from a stainless steel crucible using a Focus GmbH e-beam evaporator operated at 0.5 W power onto a clean Au(111) crystal held at 5 K located in a low temperature STM/AFM (Omicron GmbH). All images were recorded with a qPlus sensor ($f_0 = 21922$ Hz, $A_{p-p} = 2$ Å, $Q = 30$ k). After verification that the surface coverage was less than a monolayer, the crystal was allowed to heat to 300 K outside the microscope to allow the BPBA to self-assemble into a close-packed structure. The sample was placed back in the microscope after which Xe or CO was dosed onto the cold sample. CO and Xe terminated tips were prepared using standard procedures [29–33].

Figure 3.1b shows a STM overview of the self-assembled structure on Au(111). The well-known herringbone reconstruction of the Au(111) surface is clearly visible underneath the patches of molecules. Hence, the BPBA molecules interact weakly with the surface,

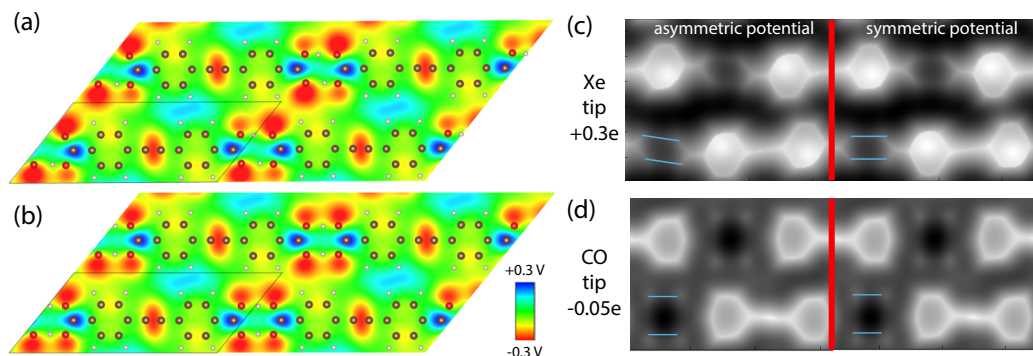


Figure 3.2 The influence of the Hartree potential 2.0 Å above the atomic cores of the molecules. a. Hartree potential corresponding to one of the configurations of hydrogen atoms on the carboxylic acid groups. The ketone oxygen has a stronger negative field than the hydroxyl oxygen. The corresponding atomic positions are overlaid. b. Hartree potential obtained by averaging of the potentials of the two configurations. The overlaid geometry is obtained by averaging the positions of the atoms of the two configurations. c-d. Simulated AFM image with a charged Xe(CO) tip using the symmetric and asymmetric potentials.

in agreement with observations made for other molecules on Au(111) [34,35]. Constant-height AFM images acquired with CO and Xe terminated tips at 0 V are shown in figure 3.1c/d. We first discuss the contrast in the images acquired with a CO tip. Both the ketone and alcohol oxygen atom of the carboxylic acid group, which both have a partial negative charge, are imaged as equally bright dots. We ascribe the equivalence of the oxygen atoms in the acid moieties to very rapid proton tunneling between the alcohol oxygen of one molecule and the opposing ketone oxygen of the neighboring molecule, resulting in an averaging effect (details will be discussed later) [36]. The carboxyl carbon atom (with partial positive charge) is not observed at this tip-sample distance with a CO tip, meaning it is still in the attractive regime. The electron rich triple bond in the center of the molecule also appears as a bright protrusion when imaged with a CO tip, similar to what has been observed before [3]. Now we discuss how the contrast changes when a Xe terminated tip is used. The carbonyl carbon is imaged as more repulsive than the neighboring oxygen atoms (i.e. less negative frequency shift). In addition, the triple bond is no longer clearly resolved. Finally, the dimensions of various features differs with different tips. Specifically, the apparent distance between the oxygen atoms belonging to the same molecule is smaller with a Xe tip than with the CO tip (1.6 ± 0.2 Å vs. 2.8 ± 0.2 Å), i.e. with a Xe tip the carboxylic acid group is imaged as a more narrow, fork-like, feature. Finally, the benzene rings appear larger with a Xe terminated tip (CO: 3.4 ± 0.2 Å vs. Xe: 4.4 ± 0.2 Å).

3.3 AFMulator

To shed light on the relative importance of the various force components, we performed extensive simulations using a molecular mechanics model (AFMulator) [8–10,37], including the electrostatic force [27]. Briefly, the model calculates the tip-sample force (F_{t-s}) via pairwise Lennard-Jones (L-J) potentials. Note that these potentials contain terms representing the vdW attraction and Pauli repulsion. In addition, electrostatic forces acting between

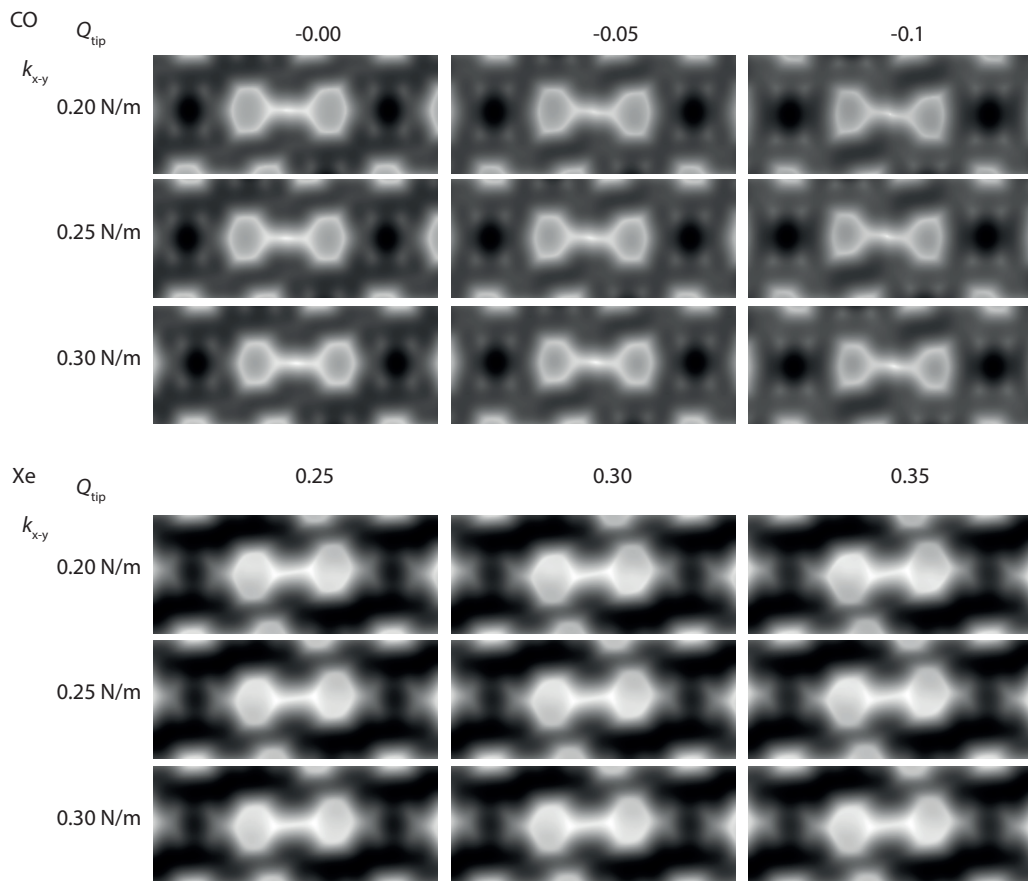


Figure 3.3. Top panel: Small changes in k_{x-y} and Q_{tip} for CO tip around the expected value of 0.25 N/m and -0.05 e-. No large contrast changes are observed. Bottom panel: Small changes in k_{x-y} and Q_{tip} for Xe tip around the expected value of 0.25 N/m and 0.3 e-. No large contrast changes are observed.

an effective charge Q_{tip} on tip and electrostatic Hartree potential of the sample [27], as calculated using DFT are taken into account. DFT calculations are performed using the Vienna Ab Initio Simulation package (VASP) [38] using generalized gradient approximation based functional PW91 [39] and projector augmented-wave method [40]. The plane wave basis set is chosen with $E_{\text{cut}} = 396$ eV. The calculated Hartree potential shows an asymmetry over the carboxylic acid groups due to the position of the hydrogen atom (fig. 3.2a). Because of the experimentally observed equivalence of the two oxygen atoms within the carboxylic groups we conclude that the image is symmetrized by rapid proton tunneling in the hydrogen-bonded carboxylic group pairs. This we account for by using an averaged force field, consisting of the Hartree potential and the L-J potential, as input for the AFMulator. The Hartree potential is obtained by averaging of the two Hartree potentials independently computed for the two hydrogen atom configurations (fig. 3.2b). The L-J potential is obtained from the averaged positions of atoms in the two configurations. The hydrogen atoms are centered between the two carboxylic acid groups as a result. Note that due to

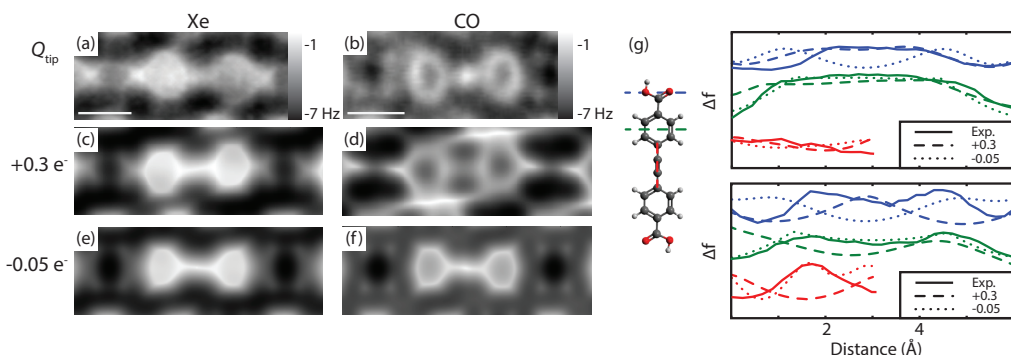


Figure 3.4. Importance of tip charge in simulated df images of BPBA in self-assembled structures. (a-b) constant height Δf images recorded with Xe and CO tip at 0 V on BPBA self-assembly (~ 3 Å and ~ 2.4 Å below STM set point 0.1 V/ 10 pA). (c-d) Simulations with tip charge: Q_{tip} : $+0.3 e^-$ for Xe and CO terminated tips. The carbonyl carbon shows repulsive contrast while the oxygen's are more attractive in both images. The triple bond is not visible in both images. In (d), the acid fork structure is not reproduced and the image is more distorted. Both deviations are due to the smaller radius and different L-J parameters of the oxygen atom. (e-f) Simulations with tip charge Q_{tip} : $-0.05 e^-$ for Xe and CO terminated tips. The oxygen atoms and the triple bond are observed as bright protrusions, while the carbonyl carbon is more attractive. In (e) more repulsion is observed on the carbonyl carbon due to the large size of the Xe atom. k_{x-y} : 0.25 N/m in all calculations. g. Line profiles over characteristic parts of the molecule (indicated in the ball and stick model) from experimental data and simulations. top: Xe, bottom: CO.

small size the in-plane hydrogen atoms are usually not directly observed in sub-molecular AFM images and its precise position is therefore not crucial for the AFM contrast. In the subsequent calculation, only the atom at the very end of the passivated tip is allowed to relax in response to the total tip-sample force.

The main parameters that go into the simulations are the lateral force constant and the effective charge of the final atom of the tip, denoted as k_{x-y} and Q_{tip} , respectively. To avoid image distortions due to the edges of the molecular structure, we simulated a crystal of BPBA molecules in the experimentally observed configuration. The result of the simulations for the Xe and CO tips with $k_{x-y} = 0.25$ N/m, and $Q_{\text{tip}} = -0.05/+0.3 e^-$, for CO and Xe terminated tips, are shown in fig. 3.1e/f, respectively. These values for k and Q are in agreement with previous reports [14,27,41]. To determine the robustness of these values with respect to small changes in Q and k a systematic check is performed for the cases $k_{x-y} = 0.2, 0.25$ and 0.3 N/m as well as $Q_{\text{tip}} = 0.0, -0.05, -0.1$ for both tips (fig. 3.3). All the features observed experimentally (contrast over O and C atoms, triple bond, width of the carboxylic acid group, size of benzene rings, discussed above) are reproduced very well in the simulations

To demonstrate the influence of the electrostatic force, we first calculated two positively charged tips: a Xe (fig. 3.4c) and a CO tip (fig. 3.4d) and compare them to experimental images (fig. 3.4a-b). Importantly, the fictive positive CO tip gives a contrast that is comparable to that of the positively charged Xe tip. Namely, we observe a repulsive contrast on the carbonyl carbon and attractive contrast on the oxygen's, unclear triple bond and an increase

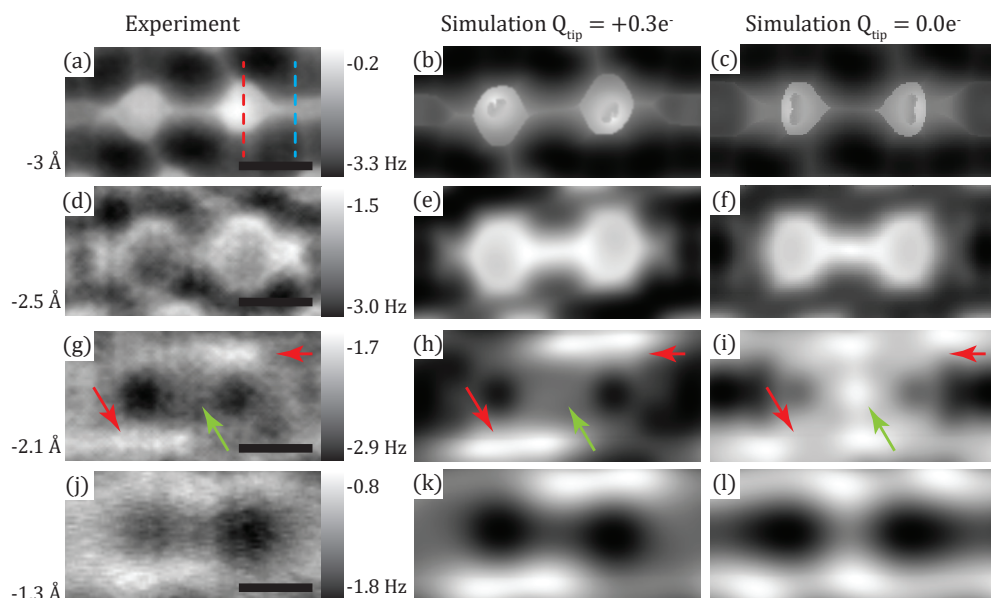


Figure 3.5. Height dependence of Δf images with a Xe tip compared to simulations with/without electrostatic force. a-c. Experimental (a) and simulated AFM images with (b) and without (c) electrostatic force ($Q_{\text{tip}} +0.3 \text{ e}^-$ and 0.0 e^-) at -3 \AA . Pauli repulsion dominates the contrast at this height. The electrostatic force causes a narrowing of the carboxylic acid group and a reduction in the symmetry along the long-molecular axis, as also seen experimentally. d-f. At -2.5 \AA , Pauli repulsion is still dominant but the electrostatic force results in a smaller repulsive interaction above the triple bond and a narrowing of the carboxylic acid group. g-i. Just after loss of atomic resolution, -2.1 \AA , vdW and electrostatic forces dominate the contrast. The experimentally observed asymmetric repulsive features between the molecules and the increased attraction above the triple bond are only reproduced in simulations with a positively charged tip. j-l. At -1.3 \AA vdW attraction determines the overall appearance, however, the electrostatic force is needed for the contrast over the triple bond. All scale bars: 2.5 \AA , experimental distance with respect to STM set point $0.1 \text{ V}/10 \text{ pA}$, simulations have the same Δz between images as the experiment.

in the diameter of the benzene rings. The additional image features in figure 3.4d between the molecules are due to a relatively large contribution of the electrostatic force because of the smaller size of the oxygen atom (1.66 \AA vs. 2.18 \AA for O/Xe). The simulation with a negatively charged Xe tip shows similar contrast as the simulation with a negatively charged CO tip. Lines profiles over the discussed details are shown in fig. 3.4g. This conclusively demonstrates that the electrostatic force contribution is essential in our understanding of the imaging contrast of AFM images of polar molecules.

The sub-molecular contrast is directly related to the strong lateral relaxations of a flexible molecule or atom (CO, Xe) attached to the metallic tip apex. These relaxations are driven not only by attractive van der Waals and repulsive Pauli interaction but also by the electrostatic interaction. Namely, the presence of the electrostatic interaction changes the relative intensity of the observed AFM contrast over atoms/bonds but it also affects the

position of sharp contours due to an extra lateral relaxation of the flexible probe. Consequently, both the intensity and shape of the sub-molecular AFM images acquired with functionalized tips with the opposite effective charge (positive Xe and negative CO terminated tips) vary significantly, as shown in figure 3.4. The possibility to use distortions in AFM contrast to extract details about the spatial extent of the electrostatic force will be published elsewhere.

3.4 Distance dependence of the forces

Since the electrostatic force, Pauli repulsion and vdW attraction have a different distance dependence, it is important to establish the importance of each force component at different heights. To investigate the height dependence of these contributions, we acquired 150 constant height Δf images at 0 V with a Xe terminated tip and with a spacing of 5 pm starting from -3.3 \AA with respect to a STM set point of 0.1 V and 10 pA. In addition, we simulated AFM images over the corresponding height range with and without the electrostatic force. At close tip-sample distances (-3 \AA) the contrast is determined by the Pauli repulsion (fig. 3.5a-c). The bright benzene rings are reproduced in calculations with and without the electrostatic force (fig. 3.5b-c). However, the asymmetric position of the benzene rings along the long-molecular axis, as well as the lateral size of the benzene rings is only reproduced in the calculation including the electrostatic force (cf. fig. 3.5a-c). In addition, only the simulations with the electrostatic force can reproduce the more narrow appearance of the carboxylic acid group. At intermediate heights (-2.5 \AA), just after the onset of sub-molecular resolution, Pauli repulsion over the atoms results in sub-molecular contrast (fig. 3.5d-f). From a comparison between figure 3.5e and 3.5f, it is clear that the electrostatic force is essential to reproduce the experimentally observed repulsive contrast above the carbonyl carbon as well as the reduced contrast over the triple bond. In addition, we find that the benzene rings appear slightly larger (0.2 \AA) in simulations with a positively charged tip. At a tip-sample distance just before the sub-molecular resolution (-2.1 \AA), the contrast is very dependent on the electrostatic forces (fig. 3.5g-i). A calculation with only vdW forces cannot reproduce the experimentally observed contrast above the triple bond (green arrows) and in the area between the molecules (red arrows). At even greater tip-sample separation (-1.3 \AA), the vdW attraction above the benzene rings dominates and the molecule has a dumbbell shape in simulations with and without electrostatic interactions (Fig. 3.5j-l). However, by including electrostatic forces (that are inherently more long range), the agreement with experiment above the triple bond is improved. Hence, taking into account electrostatic forces is essential to understand the observed contrast over a wide range of tip-sample distances, even at small distances where the Pauli repulsion dominates.

3.5 Discussion

We note here that the model currently does not incorporate the vdW attraction between the molecule and the bulk tip. This additional attractive contribution strongly depends on the macroscopic tip shape, something which is very difficult to control experimentally. However, in the present case the omission of the bulk tip will only result in a rigid offset of the calculated frequency shift values because of the relatively flat background in the close-packed self-assembled layer.

Since the total tip-sample force strongly depends on the macroscopic tip-shape, it is difficult to quantitatively assess the magnitude of each force contribution. This would also require a more detailed calculation of the charge distribution of the tip (which is again

strongly tip dependent). Nevertheless, the electrostatic force calculated using the procedure described above is on the order of tens of pN. Previously measured total tip-sample force are on the order of 10-100 pN for CO functionalized tips [2,42]. This would indicate that a significant part of the total force at intermediate distances can be due to electrostatics. Especially when interpreting the AFM contrast above hydrogen bonds, which have a significant electrostatic component, taking into account Coulomb interactions can be very important.

3.6 Conclusion

In conclusion, we imaged strongly polarized BPBA molecules with negatively charged CO terminated tips and positively charged Xe passivated tips. The use of a close-packed self-assembled layer yields the flattest possible vdW background. We observe large differences in the Δf contrast. These differences can be understood by taking into account the electrostatic contribution to the total force. These differences are prominent at relatively large tip-sample distances and contribute significantly to the contrast even at closer distances.

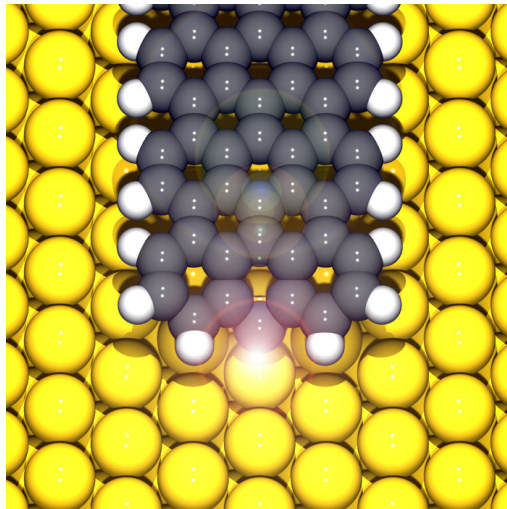
3.7 References

- [1] L. Gross, F. Mohn, N. Moll, G. Meyer, R. Ebel, W. M. Abdel-Mageed, and M. Jaspars, *Nat. Chem.* 2, 821 (2010).
- [2] L. Gross, F. Mohn, N. Moll, P. Liljeroth, and G. Meyer, *Science* 325, 1110 (2009).
- [3] D. G. de Oteyza, P. Gorman, Y.-C. Chen, S. Wickenburg, A. Riss, D. J. Mowbray, G. Etkin, Z. Pedramrazi, H.-Z. Tsai, A. Rubio, M. F. Crommie, and F. R. Fischer, *Science* 340, 1434 (2013).
- [4] B. Schuler, G. Meyer, D. Peña, O. C. Mullins, and L. Gross, *J. Am. Chem. Soc.* 137, 9870 (2015).
- [5] L. Gross, F. Mohn, N. Moll, B. Schuler, A. Criado, E. Guitian, D. Pena, A. Gourdon, and G. Meyer, *Science* 337, 1326 (2012).
- [6] Y. Sugimoto, P. Pou, M. Abe, P. Jelinek, R. Pérez, S. Morita, and O. Custance, *Nature* 446, 64 (2007).
- [7] M. Ternes, C. P. Lutz, C. F. Hirjibehedin, F. J. Giessibl, and A. J. Heinrich, *Science* 319, 1066 (2008).
- [8] P. Hapala, G. Kichin, C. Wagner, F. S. Tautz, R. Temirov, and P. Jelínek, *Phys. Rev. B* 90, 085421 (2014).
- [9] S. K. Hämäläinen, N. van der Heijden, J. van der Lit, S. den Hartog, P. Liljeroth, and I. Swart, *Phys. Rev. Lett.* 113, 186102 (2014).
- [10] M. P. Boneschanscher, S. K. Hämäläinen, P. Liljeroth, and I. Swart, *ACS Nano* 8, 3006 (2014).
- [11] N. Moll, L. Gross, F. Mohn, A. Curioni, and G. Meyer, *New J. Phys.* 12, 125020 (2010).
- [12] J. Zhang, P. Chen, B. Yuan, W. Ji, Z. Cheng, and X. Qiu, *Science* 342, 611 (2013).
- [13] C.-S. Guo, M. A. Van Hove, X. Ren, and Y. Zhao, *J. Phys. Chem. C* 119, 1483 (2015).
- [14] M. Neu, N. Moll, L. Gross, G. Meyer, F. J. Giessibl, and J. Repp, *Phys. Rev. B* 89, 205407 (2014).
- [15] S. Kawai, S. Saito, S. Osumi, S. Yamaguchi, A. S. Foster, P. Spijker, and E. Meyer, *Nat. Commun.* 6, 8098 (2015).
- [16] N. Pavliček, B. Fleury, M. Neu, J. Niedenführ, C. Herranz-Lancho, M. Ruben, and J. Repp, *Phys. Rev. Lett.* 108, 086101 (2012).
- [17] F. Albrecht, J. Repp, M. Fleischmann, M. Scheer, M. Ondráček, and P. Jelínek, *Phys. Rev. Lett.* 115, 076101 (2015).
- [18] B. Schuler, S.-X. Liu, Y. Geng, S. Decurtins, G. Meyer, and L. Gross, *Nano Lett.* 14, 3342 (2014).
- [19] K. Iwata, S. Yamazaki, P. Mutombo, P. Hapala, M. Ondráček, P. Jelínek, and Y. Sugimoto, *Nat. Commun.* 6, 7766 (2015).
- [20] A. Sweetman, S. P. Jarvis, P. Rahe, N. R. Champness, L. Kantorovich, and P. Moriarty, *Phys. Rev. B* 90, 165425 (2014).
- [21] M. Schneiderbauer, M. Emmrich, A. J. Weymouth, and F. J. Giessibl, *Phys. Rev. Lett.* 112, 166102 (2014).
- [22] A. Schwarz, A. Köhler, J. Grenz, and R. Wiesendanger, *Appl. Phys. Lett.* 105, 011606 (2014).
- [23] F. J. Giessibl, *Phys. Rev. B* 45, 13815 (1992).
- [24] G. Teobaldi, K. Lämmle, T. Trevelyan, M. Watkins, A. Schwarz, R. Wiesendanger, and A.L. Shluger, *Phys. Rev. Lett.* 106, 216102 (2011).
- [25] F. Bocquet, L. Nony, and C. Loppacher, *Phys. Rev. B* 83, 035411 (2011).

- [26] R. Hoffmann, D. Weiner, A. Schirmeisen, and A. S. Foster, *Phys. Rev. B* 80, 115426 (2009).
- [27] P. Hapala, R. Temirov, F. S. Tautz, and P. Jelinek, *Phys. Rev. Lett.* 113, 226101 (2014).
- [28] L. Gross, B. Schuler, F. Mohn, N. Moll, N. Pavliček, W. Steurer, I. Scivetti, K. Kotsis, M. Persson, and G. Meyer, *Phys. Rev. B* 90, 155455 (2014).
- [29] D. M. Eigler, C. P. Lutz, and W. E. Rudge, *Nature* 352, 600 (1991).
- [30] B. Neu, G. Meyer, and K.-H. Rieder, *Mod. Phys. Lett. B* 09, 963 (1995).
- [31] A. Yazdani, D. M. Eigler, and N. D. Lang, *Science* 272, 1921 (1996).
- [32] G. Kichin, C. Weiss, C. Wagner, F. S. Tautz, and R. Temirov, *J. Am. Chem. Soc.* 133, 16847 (2011).
- [33] L. Bartels, G. Meyer, and K. H. Rieder, *Appl. Phys. Lett.* 71, 213 (1997).
- [34] J. van der Lit, M. P. Boneschanscher, D. Vanmaekelbergh, M. Ijäs, A. Uppstu, M. Ervasti, A. Harju, P. Liljeroth, and I. Swart, *Nat. Commun.* 4, 2023 (2013).
- [35] W.-H. Soe, C. Manzano, A. De Sarkar, N. Chandrasekhar, and C. Joachim, *Phys. Rev. Lett.* 102, 176102 (2009).
- [36] X. Meng, J. Guo, J. Peng, J. Chen, Z. Wang, J.-R. Shi, X.-Z. Li, E.-G. Wang, and Y. Jiang, *Nat. Phys.* 11, 235 (2015).
- [37] <https://github.com/ProkopHapala/ProbeParticleModel>.
- [38] G. Kresse and J. Furthmüller, *Phys. Rev. B* 54, 11169 (1996).
- [39] J. P. Perdew, K. A. Jackson, M. R. Pederson, D. J. Singh, and C. Fiolhais, *Phys. Rev. B* 46, 6671 (1992).
- [40] P. E. Blöchl, *Phys. Rev. B* 50, 17953 (1994).
- [41] A. J. Weymouth, T. Hofmann, and F. J. Giessibl, *Science* 343, 1120 (2014).
- [42] M. P. Boneschanscher, J. van der Lit, Z. Sun, I. Swart, P. Liljeroth, and D. Vanmaekelbergh, *ACS Nano* 6, 10216 (2012).

4

Suppression of electron-vibron coupling in graphene nanoribbons contacted via a single atom



Based on

J. van der Lit, M. P. Boneschanscher, D. Vanmaekelbergh, M. Ijäs, A. Uppstu, M. Ervasti, A. Harju, P. Liljeroth, I. Swart
Nature Communications, **4**, 2023 (2013)

Graphene nanostructures, where quantum confinement opens an energy gap in the band structure, hold promise for future electronic devices. To realize the full potential of these materials, atomic scale control over the contacts to graphene and the graphene nanostructure forming the active part of the device is required. The contacts should have a high transmission and yet not modify the electronic properties of the active region significantly to maintain the potentially exciting physics offered by the nanoscale honeycomb lattice. Here, we show how contacting an atomically well-defined graphene nanoribbon (GNR) to a metallic lead by a chemical bond via only one atom significantly influences the charge transport through the GNR but does not affect its electronic structure. Specifically, we find that creating well-defined contacts can suppress inelastic transport channels.

4.1 Introduction

The atomic scale details of the contacts in molecular electronics are of crucial importance for the electrical characteristics of the device [1–3]. The contacts are typically realized through specific chemistries by using terminal functional groups, e.g. thiols for bonding to gold [4,5]. However, these approaches are not necessarily ideal in terms of electrical transparency, mechanical stability and atomic level control over the bonding geometry [5–7].

Atomic-scale control will also be required in contacting graphene nanostructures as their size is scaled down to open a sufficient energy gap between the valence and the conduction bands through quantum confinement for device operation at room temperature [8–13]. It is also critical for realizing novel graphene devices based on theoretically motivated concepts such as valleytronics [14,15]. Surprisingly, while graphene nanoribbons (GNRs) have been proposed to be used as molecular scale interconnects and components in graphene-based nanoelectronics, making contacts via metal-carbon bonds has not been examined experimentally.

Here, we contact an atomically well-defined GNR [13,16,17] to the gold substrate by a chemical bond via only one atom. This well-defined contact is formed by removing an individual hydrogen atom from the end of a GNR. We use combined atomically-resolved atomic force microscopy (AFM) and scanning tunnelling microscopy (STM) to show that this bond formation strongly suppresses the electron-vibron (e-v) coupling, but does not affect the bulk electronic structure of the GNR.

4.2 Geometric and electronic structure of the GNRs

We have carried out combined low-temperature STM/AFM experiments on atomically well-defined GNRs grown through the on-surface polymerization of 10-10'-dibromo-9,9'-bi-anthryl followed by thermal cyclodehydrogenation on Au(111) single crystals (fig. 4.1a, see Refs. [13,16,17] and methods section for details). A typical overview STM scan is shown in figure 4.1b. While many of the ribbons are attached to other ribbons or to gold step edges, we also observe individual, free ribbons (fig. 4.1c). Such free ribbons are mobile, i.e. imaging them with current set-points above 10 pA resulted in lateral motion along the long axis of the GNR. This indicates that defect-free GNRs are only weakly coupled to the substrate, in line with previous experiments on π -conjugated molecules on Au(111) [18]. Atomically resolved constant-height AFM images, acquired with a CO terminated tip, of the central

part and the end of a ribbon are shown in figures 4.1d and 4.1e, respectively. The GNRs have the expected structure based on the synthesis procedure: a series of alternating rows of 3 and 2 fused benzene rings along its long axis and termination in an anthracene moiety. We do not observe any reconstruction of the edges. Hence, the edges and ends correspond to arm-chair and zigzag termination, respectively. Similar images of an entire ribbon show that the synthesis method typically yields defect-free GNRs. However, defects are sometimes observed. An example is displayed in figure 4.1f, which shows an atomically resolved image of a GNR comprised of 22 monomers units. This ribbon has one missing benzene ring (indicated by the red arrow) that is clearly visible in the AFM (fig. 4.1f). However, this major modification of the geometric structure is difficult to identify in the corresponding STM image (fig. 4.1g). This underlines the importance of acquiring simultaneous STM and AFM data.

The electronic structure of defect-free and free-lying GNRs are probed using differential conductance spectroscopy [19,20]. In agreement with previous work, we find the onset of the valence and conduction bands at -0.9 V and 1.8 V, respectively (fig. 4.2a-b) [16]. An additional resonance, located only at the end of the GNR, is observed 30 mV above the E_f (fig. 4.2c) in agreement with previous observations [21]. The valence and conduction bands are visualized using dI/dV mapping in the constant height mode (fig. 4.2d-e), while the

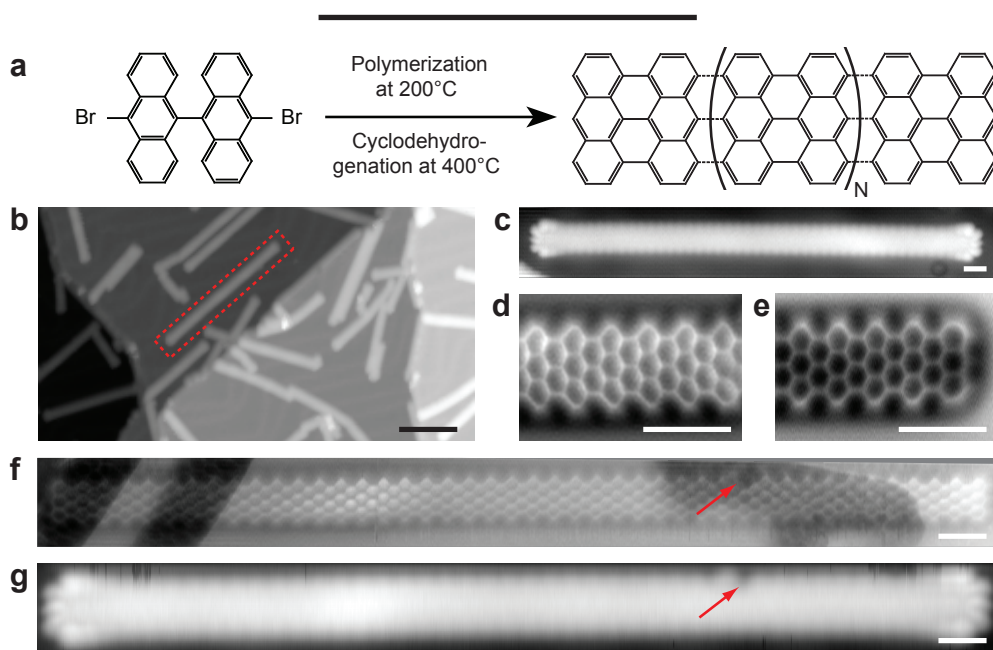


Figure 4.1 Chemical structure of atomically precise graphene nanoribbons. a. Bottom-up synthesis of an armchair GNR results in zigzag terminated ends. b. STM overview image showing a free GNR ($V = 50$ mV, $I = 5$ pA). c. Free GNR imaged with a CO terminated tip ($V = 10$ mV, $I = 5$ pA). d,e. Constant-height high resolution nc-AFM images of the middle and the zigzag end of a GNR obtained with a CO terminated tip (AFM set-point offset by 30 pm). f,g. Constant-height nc-AFM (f) and constant-current STM (g) images of 22 monomer unit long GNR with a single missing benzene ring marked by the red arrow. AFM set-point offset by 48 pm. Scale bar in b: 10 nm, others: 1 nm.

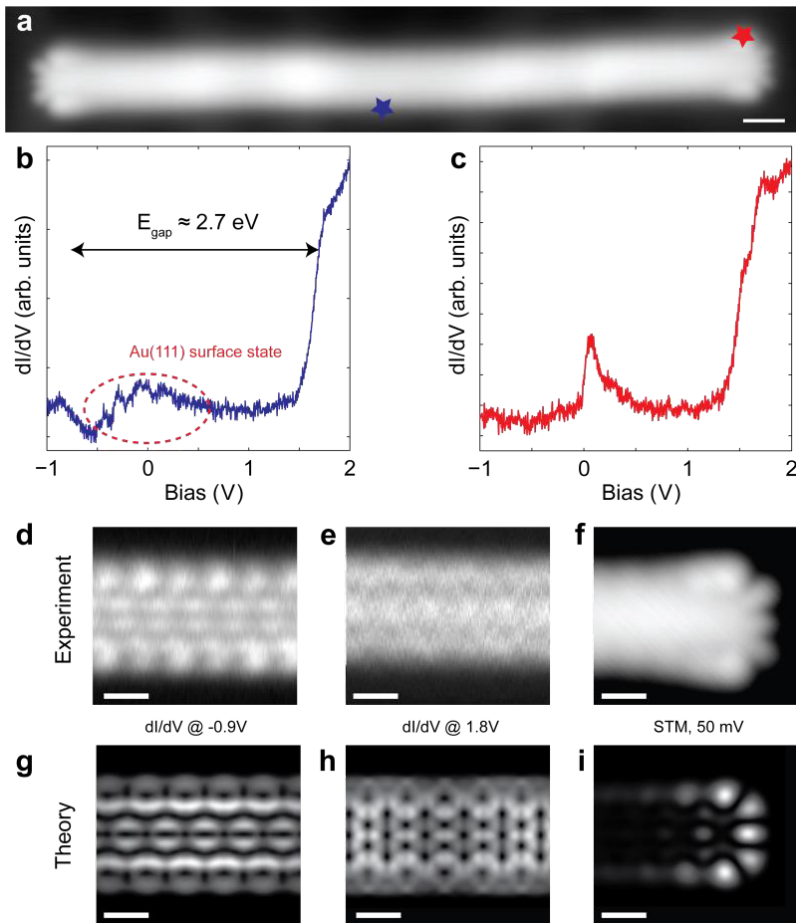


Figure 4.2. Electronic structure of free lying graphene nanoribbons. a. An STM image of a free GNR ($V = 50$ mV, $I = 20$ pA). b. dI/dV spectrum recorded on the center of the ribbon showing the bandgap to be 2.7 eV in line with previous experiments [16,17]. c. dI/dV spectrum recorded on the GNR end showing the in-gap state with vibronic replicas. d,e. Constant-height dI/dV maps of the valence and conduction bands of the GNR, respectively, acquired with a CO terminated tip. f. Constant-current STM image of the zigzag terminus acquired with a metal tip. g,h. Simulated local density of states maps of valence and conduction bands, respectively, assuming a pure p-wave tip. i. Simulated local density of states map of the end state assuming an s-wave tip. All scale bars: 0.5 nm.

state located at the end of the GNR can be observed in constant current STM. The calculated density of states of the valence band and the state at the end of the GNR, shown in figure 4.2g and 4.2i, agree well with the experiments. The agreement between the calculated (fig. 4.2h) and measured (fig. 4.2e) conduction band is less, which might be due to overlap in the states at the conduction band edge that we are unable to resolve.

In the following, we focus on the zigzag ends, which are the natural places for contacts. The GNR ends exhibit a localized state with an energy close to the Fermi level [21]. Figure 4.3a shows dI/dV spectra measured at the two ends of a free ribbon in a small bias range close to the Fermi energy. The resonance at 30 mV has been observed before and is assigned to an end-state localized at the zigzag edge [21]. Indeed, this feature is not present in spectra acquired with the tip positioned above the centre of the ribbon. The end state is located at positive bias, implying the GNR to be hole doped by the Au(111) substrate [13,16,18,22]. Its spatial extent can be imaged by taking dI/dV maps in the constant-height mode (fig. 4.3c). In order to enhance the spatial resolution of the maps, they were obtained with a CO-terminated STM tip, which gives the tip wavefunction p-wave character [23]. The experimentally

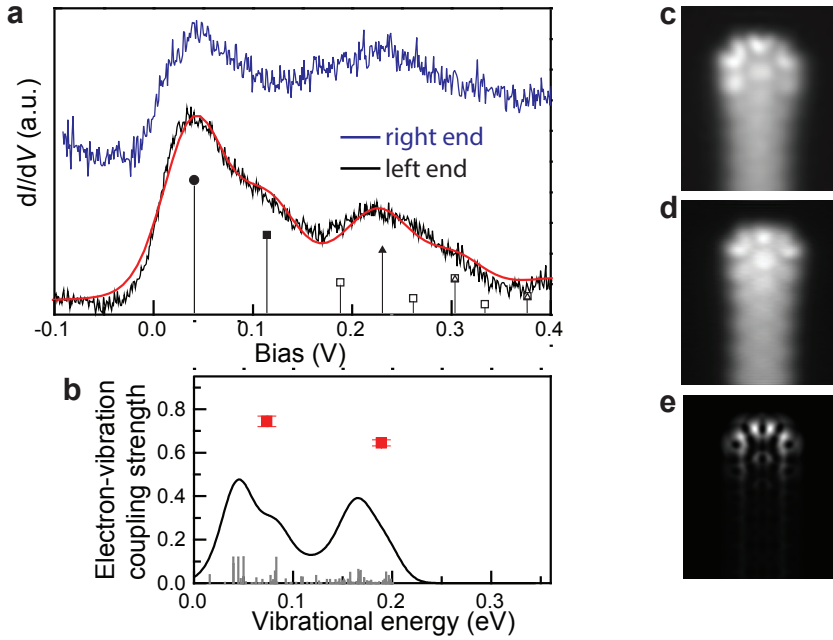


Figure 4.3. Comparison between experimental and calculated vibronic structure. a. Differential conductance spectra measured on the two ends of an isolated GNR (blue and black lines) fitted with a model for vibronic transport with two vibrational modes with energies of 74 meV and 189 meV, solid square and triangle, respectively. The elastic peak is indicated by a solid circle. Open symbols correspond to overtones and combination modes. All peaks were broadened by 40 meV and summed up to give the red line. Spectra acquired with a metal tip. b. Comparison between experimentally determined and calculated e-v coupling strength. The experimental points, as determined from fitting the spectrum in (a), are indicated by red squares. The calculated e-v coupling constants λ_q of all modes (gray lines) were broadened by a gaussian of 15 meV, and summed up (black line). Note that the zero energy corresponds to the energetic position of the elastic peak as determined in (a). c,d. Constant-height dI/dV maps recorded with a CO-terminated tip at the bias voltage corresponding to the elastic peak (c, 50 mV) and to the vibronic replica (d, 225 mV). e. Corresponding calculated local density of states map assuming that CO-tip can be modelled as a p-wave tip. Scale bars: 0.5 nm.

observed nodal plane structure is in agreement with the simulated image (fig. 4.3e). Note that the simulations did not take non-resonant tunnelling into account and used a purely p-wave tip [23,24].

4.3 Electron-vibron coupling

Two more peaks are observed in this bias range on the termini of free ribbons. One appears as a shoulder at ~ 80 mV and the third peak is located at ~ 220 mV (fig. 4.2a). The end-states of a neutral GNR are predicted to exhibit spin-splitting. However, relevant to our experiments, the splitting is predicted to be very small for charged ribbons. The energy levels of a GNR comprised of 6 monomer with a charge $q = 0, +1, +2$ are shown in figure 4.4a. Horizontal lines refer to molecular orbitals, and red upward-pointing and blue downward-pointing triangles refer to spin up and spin down electrons in the occupied states, respectively. In the neutral ribbon, the end-localized states are spin-degenerate and coincide with the HOMO and the LUMO. They consist of two states localized at the opposite ribbon ends. DFT predicts an antiferromagnetic coupling between the zero-energy states localized at zigzag edges, both of them being ferromagnetically oriented but populated with opposite spins. Upon charging, this spin degeneracy is broken and the gap between the two end states sharply decreases. In the $q = +1$ and $q = +2$ ribbons, there is a pair of end-localized states for both spins that are nearly but not exactly degenerate. In the $q = 1$ case, the HOMO belongs to one of these pairs, and the second pair is at approximately 0.2 eV. The very small HOMO-LUMO gap in this case is thus between the end-localized states of up spin species. In the $q = 2$ case, all end-localized states are spin-degenerate and unoccupied around 0.1 eV. In the finite armchair ribbons with three edge-atoms long zigzag ends, the splitting between the end states of the neutral ribbons is 0.43 eV and it is independent of the ribbon length (fig. 4.4b, black line). This is in contrast to infinite zigzag nanoribbons, in which the split decreases with an increasing ribbon width corresponding to increase of length in the finite ribbons [8]. Unlike the neutral HOMO-LUMO split, the end state split in charged GNRs decays exponentially with increasing length. Therefore, we attribute the extra peaks observed in the dI/dV spectrum to vibronic resonances.

Vibronic peaks arise as an electron tunnels through a molecular orbital and simultaneously excites a molecular vibration [25–27]. The energy spacing between the main peak and the first replica corresponds to the energy of that particular molecular vibration. The amplitude of the first replica is directly related to the strength of the electron-vibron coupling [28,29]. If the second and third peaks arise from vibronic tunnelling, they should have the same spatial dependence as the elastic resonance. This is confirmed in figures 4.3c and 4.3d, which show dI/dV constant-height maps at voltages corresponding to the first and third peak, respectively. The nodal plane structure observed at 50 mV and 225 mV is identical.

The overall line shape can be fitted well by a vibronic transport model with two vibrational modes (74 meV and 189 meV), including overtones and combination modes (red line, fig. 4.3a). The model uses the energies of the modes ($\hbar\omega_q$, the fitted response includes overtones and combination modes as predicted by the theory in ref. [28,30]) and the dimensionless coupling constants λ_q as the fitting parameters. The e-v coupling strength can also be calculated theoretically using DFT [31–33]. The result of such a calculation on a 3 monomer unit long GNR is shown in figure 4.3b. The gray lines indicate the couplings to individual vibrational modes. Broadening the e-v coupling of each mode with a gaussian with a width of 15 meV results in the black line. The overall response has 2 strong peaks and

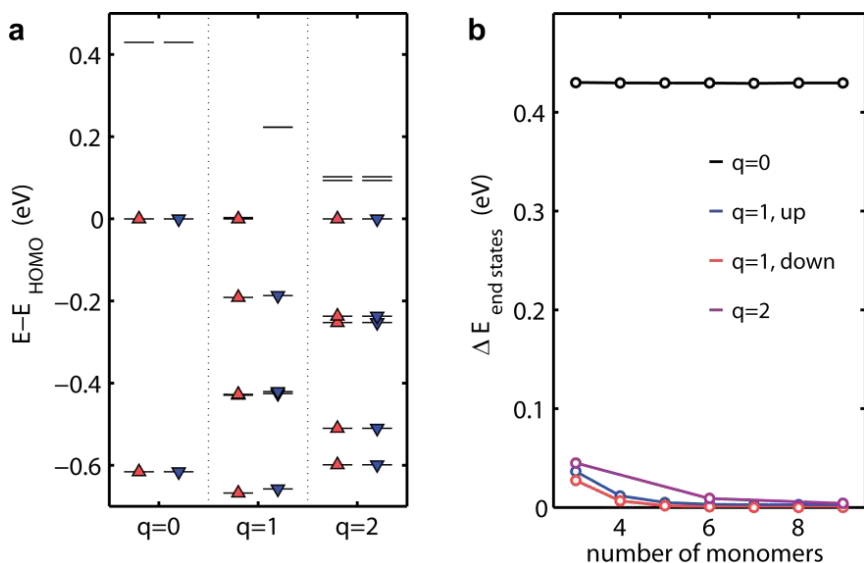


Figure 4.4. DFT calculations of spin splitting of the zigzag end state. a. Energy levels close to HOMO in neutral ($q = 0$) and hole-doped ($q = 1$, $q = 2$) six-monomer ribbons. Horizontal lines refer to molecular orbitals, and red upward-pointing and blue downward-pointing triangles refer to spin up and spin down electrons in the occupied states, respectively. Upon charging, the spin degeneracy is broken and the gap between the two end states sharply decreases. In the $q = 1$ and $q = 2$ ribbons, the gap is 0.2 and 0.1 eV, respectively. b. The energy split between the states localized at the zigzag ends as a function of the number of monomers for neutral (black) and charged ($q = 1$ and $q = 2$) ribbons (red and blue refer to the two spin channels).

a shoulder on the lower energy peak. This can be compared to the energies and coupling constants as determined from the experimental dI/dV spectrum. While the energies are in reasonable agreement, the coupling constants are underestimated by DFT. However, as in reality many modes contribute, the average coupling constant will go down as more modes are included in the fitting of the experimental dI/dV spectrum. Figure 4.5 shows the result of the vibronic transport model when fitting 3 or 4 modes (purple and green markers) together with the DFT results (grey vertical lines and solid black curve). An degrees in e-v coupling strength is observed with increasing number of modes.

One prerequisite to observe vibronic tunnelling is a sufficiently long lifetime of the excited state. In an STM setup this implies the existence of a double-barrier-tunnelling junction. This is typically realized by inserting a thin layer between the molecule/nanostructure and the metallic substrate [25–27]. Here, we observe for the first time vibronic charge transport through a carbon nanostructure adsorbed directly on a metal. This observation supports the notion that the interaction of π -conjugated molecules with Au(111) is weak (no chemical bonding) [18].

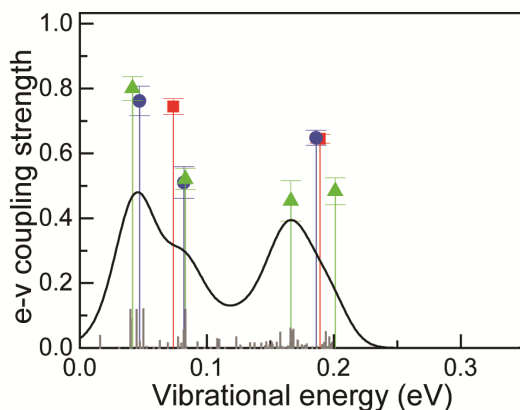


Figure 4.5. Fitting the vibronic structure in the dI/dV spectra. Comparison between the DFT calculation of the e-v coupling (black solid line) and the extracted coupling constants based on fitting the experimental dI/dV spectrum to vibronic transport model with two (red squares), three (blue circles) or four (green triangles) vibrational modes.

4.4 Contacting GNRs

To study the effect of contacting the GNR to a metal, we controllably created a single GNR-Au bond. An example of such an experiment is shown in figure 4.6. The middle hydrogen atom at one of the zigzag ends is removed by locally applying a high voltage pulse, similar to the procedures for dehydrogenation of phthalocyanine molecules on Au(111) [34] and benzene on Cu [35,36]. Figures 4.6a and 4.6b show a free GNR before and after applying a voltage pulse of 3.7 V at the left end of the nanostructure, respectively. After the pulse, the GNRs can no longer be moved laterally, indicating an increased interaction with the substrate. Atomically resolved AFM images show a dark (less repulsive) feature at the position of the middle C atom of the zigzag edge. However, the outer two C_6 rings appear unchanged, i.e. similar to the rings in the bulk of the ribbon and to the rings of the intact end. AFM imaging at smaller tip-sample distances reveals bonds in the direction of the middle zigzag C atom (fig. 4.6f). The above strongly suggests that the middle C atom bent down and formed a bond with the underlying Au(111) substrate.

Higher magnification STM images (fig. 4.6c and 4.6d) show how the electronic state on one end is modified by the bonding to the surface, while the spatial shape of the electronic state at the opposite end appears unaltered. Differential conductance spectra taken on the end where the contact was made show only one broad resonance. It is not possible to assess the strength of the vibronic coupling in this ribbon end due to the increased lifetime broadening caused by the bond formation. The shift of the peak may be related to p-type doping or to a change in the orbital energy due to the bond formation. Moreover, dI/dV spectra of the opposite (intact) end show that contacting the GNR several tens of nanometres away results in a large decrease in the electron-vibron coupling: the vibronic replicas are strongly suppressed due to formation of a single C-Au bond (at the opposite end). Note that the elastic resonance at the intact end is unchanged. In addition, contacting the GNR does not lead to changes in the conduction and valence bands as shown in figure 4.7. dI/dV spectra are recorded on the GNR before (fig. 4.7a) and after (fig. 4.7b) contacting it. The valence and conduction band onsets remain located at -0.9 and 1.8 V, respectively.

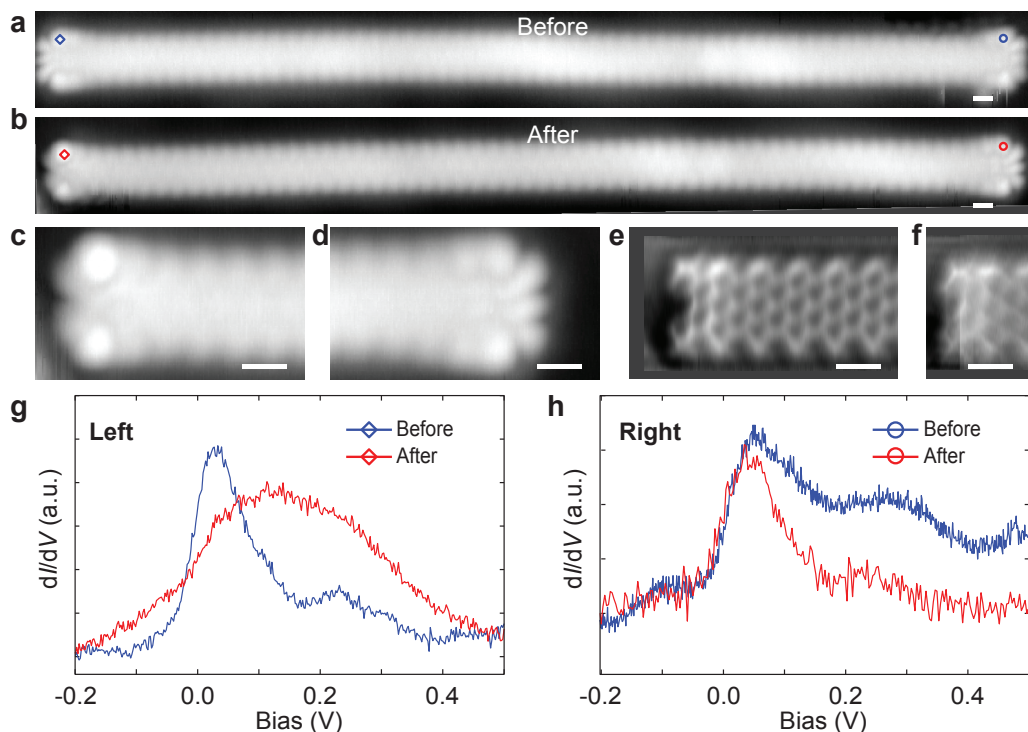


Figure 4.6. Controlled atomic scale modification of the GNR reduces vibronic coupling. a. High-resolution STM image of a free GNR ($V = 50$ mV, $I = 5$ pA). b. High-resolution STM image after a bias pulse has been used to modify the left end of the GNR ($V = 50$ mV, $I = 20$ pA). c,d. Zoomed-in STM images of the GNR ends after the modification (c: $V = 50$ mV, $I = 50$ pA, d: $V = 10$ mV, $I = 2$ pA). e. Atomically resolved AFM image of the contacted GNR (AFM set-point offset by 120 pm). f. AFM image of the same ribbon as in panel e, but with the tip 80 pm closer to the sample. g,h. dI/dV spectra recorded at the left and right ends of the GNR before (blue) and after (red) of the modification. All the images and spectra have been acquired with a CO-terminated tip. Scale bars: 0.5 nm.

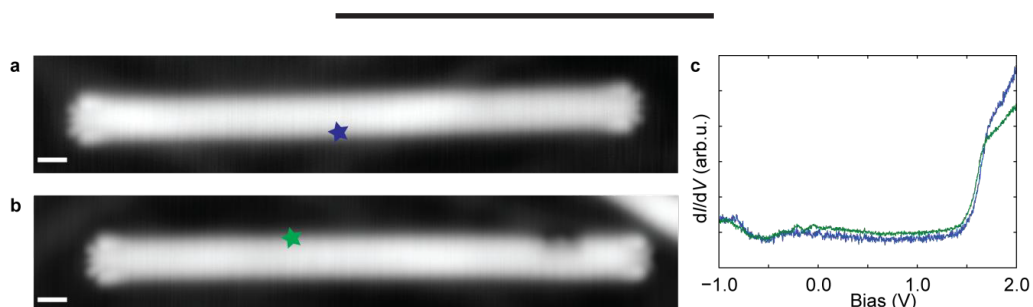


Figure 4.7. Influence of contacting on the valence and conduction bands. a. STM image of free lying GNR. b. STM image after applying a voltage pulse of 3.7 V to the right terminus. c. dI/dV spectra acquired at the armchair edge of the GNR before and after contact formation. The positions at which the spectra were acquired are indicated in a and b. Scale bars: 1 nm.

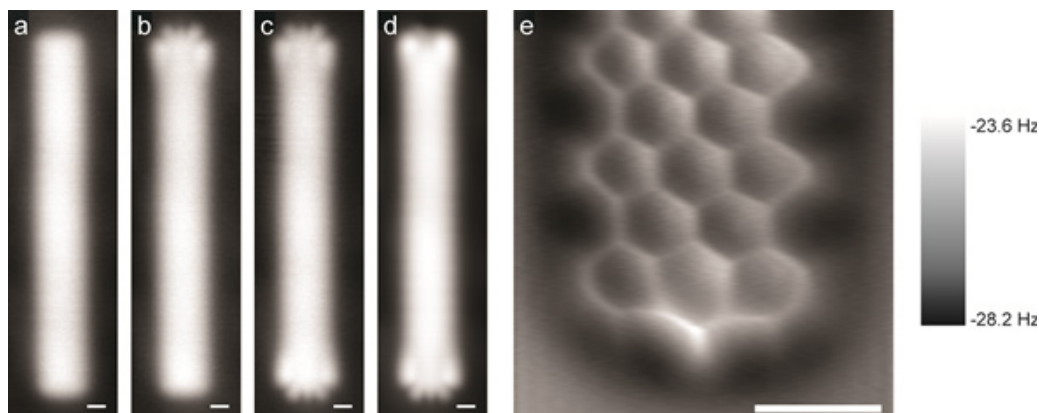


Figure 4.8. Hydrogen abstraction from the GNR terminus. a. Free lying GNR with two ends that do not show an end state at low bias ($V = 50$ mV, $I = 15$ pA). b. After applying a voltage pulse of 2.5 V at the top end, the ‘regular’ electronic state is observed ($V = 50$ mV, $I = 10$ pA). c. Applying a similar pulse to the bottom end leads to the appearance of this state also at the bottom ($V = 50$ mV, $I = 10$ pA). d. Applying a 3.7 V pulse at the top terminus resulted in the formation of a C-Au contact, as described in the main text ($V = 0.5$ V, $I = 150$ pA). e. Atomically resolved AFM image of the end of (a) that does not show states at low bias. Previously, this type of STM contrast on a GNR end was wrongfully assigned to a missing C atom [17]. The increased repulsion on the middle C atom is consistent with an sp^3 -hybridized C atom, passivated by two hydrogen atoms one of which is located above the GNR plane (CH_2 group). All scale bars: 0.5 nm.

This demonstrates that the electronic structure of the GNR is not affected by contacting.

Further evidence on the removal of a single hydrogen atom by voltage pulses comes from experiments on ribbons where the zigzag end does not exhibit the low bias state (fig 4.8). The free lying GNR in figure 4.8a has two hydrogen atoms on the centre carbon of the zigzag end that can be visualized in AFM (fig. 4.8e). The second hydrogen atom sticks out of the molecular plain suggesting a sp^3 -hybridized carbon and is imaged as a repulsive feature. A voltage pulse at the top/bottom termini removes one hydrogen and restores the original sp^2 -hybridization visible by the electronic state at these ends (fig. 4.8b-c). Finally, a higher voltage pulse at the top termini results in the formation of the Au-GNR bond (fig. 4.8d).

We have created single-atom contacts to 4 different free ribbons. In all cases, we observed a weakening of the e-v coupling strength. Since there is no registry between the ribbons and the Au(111) surface, it is unlikely that the weakening is due to a change of the adsorption site of the GNR. Furthermore, as pointed out above, the ribbons are weakly coupled to the substrate. For such systems, the substrate does not have a large influence on the relative magnitude of the e-v coupling strength (all spectra were acquired at positions with a maximum apparent height [24]). It is well-known that the lifetime of the electron on a molecular resonance has a significant effect on the vibronic coupling strength. As the lifetime is shortened, the vibronic features decrease in intensity [29], in line with our results. In addition, formation of an atomic contact increases dissipation, leading to a faster decay of the vibrationally excited state and to a decrease of inelastic carrier transport [37].

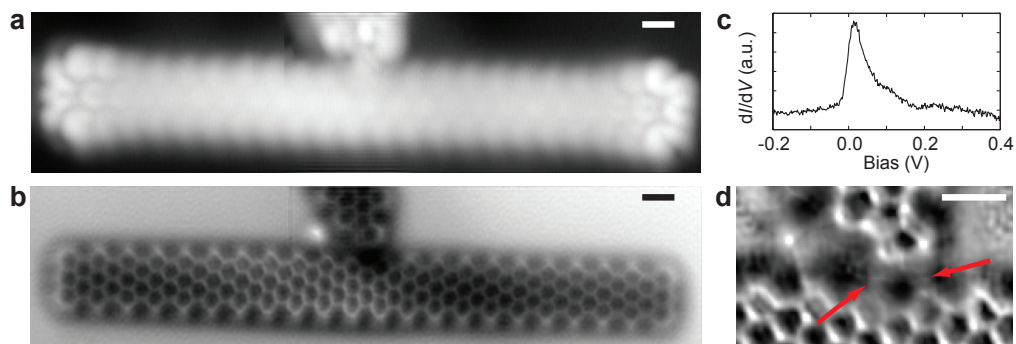


Figure 4.9. Chemical and electronic structures of commonly observed defects. a,b. STM (a) and AFM (b) images recorded with a CO terminated tip of a GNR connected in the middle by another ribbon (STM setpoint: $V = 10$ mV, $I = 15$ pA. AFM offset w.r.t. STM: 30 pm). c. dI/dV spectra acquired on the end of the ribbon shown in a (with a CO tip). d. Higher magnification constant height AFM image of the junction shown in b (local contrast). AFM set-point offset by 50 pm. Arrows indicate possible bonds between the ribbons. All scale bars 0.5 nm.

The results shown in figure 4.6 demonstrate that the strength of the electron-vibron coupling and the electron lifetime are sensitive to the exact atomic-scale structure of the GNRs. To investigate these effects in more detail, we examine a GNR that is most likely connected in the middle to another ribbon (fig. 4.9a-b and 4.9d). In turn this second ribbon is part of a large network of connected species. Such structures occur naturally after the on-surface polymerization and cyclodehydrogenation steps. While the elastic peak position and amplitude and wavefunction structure at the ends of the ribbon are very similar to an isolated GNR, the vibronic peaks are very weak (fig. 4.9c). This suppression of the e-v coupling is likely to be caused by a similar mechanism as in the case of contacting individual ribbons: The lifetime of the vibrationally excited state is reduced either due to increased tunnelling rate out of the GNR or increased energy dissipation due to better coupling with the phonons of the substrate or the neighbouring ribbon.

4.5 Conclusion

We have demonstrated that defect-free GNRs show a mid-gap state localized on the zigzag termini, as well as valence and conduction states in agreement with DFT. The GNRs are weakly coupled to the Au(111) substrate. Au-C bonds can be created at well-defined positions by removal of a single hydrogen atom through a voltage pulse from the STM tip. By directly comparing the electronic structure of a ‘free’ GNR with the electronic structure of the same ribbon after making contact with the metal substrate, we obtain direct and unambiguous information on the effect of coupling to the leads. This approach should be generally applicable to study the effect of contact formation. We find that creating a single carbon-metal bond does not modify the bulk electronic structure (valence and conduction bands) of the GNR, but strongly reduces the strength of the electron-vibration coupling of the end state due to an increased coupling with the substrate. This effect can be sensitively probed by measuring the amplitude of the vibronic replica, i.e. the intensities of inelastic transport signatures.

4.6 Methods

Sample preparation. The 10-10'-dibromo-9-9'bianthryl molecules were synthesized by subsequent decomposition of the Grignard of 9-bromo-anthracene over CuCl_2 followed by bromination using bromine [13,38]. Samples were prepared by evaporating the bi-anthryl precursor molecule from a Knudsen cell-type evaporator onto a Au(111) single crystal cleaned by standard procedures and two subsequent heating steps [13,17]. This resulted in a sub-monolayer coverage with a low number of free GNRs.

STM and AFM measurements. After the growth, the sample was inserted into a low-temperature STM/AFM ($T = 4.8$ K, Omicron LT-STM/QPlus AFM), housed within the same ultrahigh vacuum system (base pressure $<10^{-10}$ mbar). We used a QPlus sensor with a resonance frequency f_0 of 24.454 Hz, a quality factor of $>12k$, and a peak-to-peak oscillation amplitude of ~ 86 pm. STS measurements were performed using a lock-in amplifier ($f_{\text{mod}} = 714$ Hz, $A_{\text{mod}} = 10$ mV (rms)). Picking up an individual carbon monoxide molecule to the tip apex was used to achieve atomically resolved AFM images and to improve the spatial resolution of STM orbital imaging [23,39,40]. For the constant-height AFM images, the tip-sample distance was typically decreased by a few tens of pm (as indicated in the figure captions) w.r.t. the STM set-point ($V = 50$ mV, $I = 10$ pA) after switching off the feedback. AFM images were recorded with $V = 0$ V.

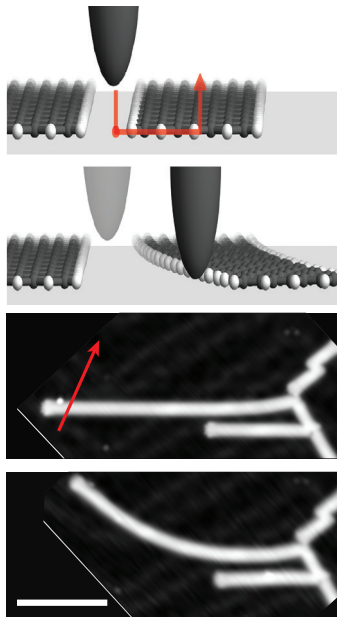
4.7 References

- [1] F. Chen, J. Hihath, Z. Huang, X. Li, and N. J. Tao, *Annu. Rev. Phys. Chem.* **58**, 535 (2007).
- [2] S. M. Lindsay and M. A. Ratner, *Adv. Mater.* **19**, 23 (2007).
- [3] J. Repp, G. Meyer, S. Paavilainen, F. E. Olsson, and M. Persson, *Science* **312**, 1196 (2006).
- [4] J. C. Love, L. A. Estroff, J. K. Kriebel, R. G. Nuzzo, and G. M. Whitesides, *Chem. Rev.* **105**, 1103 (2005).
- [5] S. Jan van der Molen and P. Liljeroth, *J. Phys. Condens. Matter* **22**, 133001 (2010).
- [6] C. Li, I. Pobelov, T. Wandlowski, A. Bagrets, A. Arnold, and F. Evers, *J. Am. Chem. Soc.* **130**, 318 (2008).
- [7] S. Guo, J. Hihath, I. Díez-Pérez, and N. Tao, *J. Am. Chem. Soc.* **133**, 19189 (2011).
- [8] Y.-W. Son, M. L. Cohen, and S. G. Louie, *Nature* **444**, 347 (2006).
- [9] L. A. Ponomarenko, F. Schedin, M. I. Katsnelson, R. Yang, E. W. Hill, K. S. Novoselov, and A. K. Geim, *Science* **320**, 356 (2008).
- [10] M. Han, B. Özyilmaz, Y. Zhang, and P. Kim, *Phys. Rev. Lett.* **98**, 206805 (2007).
- [11] C. Berger, Z. Song, X. Li, X. Wu, N. Brown, C. Naud, D. Mayou, T. Li, J. Hass, A. N. Marchenkov, E. H. Conrad, P. N. First, and W. A. de Heer, *Science* **312**, 1191 (2006).
- [12] M. Sprinkle, M. Ruan, Y. Hu, J. Hankinson, M. Rubio-Roy, B. Zhang, X. Wu, C. Berger, and W. A. de Heer, *Nat. Nanotechnol.* **5**, 727 (2010).
- [13] J. Cai, P. Ruffieux, R. Jaafar, M. Bieri, T. Braun, S. Blankenburg, M. Muoth, A. P. Seitsonen, M. Saleh, X. Feng, K. Müllen, and R. Fasel, *Nature* **466**, 470 (2010).
- [14] A. H. Castro Neto, N. M. R. Peres, K. S. Novoselov, and A. K. Geim, *Rev. Mod. Phys.* **81**, 109 (2009).
- [15] A. Rycerz, J. Tworzydło, and C. W. J. Beenakker, *Nat. Phys.* **3**, 172 (2007).
- [16] P. Ruffieux, J. Cai, N. C. Plumb, L. Patthey, D. Prezzi, A. Ferretti, E. Molinari, X. Feng, K. Mullen, C. A. Pignedoli, and R. Fasel, *ACS Nano* **6**, 6930 (2012).
- [17] M. Koch, F. Ample, C. Joachim, and L. Grill, *Nat. Nanotechnol.* **7**, 713 (2012).
- [18] W.-H. Soe, C. Manzano, A. De Sarkar, N. Chandrasekhar, and C. Joachim, *Phys. Rev. Lett.* **102**, 176102 (2009).
- [19] F. Mohn, J. Repp, L. Gross, G. Meyer, M. Dyer, and M. Persson, *Phys. Rev. Lett.* **105**, 266102 (2010).
- [20] I. Swart, L. Gross, and P. Liljeroth, *Chem. Commun.* **47**, 9011 (2011).
- [21] L. Talirz, H. Söde, J. Cai, P. Ruffieux, S. Blankenburg, R. Jafaar, R. Berger, X. Feng, K. Müllen, D. Passerone, R. Fasel, and C. A. Pignedoli, *J. Am. Chem. Soc.* **135**, 2060 (2013).
- [22] C. Bronner, F. Leyssner, S. Stremlau, M. Utecht, P. Saalfrank, T. Klamroth, and P. Tegeder, *Phys. Rev. B* **86**, 085444 (2012).
- [23] L. Gross, N. Moll, F. Mohn, A. Curioni, G. Meyer, F. Hanke, and M. Persson, *Phys. Rev. Lett.* **107**, 086101 (2011).
- [24] N. Pavliček, I. Swart, J. Niedenfür, G. Meyer, and J. Repp, *Phys. Rev. Lett.* **110**, 136101 (2013).
- [25] X. H. Qiu, G. V. Nazin, and W. Ho, *Phys. Rev. Lett.* **92**, 206102 (2004).

- [26] B. J. Leroy, S. G. Lemay, J. Kong, and C. Dekker, *Nature* **432**, 371 (2004).
- [27] J. Repp, P. Liljeroth, and G. Meyer, *Nat. Phys.* **6**, 975 (2010).
- [28] N. S. Wingreen, K. W. Jacobsen, and J. W. Wilkins, *Phys. Rev. B* **40**, 11834 (1989).
- [29] J. W. Gadzuk, *Phys. Rev. B* **44**, 13466 (1991).
- [30] N. S. Wingreen, K. W. Jacobsen, and J. W. Wilkins, *Phys. Rev. Lett.* **61**, 1396 (1988).
- [31] G. te Velde, F. M. Bickelhaupt, E. J. Baerends, C. Fonseca Guerra, S. J. A. van Gisbergen, J. G. Snijders, and T. Ziegler, *J. Comput. Chem.* **22**, 931 (2001).
- [32] C. Fonseca Guerra, J. G. Snijders, G. te Velde, and E. J. Baerends, *Theor. Chem. Accounts Theory, Comput. Model. (Theoretica Chim. Acta)* **99**, 391 (1998).
- [33] J. S. Seldenthuis, H. S. J. van der Zant, M. A. Ratner, and J. M. Thijssen, *ACS Nano* **2**, 1445 (2008).
- [34] A. Zhao, Q. Li, L. Chen, H. Xiang, W. Wang, S. Pan, B. Wang, X. Xiao, J. Yang, J. G. Hou, and Q. Zhu, *Science* **309**, 1542 (2005).
- [35] L. J. Lauhon and W. Ho, *J. Phys. Chem. A* **104**, 2463 (2000).
- [36] T. Komeda, Y. Kim, Y. Fujita, Y. Sainoo, and M. Kawai, *J. Chem. Phys.* **120**, 5347 (2004).
- [37] M. Čížek, M. Thoss, and W. Domcke, *Phys. Rev. B* **70**, 125406 (2004).
- [38] F. Bell and D. H. Waring, *J. Chem. Soc.* 267 (1949).
- [39] L. Gross, F. Mohn, N. Moll, P. Liljeroth, and G. Meyer, *Science* **325**, 1110 (2009).
- [40] Z. Sun, M. P. Boneschanscher, I. Swart, D. Vanmaekelbergh, and P. Liljeroth, *Phys. Rev. Lett.* **106**, 046104 (2011).

5

Bending and buckling of narrow armchair graphene nanoribbons via STM manipulation



Based on

J. van der Lit, P.H. Jacobse, D. Vanmaekelbergh, I. Swart
New Journal of Physics, **17**, 053013 (2015)

Semiconducting graphene nanoribbons (GNRs) are envisioned to play an important role in future electronics. This requires the GNRs to be placed on a surface where they may become strained. Theory predicts that axial strain, i.e. in-plane bending of the GNR, will cause a change in the band gap of the GNR. This may negatively affect device performance. Using the tip of a scanning tunneling microscope (STM) we controllably bent and buckle atomically well-defined narrow armchair GNR and subsequently probed the changes in the local density of states (LDOS). These experiments show that the band gap of a 7 atom wide armchair GNR is very robust to in-plane bending and out-of-plane buckling.

5.1 Introduction

For graphene to reach its full potential in electronic applications, it is essential to introduce a band gap [1]. There exist various ways to do so, ranging from creating graphene nanostructures, to inducing strain [2–5]. In case of graphene nanoribbons, the band gap depends on the width and termination of the ribbon. This makes GNRs promising structures for application in future electronics, especially if they are atomically well-defined. Sizeable band gaps are only obtained for armchair edge GNRs (ac-GNR) having a width on the order of 5–15 atoms [3–5]. When such an ac-GNR would be integrated into a (macroscopic) device it will almost certainly experience some form of strain [6,7]. This raises the question how strain affects the electronic structure of ac-GNRs.

Thus far, the influence of axial strain and in-plane bending strain on the electronic structure of GNRs has only been addressed theoretically. Depending on the type of strain, changes in the band gap ranging from a few tens of meV to 1 eV have been predicted [8–11]. Experimental verification of these predictions are scarce, especially for in-plane bending and buckling. Recent advances in the preparation of GNRs allows for synthesis of atomically precise 7-ac-GNRs on Au(111) under UHV conditions [12]. The electronic structure of these ribbons is well characterized [13–15]. High-resolution direct/inverse photoemission spectroscopy gives a band gap of 2.4 ± 0.4 eV [13]. Scanning tunneling spectroscopy (STS) measurements find a comparable band gap (2.6 eV) [14,15]. In a STM experiment the GNR could also be picked up to perform conductance measurements along its long axis [16]. In this experiment the conductance is observed to decrease when the GNR is lifted from the surface. This is ascribed to out of plane bending of the GNR, caused by lifting it from the surface. Here, we study how in-plane bending of atomically well-defined ac-GNRs affects their electronic structure. The ribbons are bent using the tip of a scanning tunneling microscope. The changes in the electronic structure are subsequently probed using STS.

5.2 Bending of ac-GNR

All experiments were performed in a low temperature STM/AFM (Omicron GmbH) kept at 4.5K using a tuning fork in the Q-plus design as the force sensor ($f_{\text{res}} = 24.454$ Hz, $Q = 12k$, $A_{\text{osc}} \sim 86$ pm). Seven atoms wide ac-GNR are grown by evaporating the precursor molecule 10-10'-dibromo-9-9'-bisanthracene onto a clean Au(111) surface kept at 200 °C, as described previously [12]. Subsequent heating to 400 °C leads to the formation of atomically well-defined ac-GNRs. All STS spectra are recorded using a lock-in amplifier with the oscillator set to $f_{\text{mod}} = 293$ Hz, $A_{\text{mod}} = 10/20$ mV RMS.

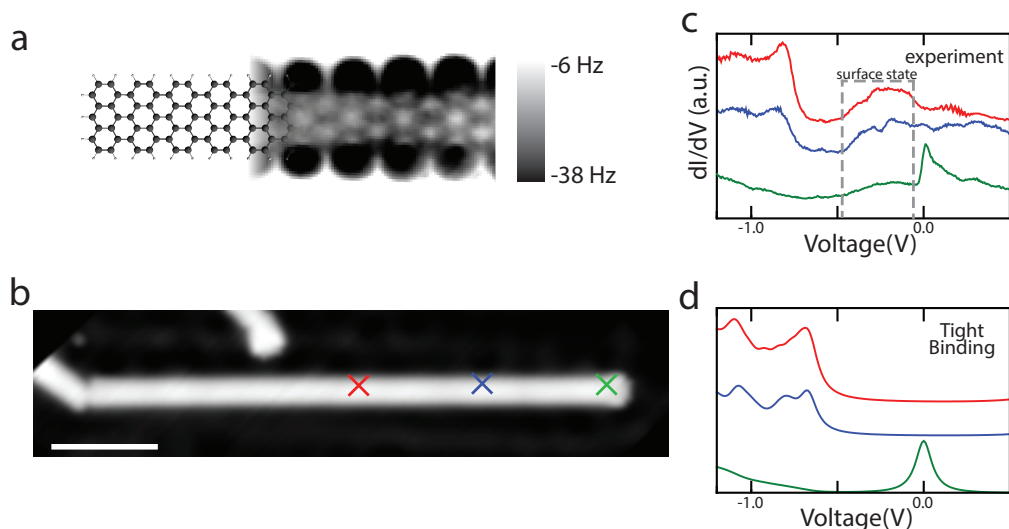


Figure 5.1. a. 7 atoms wide ac-GNR overlaid with atomically resolved AFM image. b. STM image of 7 atoms wide ac-GNR (100 mV, 100 pA) with colored crosses indicating positions of STS spectra, scale bar 5 nm. c-d. experimental and calculated (TB) STS spectra on ac-GNR (25 monomer units).

Figure 5.1a shows an atomically resolved AFM image of an ac-GNR measured with a metal terminated tip, overlaid with an atomic model. The measurement is performed at constant height and shows a large attractive force at the edge of the ribbons. At these points the GNR might be lifted slightly from the surface due to the reactive metal tip. Note that chemically passivated tips (typically CO terminated) are required to avoid accidental pick up of small molecules [17]. Scanning Tunneling Spectroscopy (STS) spectra recorded at several positions over a GNR (fig. 5.1b) shown in figure 5.2c show the onset of the valence band around -0.8 V. The onset becomes less steep when STS spectra are recorded closer to the end of a ribbon. Tight Binding calculations (TB) performed on gas-phase ribbons predict that the states on ac-GNRs can be considered as monomer states modulated by a 1D particle-in-a-box envelope function. Since the intensity of this envelope function varies spatially, a decrease in the LDOS is expected towards the end of the GNR. STS spectra extracted from the TB calculations (fig. 5.1d) are in good agreement with the experiment. Note that the broad in-gap resonance between -0.5 V and 0 V is due to the Au surface state under the ribbon.

The STM tip can be used for the manipulation of small molecules or atoms [18]. The same methodology can be used to bend GNRs. Briefly, in-plane bending of ac-GNR is done by placing the tip next to the GNR, disconnecting the feedback loop, moving the tip a few Angstroms towards the surface, and moving the tip in the direction of the desired bend (fig. 5.2a). After the manipulation, the feedback loop is reconnected and an image can be obtained of the bend ac-GNR (fig. 5.2b). We find that the maximum curvature that can be obtained for an ac-GNR is 2 deg/nm. Above this curvature the energy associated with the internal strain in the GNR is bigger than the interaction energy with the surface, causing the GNR to relax to a less strained conformation. An example of the changes in the electronic structure of a GNR due to bending to a curvature of 2 deg/nm is shown in figure 5.2c. The valence

band onset is shifted to lower bias by 59 ± 10 mV (fig. 5.3c, top), while the conduction band shifts to higher bias by 26 ± 10 mV (fig. 3c, bottom). The change in band gap is only 33 mV (1.3 %). Figure 5.3d shows the valence/conduction band of several GNRs, plotted as a function of curvature. In all cases, we find that for curvatures up to 2 deg/nm the effect of bending on the band gap is small, on the order of a few percent.

Note that since both the valence and conduction band shift in the same direction, we can rule out that the shift of the bands is caused by a change in voltage distribution in the tunnel junction (caused by e.g. a change in the adsorption height of the GNR on the Au(111)). Also, a slight buckling (induced by bending) is deemed unlikely: Buckling would result in one of the arm-chair edges being closer to the substrate, whereas the opposite edge is further away. This should lead to a shift in opposite directions on the two sides of the GNR. However, this is not observed experimentally. In addition, we did not observe differences in the apparent height along the short axis of the GNRs. Considering the above, we believe that the observed shift of the valence and conduction bands, as well as the small changes in the band gap are caused by the in-plane bending.

For planar ribbons, strain can be accommodated in changes in bond-angle and in bond length. In case of the latter, the distances between the atoms, and therefore the magnitude of the hopping integral, should change significantly. This should result in large changes in band gap. In contrast, if strain causes bond angles to distort, the magnitude of the hopping integral – and therefore the band gap – should not change much. Hence, we tentatively conclude that the strain induced by in plane bending is accommodated in distorted bond angles. This is consistent with the calculated ratio of the bond and angle stiffness [19,20].

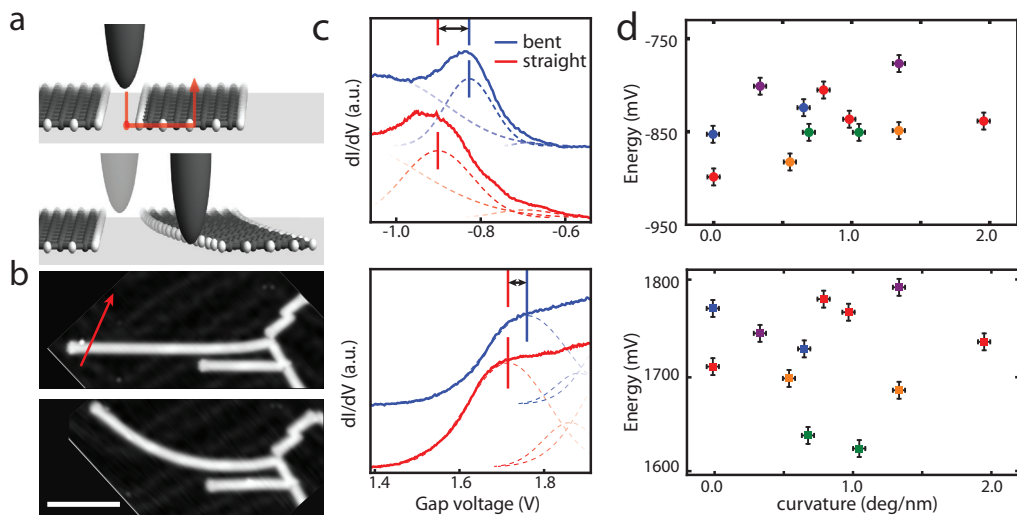


Figure 5.2. a. Schematic of GNR bending: after that the feedback loop is disconnected, the tip is moved towards the surface and the GNR is pushed by the tip. b. Top, a straight GNR with the tip trajectory indicated. Bottom, after manipulation the GNR is at its maximum curvature of 2 deg/nm. c. STS spectra of valence band (top) and conduction band (bottom) recorded for bent/straight ribbons. d. Position of valence band (top) and conduction band (bottom) recorded on several ribbons (indicated by colors) with different curvatures.

To investigate the mechanism of bending as well as to bend ac-GNR beyond 2 deg/nm, an additional z-step towards the surface was made before reconnecting the feedback loop. This additional z-step results in the deposition of a small cluster of atoms next to the ribbon (see fig 5.3a). We believe that the tip pushes the GNR since the cluster of atoms ends up on the side of the ribbon from which the tip came. This small cluster allows us to push the GNR beyond a curvature of 2 deg/nm (fig. 5.3a-1/2). Above a curvature of 4 deg/nm ac-GNRs start to buckle. This buckling is seen in STM images as a large increase in apparent height at the buckling site. The buckled GNR is stable on the surface indicated by the fact that it does not relax to a more straight conformation, even after removal of the cluster of atoms needed for curvatures between 2 and 4 deg/nm (fig. 5.3a-3). The STS spectrum in figure 5.3b is recorded on a straight part of a buckled ac-GNR. It shows the same features as a spectrum obtained on a straight GNR (VB at -859 mV, Au(111) surface state onset at -400 mV and the CB at 1757 mV) [14,15]. Buckled GNRs can be returned to (nearly) straight configurations. STM images acquired after ‘unbuckling’ do not reveal any defects, demonstrating that the buckling is a non-destructive process (fig. 5.3a-4).

5.3 Buckling of ac-GNR

Finally, we can use the STM tip to buckle the ac-GNR along the entire edge, resulting in a so-called partial-Single Walled Nanotube (p-SWNT) [15,21]. Figure 5.4a shows an intact ac-GNR. Figure 4b shows the same GNR after scanning several times at high bias (3.7V). A single voltage pulse of this magnitude leads to breaking of a C-H bond and formation of a C-Au bond [15]. The ribbon appears narrower and the apparent height has decreased w.r.t. the as-grown ribbons (see fig. 5.4d, location of the line profiles indicated in 5.4a and 5.4b). A constant height AFM image of this ribbon (fig. 5.4c, acquired with a metal tip) has a loss of contrast near the edges, consistent with a buckled structure [22]. Additionally, the large areas of attraction, seen for the intact GNR (fig. 5.1a), are no longer present. This suggests that the ribbon is more strongly coupled to the surface, in agreement with the narrower appearance and the lower apparent height. The above observations strongly suggest that

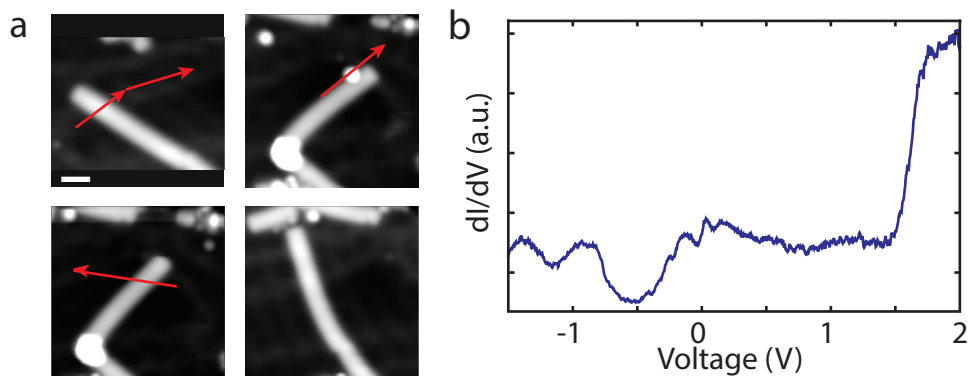


Figure 5.3. a. Bending of ac-GNRs beyond 2deg/nm. Arrows indicate the direction of tip motion. Top left image: 2 manipulations steps to bend a GNR beyond 2deg/nm. The last step is deposition of a small cluster of atoms to prevent GNR relaxation. Top right image: cluster is removed. Bottom left image: buckled GNRs is stable for imaging and can be straightened by pushing. Bottom right image: STM image after straightening the buckled GNR. b. STS spectra recorded on a straight part of a buckled GNR.

(almost) all C-H bonds are broken and that multiple C-Au bonds are formed. Due to mismatch of the GNR structure with the underlying Au lattice the p-SWNT is not evenly buckled. A STS spectrum before and after the buckling of the ac-GNR shows a broadening of the CB (fig. 5.4e), also consistent with an increased coupling to the surface [15].

5.4 Conclusion

To conclude, we have subjected atomically precise ac-GNR to several different types of STM manipulations. For in-plane bending of ac-GNRs up to curvatures of 2 deg/nm, both the conduction and valence band shift to lower bias. The changes in the band gap are on the order of a percent. A GNR can also be buckled, transforming it to a p-SWNT, by contacting the carbon atoms along the armchair edge to the Au substrate via tip induced bond formation. An atomically resolved AFM image shows the buckled structure. In this conformation the states of the ac-GNR broaden significantly due to increasing coupling to the surface.

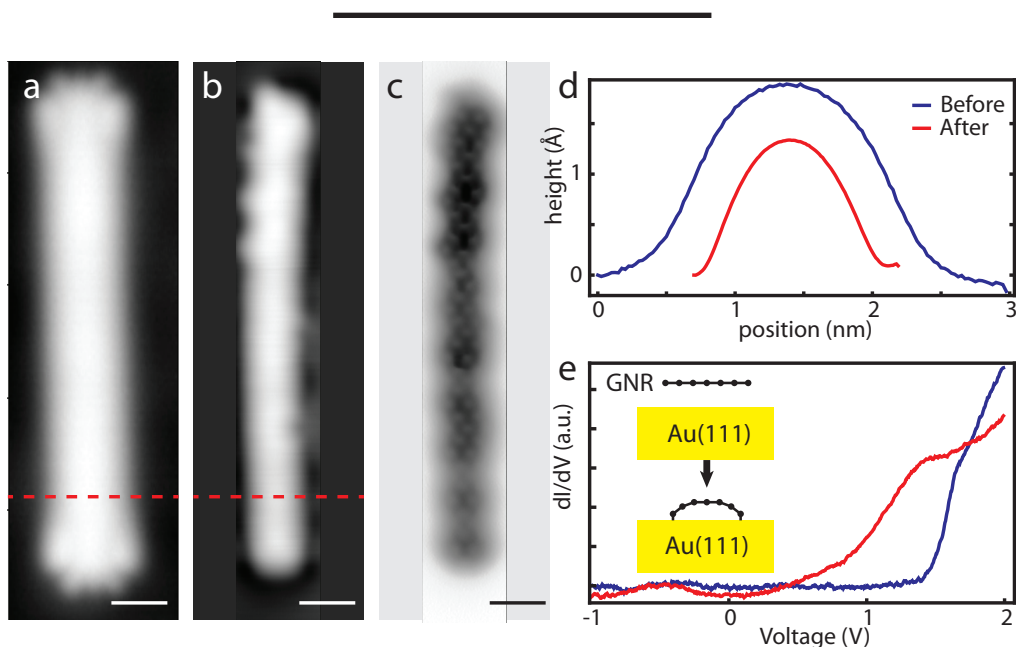


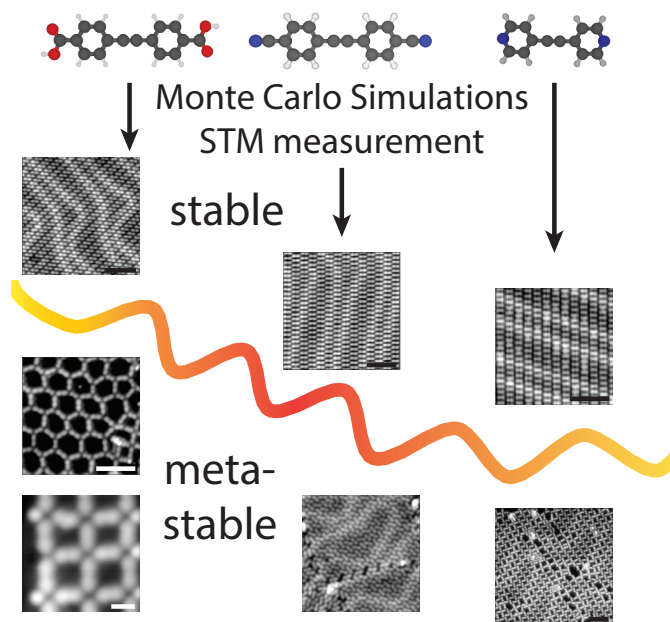
Figure 5.4. a. STM image of an intact GNR (50 mV, 2 pA). b. STM image (100 mV, 50 pA) of a buckled GNR after scanning the as-grown GNR multiple times at 3.7 V, 500 pA. c. Constant height AFM image of the buckled ac-GNR shown in b. d. height profiles of ac-GNR before and after buckling (dotted lines in (a) and (b)). e. STS spectra recorded on an ac-GNR before and after buckling (see inset).

5.5 References

- [1] K. S. Novoselov, V. I. Fal'ko, L. Colombo, P. R. Gellert, M. G. Schwab, and K. Kim, *Nature* **490**, 192 (2012).
- [2] V. Pereira, A. Castro Neto, and N. Peres, *Phys. Rev. B* **80**, 045401 (2009).
- [3] P. Shemella, Y. Zhang, M. Mailman, P. M. Ajayan, and S. K. Nayak, *Appl. Phys. Lett.* **91**, 042101 (2007).
- [4] Y.-W. Son, M. L. Cohen, and S. G. Louie, *Phys. Rev. Lett.* **97**, 216803 (2006).
- [5] M. Ezawa, *Phys. Rev. B* **73**, 045432 (2006).
- [6] X. Li, X. Wang, L. Zhang, S. Lee, and H. Dai, *Science* **319**, 1229 (2008).
- [7] X. Wang, Y. Ouyang, L. Jiao, H. Wang, L. Xie, J. Wu, J. Guo, and H. Dai, *Nat. Nanotechnol.* **6**, 563 (2011).
- [8] L. Sun, Q. Li, H. Ren, H. Su, Q. W. Shi, and J. Yang, *J. Chem. Phys.* **129**, 074704 (2008).
- [9] P. Koskinen, *Phys. Rev. B* **85**, 205429 (2012).
- [10] Y. Lu and J. Guo, *Nano Res.* **3**, 189 (2010).
- [11] O. Hod and G. E. Scuseria, *Nano Lett.* **9**, 2619 (2009).
- [12] J. Cai, P. Ruffieux, R. Jaafar, M. Bieri, T. Braun, S. Blankenburg, M. Muoth, A. P. Seitsonen, M. Saleh, X. Feng, K. Müllen, and R. Fasel, *Nature* **466**, 470 (2010).
- [13] S. Linden, D. Zhong, A. Timmer, N. Aghdassi, J. Franke, H. Zhang, X. Feng, K. Müllen, H. Fuchs, L. Chi, and H. Zacharias, *Phys. Rev. Lett.* **108**, 216801 (2012).
- [14] P. Ruffieux, J. Cai, N. C. Plumb, L. Patthey, D. Prezzi, A. Ferretti, E. Molinari, X. Feng, K. Mullen, C. A. Pignedoli, and R. Fasel, *ACS Nano* **6**, 6930 (2012).
- [15] J. van der Lit, M. P. Boneschanscher, D. Vanmaekelbergh, M. Ijäs, A. Uppstu, M. Ervasti, A. Harju, P. Liljeroth, and I. Swart, *Nat. Commun.* **4**, 2023 (2013).
- [16] M. Koch, F. Ample, C. Joachim, and L. Grill, *Nat. Nanotechnol.* **7**, 713 (2012).
- [17] L. Gross, F. Mohn, N. Moll, P. Liljeroth, and G. Meyer, *Science* **325**, 1110 (2009).
- [18] G. Meyer, J. Repp, S. Zöphel, K.-F. Braun, S. W. Hla, S. Fölsch, L. Bartels, F. Moresco, and K. H. Rieder, *Single Mol.* **1**, 79 (2000).
- [19] C. Li and T.-W. Chou, *Int. J. Solids Struct.* **40**, 2487 (2003).
- [20] K. Alzebedeh, *Int. J. Mech. Mater. Des.* **8**, 269 (2012).
- [21] Q. Yuan, H. Hu, J. Gao, F. Ding, Z. Liu, and B. I. Yakobson, *J. Am. Chem. Soc.* **133**, 16072 (2011).
- [22] M. P. Boneschanscher, J. van der Lit, Z. Sun, I. Swart, P. Liljeroth, and D. Vanmaekelbergh, *ACS Nano* **6**, 10216 (2012).

6

Modelling the Self-Assembly of Organic Molecules on Weakly Interacting Surfaces



Based on

J. van der Lit, J. L. Marsman, R. S. Koster, P. H. Jacobse, S. A. den Hartog, N. J. van der Heijden, D. Vanmaekelbergh, R. J.M. Klein Gebbink, L. Filion, I. Swart
Journal of Physical Chemistry C, **17**, 052013 (2015)

If organic molecules are to be used as the active component in devices, self-assembly represents the most attractive route to control the geometric structure and therefore part of the device performance. In this chapter, high-resolution STM measurement combined with DFT and MC calculations are used to study the stability of self-assemblies of molecules with bonding motifs spanning (nearly) the entire range of intermolecular interaction strengths. Our atomistic model reproduces the experimentally observed crystal structures with sub-Ångström precision in all cases. In addition, it is able to identify metastable structures through thermodynamic analysis. This model will allow for a-priori predictions of the structure of molecular self-assemblies on weakly interacting surfaces.

6.1 Introduction

The ability to control the properties of surfaces is of key importance for many technologies. One attractive route to achieve this is via the adsorption of organic molecules [1]. In particular, molecular layers can impart potentially useful features to surfaces, such as resistance to corrosion, templating, and biocompatibility [2,3]. Ordered molecular architectures can give rise to more sophisticated functionalities such as gas-sensing [4], molecular machines [5], and molecular circuitry for electronics [6,7]. Both the type of molecules as well as the geometric structure of the final self-assembled layer influence the properties of the material. Hence, structural control is of great importance.

On a surface, the interplay of molecule-molecule and molecule-substrate interactions governs the geometry of the final layer. For example, molecules with different functional groups but the same chemical backbone give rise to different self-assembled structures (vide infra) [8]. In addition, the same molecule can form multiple structures, [9] either because multiple crystals are stable or because a local minimum in free energy is kinetically favored. Specifically, phenomena such as kinetic trapping and pathway complexity can result in formation of metastable structures [10]. Such phases are well-known experimentally and a significant research effort is devoted to circumvent their formation [11–13]. On the other hand, control over metastable structures offers an additional avenue to tune the final geometry of the self-assembled phase via experimental parameters, e.g., the cooling rate [14].

Considering the vast parameter space and the importance of the structure for the final properties, a method that predicts which structures are thermodynamically stable and which are metastable based on just the chemical composition of the constituent molecules and the substrate used, is therefore highly desirable. Thus far, extracting thermodynamic information from models of molecular self-assembly has received little attention.

Different types of models have been used to simulate self-assembly. This includes models in which molecules are represented as geometric shapes that move on a lattice. The interactions between these shapes are described using a set of binding rules extracted from density functional theory (DFT). Alternatively, atomistic models have been devised [15,16]. In the absence of chemical reactions, intermolecular interactions are dominated by van der Waals attraction (vdW), Pauli repulsion, and electrostatic forces [1,17–20]. Hence, the atomic models should therefore include at least these three interactions. An accurate description of the electrostatic contribution is especially important, as these can range

from very weak to very strong and can be long-ranged. Since most classical force fields incorporate these interactions (in one form or another), these have been used to simulate self-assembly of molecules [9,15,16,21–24]. Additionally, methods for incorporating molecule-substrate interactions have been developed [25–27]. However, the ability to predict which crystals are stable and which are metastable has received little attention.

Here, we present an experimental and theoretical investigation of the self-assembly of molecules with different functional groups (carboxylic acids, nitrile groups, pyridine groups) on weakly interacting surfaces. This results in systems with strong, intermediate, and weak electrostatic interactions between molecules, respectively. We developed an atomistic model that accurately describes the forces between molecules based solely on the chemical structure of the molecules. Each atom is assigned a fractional charge, calculated from DFT and lone pairs are explicitly taken into account. This, together with the vdW and Pauli interactions, is used as input for Monte Carlo (MC) simulations. Both stable and metastable phases are identified. In all cases, the experimentally observed crystal structures are reproduced with a precision in the lattice parameters of 0.3 Å or better.

6.2 Self-assembly on a Au(111) surface

The magnitude of the electrostatic interactions is varied by introducing different functional groups (carboxylic acid, nitrile, and pyridine) to otherwise similar molecules. The structure of the molecules (bis-(para-benzoic acid)-actelyene, **1**, bis-(para-cyanobenzene)-actelyene, **2**, and bis-(para-pyridine)-acetylene, **3**) is given in figure 6.1a–c, respectively. The molecules were synthesized according to literature procedures [28–30]. For details, see the methods section. Molecules **1–3** were evaporated onto an Au(111) crystal cleaned by several sputter/anneal cycles held at room temperature from a stainless-steel crucible in an e-beam evaporator. In all cases only one type of molecule was evaporated and the coverage was below one monolayer. After evaporation the crystal was inserted into a LT-STM (Omicron GmbH) operating at $T = 4.5\text{ K}$ located in the same vacuum system.

All molecules formed at least two different structures on the Au(111) surface, an overview of which is shown in figure 6.1d–j. All three types of molecules appear as dumbbells in the STM images. Given the cooling rate of $>10\text{ K min}^{-1}$, it is very likely that some of these structures are metastable [14]. For all three molecules a close-packed crystal is observed (fig. 6.1d–f). All molecules also form self-assembled layers with a lower density (fig. 6.1g–j). Note that these structures are very different for the different molecules. For **1**, patches with honeycomb (fig. 6.1g) and square (fig. 6.1j) geometries are observed, whereas for **2** a ‘fishbone’ like structure (fig. 6.1e) is found. **3** forms multiple lower density structures that contain a significant number of defects, one of which is shown in figure ii. In the following, this chiral structure is referred to as the ‘windmill’ structure. Both stereoisomers are observed in equal amounts. As clearly seen in figures 6.1d–f, the herringbone reconstruction of the Au(111) surface is visible underneath all crystals. This implies that the interaction between the molecules and the surface is weak, in line with previous experiments on π -conjugated molecules on Au(111) [31,32].

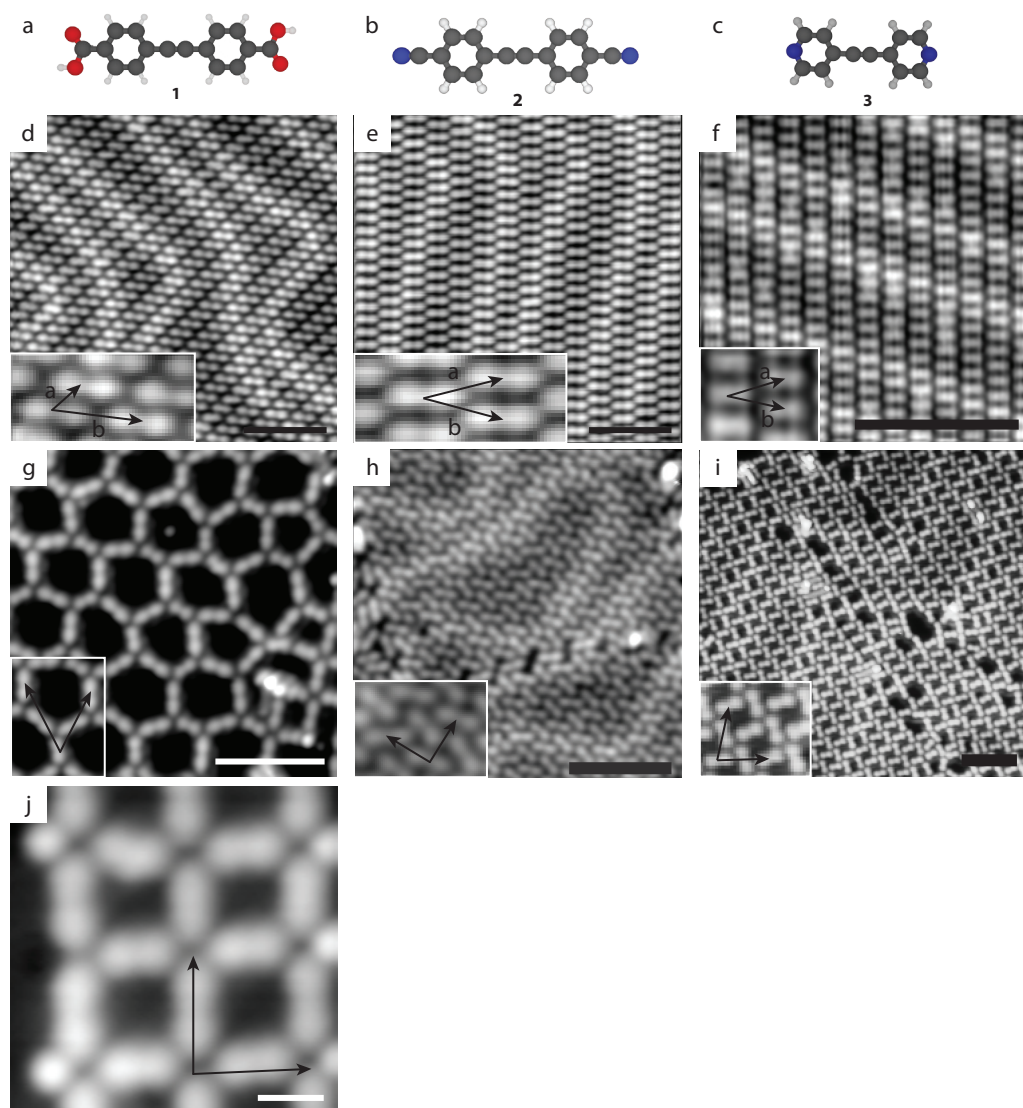


Figure 6.1. STM overview of self-assembled structures on Au(111). a-c. Structures of **1-3**, respectively. C, N, O, and H atoms are indicated in black, blue, red, and white, respectively. d-f. Close-packed crystals of structure of **1-3**, respectively. The insets shows the unit cells. g-j. Crystals with different geometries as observed for **1** (g,j), **2** (h) and **3** (i). All images are recorded on a Au(111) surface with tunneling parameters of 0.05-0.1 V/5-10 pA. Scale bars in d-i: 5 nm, in j: 1 nm.

6.3 DFT calculation of adsorption energies

To obtain more information on the interaction between **1-3** and the Au(111) substrate, we performed DFT calculations with periodic boundary conditions using the VASP package [33,34]. These calculations employed the optB88-vdW

functional to account for Van der Waals interactions and cut-off energies of 600 eV and 800 eV for the wavefunctions and the augmentation charges respectively. Each molecule was first allowed to relax in a vacuum until the forces were smaller than 1 meV/Å. Molecules were then placed in the high symmetry directions of the Au(111) surface: $[10\bar{1}]$ and $[\bar{1}2\bar{1}]$. For the Au(111) crystal, a lattice parameter obtained with a calculation of bulk Au was used. Due to the size of the molecules, the thickness of the Au(111) slab was limited to 4 layers. This resulted in slabs containing 9×6 Au atoms per layer for molecules oriented in the $[10\bar{1}]$ direction and 5×10 for molecules in the $[\bar{1}2\bar{1}]$ direction. The vacuum layer was 20 Å. The adsorption energy of a molecule is calculated by subtracting the energy of the empty slab and the free molecule from the combined system.

Figure 6.2 shows the adsorption energies of molecule 1-3 along the $[10\bar{1}]$ and $[\bar{1}2\bar{1}]$. The minima for all three molecules (shown in figure 6.2 with magenta open symbols) are located around $h_{\min} = 3.4$ Å for both directions. For molecules 2 and 3 the difference in the adsorption energy between the two high symmetry directions is very small. For molecule 1, they are somewhat larger. Adsorption energies in the range of -1.5 – 2 eV per molecule (-5 – 7 meV per atom), as well as adsorption heights of approximately 3.4 Å indicate a weak molecule-substrate interaction. A Bader analysis of the charge density shows that the total charge transfer between 1-3 and the substrate is on the order of 0.01 e^- . Hence, neutral molecules are used to model the self-assembly.

6.4 Monte Carlo simulations using Hunter-Sanders model

We now turn our attention to simulations of the self-assembled layers. In the absence of chemical bonding, the geometric structure of a molecule will to first order not change due to self-assembly. Hence, to model self-organization it should be sufficient to take into account only intermolecular interactions, i.e. we treat the molecule as a rigid body. To investigate the stability of the observed structures we propose an atomistic model that includes only vdW, Pauli and electrostatic forces between atoms. The vdW and Pauli are modelled using parameterized pair potential function from the AMBER force field [35]. As a starting point to model the electrostatic forces between molecules, we use the model by Hunter and Sanders [36]. This model accurately describes the packing of aromatic molecules in 3D crystals. The model is illustrated in figure 6.3a/b. Each atom that contributes to the π -framework is represented by 3 point charges (fig. 6.3b); a positive charge ($+1e^-$ for C, $+1.5e^-$ for N, $+2e^-$ for O) at the location of the nucleus and two negative point charges

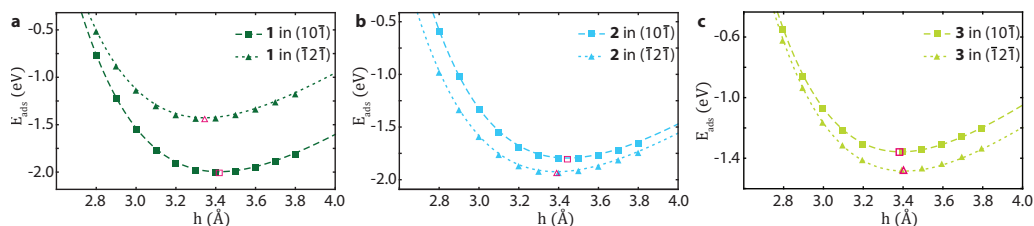


Figure 6.2. Adsorption energy of all molecules on Au(111) a. Energy distance curves for 1 with the molecule oriented in the high symmetry directions as indicated. Solid symbols indicate calculation results. The dotted and dashed lines correspond to a fit to the rational function $f(h) = a/h + b/h^2 + c/h^3$. Open magenta symbols indicate the minimum of the fit. b. Same as a, but for 2. c. Same as a, but for 3.

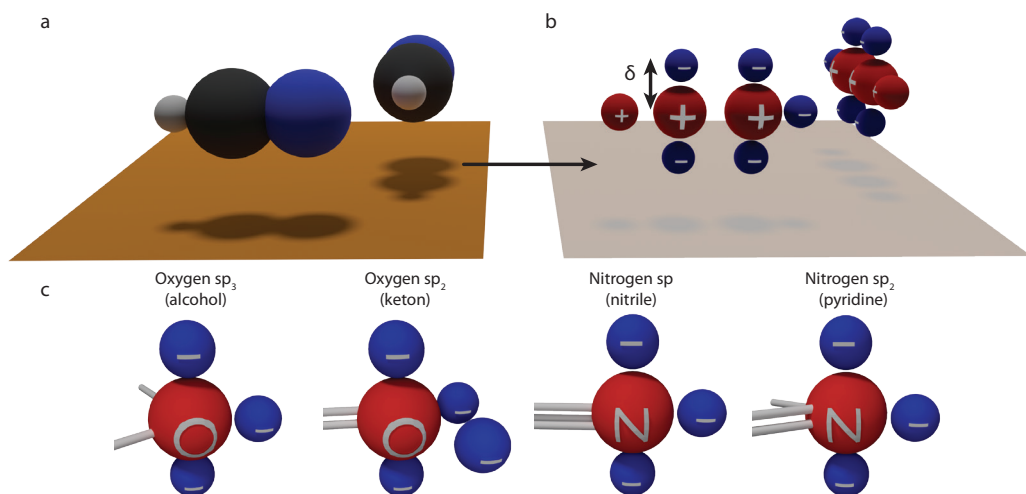


Figure 6.3. Atomic model to interpret molecular interactions. a. Two HCN molecules above a weakly interacting surface. b. Representation of the point charges in two HCN molecules comprising the electrostatic interaction. c. Lone pair configurations around oxygen and nitrogen atoms as used in the model.

($-0.5e^-$, $-0.75e^-$ and $-1e^-$) located a distance $\delta = 0.47 \text{ \AA}$ above and below the nucleus (fig. 6.3b). The value of δ is chosen such that the model reproduces the experimental value of the quadrupole moment of benzene [37]. We amend the original model by including the H atoms as single point charges at their atomic positions (fig. 6.3b). In addition, lone pairs of electrons are explicitly taken into account as additional negative point charges (fig. 6.3b). The number and position of lone pairs around an atom is determined by its hybridization. In figure 6.3c the lone pair configurations for oxygen and nitrogen used in this chapter are illustrated. All lone pairs are located a distance $\Delta_L = 0.47 \text{ \AA}$ from the positive charge. A sp^3 oxygen has one lone pair above and one lone pair below the plane. This can be modelled by including a single lone pair in the plane. The sp^2 oxygen has two lone pairs in the plane, separated by 120° . Nitrogen in a sp hybridization has one lone pair in line with the bonding direction. Finally, a sp^2 nitrogen has one lone pair in the plane directly opposite its two bonding partners.

In (nearly) all molecules, the electrons are inhomogeneously distributed over space leading to charge polarization. This charge polarization is incorporated by assigning a fractional charge to each atom. The magnitude of these partial charges are obtained by partitioning the total electron density, obtained from DFT, using the Voronoi Deformation Density (VDD) [38]. The magnitude of the negative point charges is determined by dividing the total negative charge of the atom ($-1e^-$ for C, $-1.5e^-$ for N, $-2e^-$ for O, corrected by the VDD charges) by the number of negative point charges surrounding it. For example, the N atom in figure 6.3b (VDD: $-0.17e^-$) is modelled by one positive charge of $+1.5e^-$ and three identical negative point charges of $(-1.5e^- - 0.17e^-)/3 = -0.443e^-$. Finally, the self-assembly is studied using Monte Carlo simulations in the canonical ensemble (details in methods section).

Snapshots of the simulation of **1-3** after MC runs of 4×10^6 , 2.5×10^6 , and 2.75×10^6 cycles are shown in figure 6.4a-c, respectively. At the start of the simulations, the molecules were

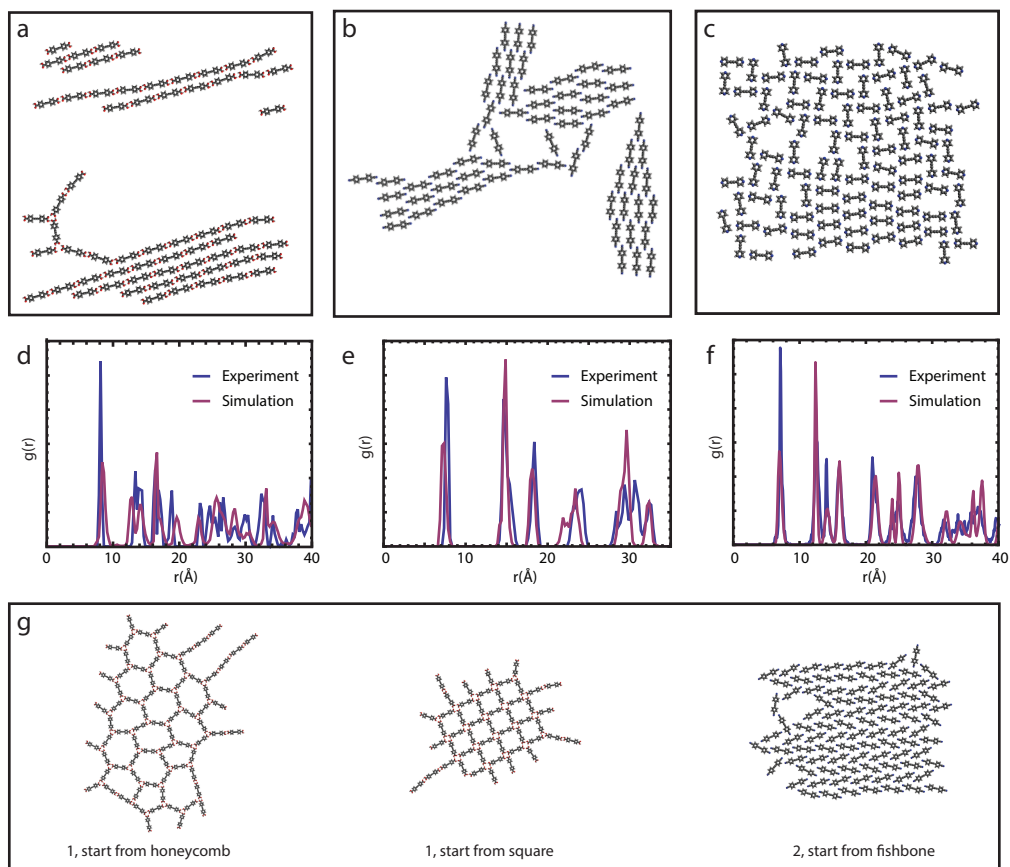


Figure 6.4. MC simulations of all molecules showing most stable structures. a. Snapshot of **1** after 4×10^6 MC-cycles at $T = 500$ K in a $150 \text{ \AA} \times 150 \text{ \AA}$ box showing self-assembly. b. Same as (a), but for **2** and after 2.5×10^6 MC-cycles at $T = 275$ K. c. Same as (a) but for **3**, and after 10^6 MC-cycles at $T = 150$ K. d-f. Radial distribution functions extracted from experimental (blue) and simulation (isotension-isothermal ensemble, red) data for close packed crystals of **1-3**, respectively. g. From left to right: snapshots of simulations starting with experimentally observed honeycomb and square crystals of **1** (after 3×10^6 , 3×10^5 MC cycles and at $T = 300$, 250 K respectively) and the 'fishbone' crystal of **2** (after 3×10^5 MC simulations, $T = 250$ K).

placed randomly in a $150 \times 150 \text{ \AA}$ box and the temperatures were fixed at $T = 500$ K, 275 K, and 300 K, respectively. For all molecules, patches of close-packed crystals are observed. These are also the most abundant in the experiment. Interestingly, for **3** also the lower density windmill structure is observed in the simulations.

To facilitate a comparison between experiment and theory, we determined the radial distribution function, $g(r)$, as well as the lattice parameters from the STM images and MC simulations. The crystals observed in the NVT simulations are rather small, making it difficult to extract meaningful parameters from these simulations. Larger crystals were obtained by using the crystals found in the NVT simulations as input for isotension-iso-

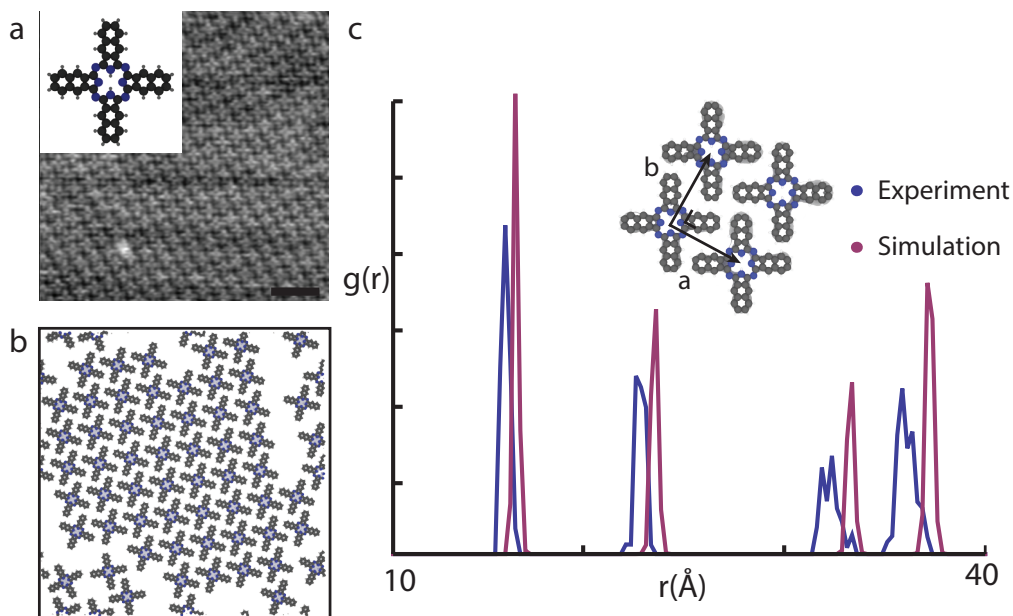


Figure 6.5. The self-assembly of 2,3-naphthalocyanine. a. STM image of close-packed crystal of **4** taken at room temperature. ($V = -1.47$ V, $I = 40$ pA). Scale bar: 5 nm. Data courtesy of M. Stöhr. The inset shows the chemical structure of **4**. Carbon, hydrogen and N atoms are indicated in gray, white and blue, respectively. b. Snapshot of 64 molecules after a MC run of 450K cycles at $T = 100$ K. c. $g(r)$ extracted from the STM images and MC simulations. The inset shows the unit cell of the molecular crystal. Lattice parameters are: $a = b = 16.1/16.6$ Å, $\alpha = 90/90^\circ$, respectively (experiment/theory).

thermal ensemble MC simulations (details in methods section). The radial distribution functions are given in figure 6.4d-f. In all cases the peaks overlap, indicating a good agreement. This is further corroborated by the fact that lattice parameters agree to within 0.3 Å and 2° (see Table 1). Hence, our model is able to correctly reproduce the structure of a self-assembled molecular layer for various intermolecular interaction strengths. Even in the case of previously studied 2,3-naphthalocyanine (**4**) [20], where the electrostatic contribution to the intermolecular interaction is virtually zero, our model correctly reproduces the experimentally observed crystal structure (fig. 6.5a-b). The experimental and simulated radial distribution functions of **4** are shown in figure 6.5c. The peaks overlap, indicating a good agreement. The experimental/theoretical lattice parameters are: $a = b = 16.1/16.6$ Å, $\alpha = 90/90^\circ$, respectively. The difference between experimental and simulated values are somewhat larger than for **1-3**. We tentatively assign this somewhat larger differences to a non-perfect description of the L-J pair potential.

To study the robustness of the model, we investigate the self-assembly of **2** with various values of δ and Δ_L . We varied δ from 0.2 to 0.6 Å and plot the radial distribution function of the resulting crystal (fig. 6.6a). For values of δ smaller than 0.6 Å, the molecules form the close-packed structure. In this regime, an increase in δ results in a small increase in the distance between the molecules. This increase can be rationalized from a decrease in

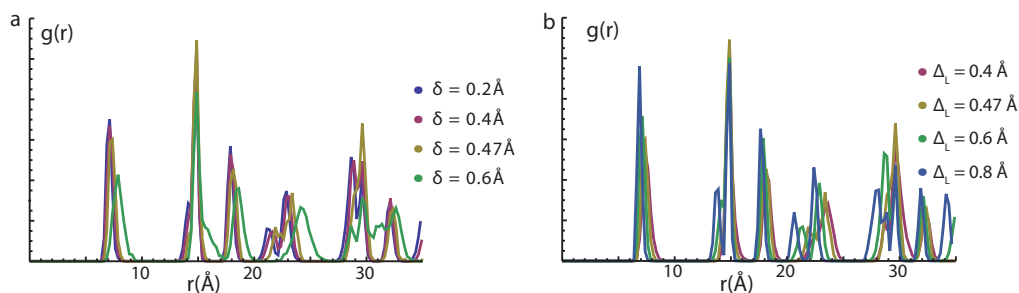


Figure 6.6. The radial distribution of BPCA with varying δ and lone pair distance. a. The radial distribution of **2** for several values of delta. b. The radial distribution of **2** with several distances for the lone pair.

Table 6.1. Lattice parameters of close-packed crystals of **1**, **2** and **3**. Standard deviation for all distances and angles: 0.2 Å and 1°, respectively.

Molecule	Extracted from	Lattice parameters		
		a (Å)	b (Å)	α (°)
1	Experiments	8.1	16.3	51
	Simulations	8.4	16.5	50
2	Experiments	14.6	14.6	30
	Simulations	14.9	14.8	29
3	Experiments	12.3	12.3	32
	Simulations	12.4	12.4	34
4	Experiments	16.1	16.1	90
	Simulations	16.6	16.6	90

the intermolecular interactions (due to a larger distance between the negative charges of one atom and the positive charge of another atom). Above $\delta = 0.6$ Å, the molecules self-assemble into a different crystal structure.

Increasing Δ_L has the same effect as increasing δ : the distance between the molecules increases but the symmetry of the crystal is unaffected (fig. 6.6b). For very small values of Δ_L , there are significant differences in the crystal structure, as evidenced by the different radial distribution function (purple curve in fig. 6.6b). This can be rationalized from the smaller effect of the negative point charge used to model the lone pair at smaller Δ_L . From the observations described above we conclude that the model is robust with respect to small variations in δ and Δ_L .

It is well known that not all stable phases form spontaneously in typical MC simulations. Hence, to investigate the stability of the other experimentally observed crystals for **1** and **2**, we performed simulations in the canonical ensemble where we start with the experimentally observed crystals. If the simulated crystals quickly transform into another crystal or melt into a gas or liquid, then according to the model they are unstable. If they do not

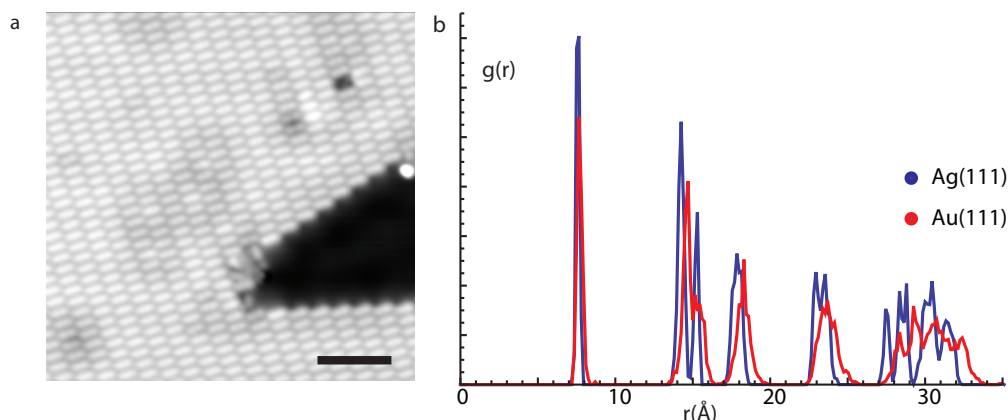


Figure 6.7. Self-assembly of **2** on a Ag(111) surface. a. STM image of self-assembled layer ($V = 0.1$ V, $I = 20$ pA). Scale bar: 5 nm. b. experimental $g(r)$ of **2** on Ag(111) and Au(111).

melt, they are either metastable or stable. Figure 6.4g shows snapshots of these simulations for the honeycomb and square crystal structures of **1** and the fishbone phase of **2** (after 3×10^6 , 3×10^5 , and 3×10^5 cycles, respectively). Simulations were performed using $T = 300$, 250, and 250 K, respectively. In all cases, the crystals are still intact, indicating that they are at least metastable.

To investigate if the model can also be used for molecules on other surfaces, we studied the self-assembly of **2** on Ag(111). In figure 6.7a an STM image of the self-assembled structure of **2** on Ag(111) is shown. As in the case of Au(111), the molecules form a close-packed structure. A comparison of the radial distribution function, $g(r)$, of the self-assembled layer on Ag(111) and Au(111) shows only minor differences (fig. 6.7b). These might be due to changes in the charge distribution in the molecule caused by a stronger molecule-substrate interaction on Ag(111).

6.5 Thermodynamic stability of the observed phases

To determine which structures are fully stable and which are only metastable at $T = 0$ K, we determined the $T = 0$ K phase diagram using a common tangent construction. In a common tangent construction, the Helmholtz free energy per area is plotted as a function of the density. In this representation, phase coexistence corresponds to a pair of densities at which the tangent lines to this curve have both the same slope and the same intercept, corresponding to equal pressure and chemical potential. At zero temperature the Helmholtz free energy is simply equal to the potential energy, i.e. $F = U$. Hence, in figure 6.8a-c we plot the energy per volume of the crystal phases as a function of the density for molecules **1-3**, respectively. We also include a gas phase in these plots. At $T = 0$ K, the gas phase is expected to have a very low density, and the molecules do not interact. Hence, the free energy of the gas phase is $F_{\text{gas}} = U_{\text{gas}} \approx 0$ meV. Both the honeycomb and square structures of **1** are clearly above the common tangent line (fig. 6.8a). Hence, at $T = 0$ K the two structures are metastable in our model and the high density phase is stable. For **2**, the ‘fishbone’ structure is higher in energy than the close-packed structure (fig. 6.8b). It is above the common tangent line, indicating it is also metastable. In contrast, for **3** both the ‘windmill’ crystal and the close-packed crystal are fully stable at $T = 0$ K (fig. 6.8c). This explains why

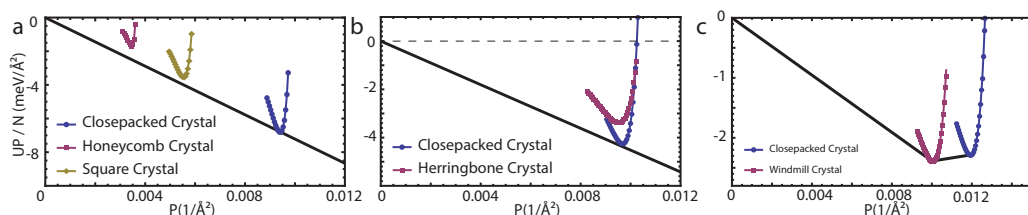


Figure 6.8. Common tangent constructions for 1-3 at $T = 0$ K. a. For 1, the common tangent connects the close-packed crystal with the gas phase. The honeycomb and square phase are located above the line, indicating that they are metastable. b. For 2, the 'fishbone' structure lies above the common tangent line. c. For 3, both crystal structures are connected via the common tangent line, and are therefore stable.

both phases are observed in the canonical NVT simulations: at the density where the NVT simulations shown in figure 6.4c were performed, there is a coexistence of both phases.

6.6 Discussion

It is well known that the electrostatic interaction between a point charge and a conductive surface can be modelled using the method of image charges. To examine the influence of image charges on the self-assembly, we expanded our model as indicated in figure 6.9a. The image charges are located at a distance d_{im} below the molecule. When two atoms interact in the expanded model, not only the interaction between the charges are taken into account but also the interaction between the charges of one atom and the image charges of the other atom. Interactions between image charges are not included. As a starting point for the distance between the image charges, we set it equal to twice the typical adsorption height, which was calculated to be $3.3 - 3.4$ Å on Au(111) (fig. 6.2). Hence, d_{im} should be approximately 6.6 Å. We varied d_{im} between 4 Å and ∞ . The latter corresponds to neglecting image charges (as in the original model). Figure 6.9b shows the radial distribution function for different d_{im} of a close packed layer of 2. The radial distribution functions overlap for all values of d_{im} , demonstrating that image charges have a negligible influence on the self-assembly and can therefore be neglected.

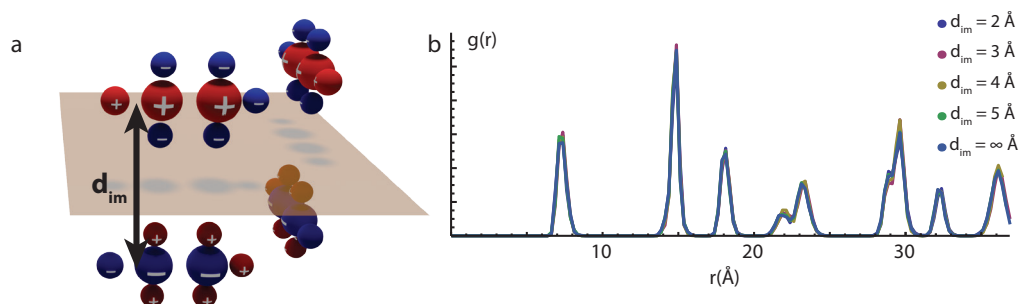


Figure 6.9. Effect of including image charges in the model. a. The images charges are included below the real molecule as opposite point charges. b. The radial distribution function of the close packed structure of 2 calculated at different distances d_{im} . At infinite distance the model is equal to the original model, without image charges.

However, the inclusion of lone pairs in our model is critical to correctly reproduce experimental observations.

6.7 Conclusion

In summary, we have investigated the self-assembly of three molecules with a similar backbone, but with different functional groups on a weakly interacting surface. The intermolecular electrostatic interactions span nearly the entire energy range. A variety of crystal structures are observed. In addition, we developed a simple model that can be used to study the self-assembly of molecules on a weakly interacting surface. The model includes vdW, Pauli, and electrostatic interactions. The model allows us to establish which self-assembled phases are stable and which ones are metastable. We hope that the availability of a predictive model will help to speed up the research of scientists aiming to synthesize and study self-assembled molecular layers with a particular geometry. We believe that it is possible to expand the applicability of the model by including molecule-substrate interactions. For example it should be straight forward to expand the model described here to also include ionic surfaces. An alternative approach is to use potential energy grid files [25,26].

6.8 Methods

Synthesis

Bis-(para-benzoicacid)-acetylene (1) [39]

A catalyst solution was prepared by dissolving $\text{Pd}(\text{OAc})_2$ (23 mg, 0.103 mmol) and tPPTs (342 mg, 0.602 mmol) in degassed H_2O (10 mL) and stirring for 30 min at room temperature (RT), yielding a dark-brown solution. 4-iodobenzoic acid (1.01 g, 4.07 mmol) and 4-ethynylbenzoic acid (0.59 g, 4.03 mmol) were added to 100 mL $\text{H}_2\text{O}/\text{MeCN}$ (1:1) yielding a yellow-orange suspension. K_2CO_3 (2.77 g, 20.09 mmol) was added to the mixture, which was stirred at 50 °C under N_2 . After about 5 min, when a dark orange solution was obtained, a CuI solution (45 mg, 0.24 mmol, in MeCN) and catalyst solution (10 mL) were added, turning the mixture yellow-green. After stirring for an hour, the mixture was allowed to cool to RT. HCl (37%) was added to precipitate the product which after filtering yielded 79.9 mg (7.5% yield) of tan solid. ^1H NMR (400 MHz, d_6 -DMSO): δ =7.96(d, 4H, J_1 = 8.61Hz), 7.68 (d, 4H, J_1 = 8.22Hz). ^{13}C NMR(400 MHz, d_6 -DMSO): δ = 167.06, 132.15, 131.38, 130.03, 126.48, 91.49.

Bis-(para-cyanobenzene)acetylene (2) [28]

A mixture of 4-bromobenzonitrile (1.0026 g, 5.505 mmol), 4-ethynylbenzonitrile (0.67 g, 5.50 mmol), $\text{Pd}(\text{PPh}_3)_2\text{Cl}_2$ (79.1 mg, 0.11 mmol) and PPh_3 (27.2 mg, 0.104 mmol) in dry Et_3N (20 mL) was stirred for 10 min under a N_2 . CuI (38.8 mg, 0.204 mmol) was added and the suspension was heated to 90 °C. The brown-green suspension was stirred for 2 h under reflux. After the mixture had cooled to RT the solvent was removed until a brown solid remained. CHCl_3 (80 mL) was added, and the solution was filtered, washed with a K_2CO_3 solution, water, and brine. After drying over MgSO_4 , the solvent was evaporated to obtain a brown-yellow solid. The product was purified using column chromatography (Silica gel) (DCM/hexane (6:4)). Further purification was done by recrystallization from acetone yielding 319.1 mg (25.4% yield) of yellow needle crystals. ^1H NMR (400 MHz, CDCl_3): δ = 7.66 (d, 4H, J_1 =9.00Hz), 7.61 (d, 4H, J_1 = 8.61 Hz). ^{13}C NMR (400 MHz, CDCl_3): δ = 132.15, 127.05, 118.21, 112.41, 91.52.

Bis-(para-pyridyl)acetylene (3) [30]

Br_2 (1 mL, 17.26 mmol) was slowly added to a stirred solution of 1,2-bis(4-pyridyl)ethylene (1.01 g, 5.53 mmol) in HBr (17 mL, 48%) at 0 °C. The mixture was stirred for 2 h at 120 °C and allowed to cool to RT, before being cooled in ice for 30 min. The resulting suspension was filtered and the residue was washed with cold water and stirred in NaOH (35 mL, 2 M) for 1 h before being filtered again. The residue was dried in vacuo, added to a $t\text{-BuO}^- \text{Na}^+$ solution (60 mL) and left to stir at 80 °C for

4 h. After the mixture was allowed to cool to RT, ethanol (20 mL) and H₂O (20 mL) were added and the resulting orange solution was extracted with CDCl₃ until the extracts were colorless. After the solvent was removed, a dark orange oil was obtained to which CDCl₃ and water were added. The resulting solution was again extracted with CDCl₃ until the extracts were colorless and the solvent was removed to obtain a yellow solid. Purification by silica gel column with a diethyl ether:THF (17:3) eluent yielded 269.4 mg of white solid product (26.9% yield). ¹H NMR (CDCl₃): δ = 8.61 (d, 4H, JHH = 5.09 Hz), 7.37 (d, 4H, JHH = 5.09 Hz), ¹³C NMR (CDCl₃): δ = 149.83, 130.22, 125.57, 90.62.

Monte Carlo

Canonical NVT ensemble

We use two-dimensional MC simulations in the canonical NVT ensemble, e.g. with a fixed number of molecules (N), fixed volume (V), and fixed temperature (T), to study the self-assembly of the molecules. Sampling is performed using the Metropolis algorithm [40]. In the initial configuration the molecules are positioned such that they do not overlap and have a random orientation. Each MC step has a 50/50 change of performing a trial displacement or a trial rotation. The respective step sizes are chosen such that approximately 30% of the attempted MC steps are accepted. The molecular density is chosen low enough that the crystal formed in coexistence with a gas. To avoid boundary effects, periodic boundary conditions are applied in the simulation. Note that a single MC cycle consisted of N MC steps.

Isotension-isothermal NPT simulations

We performed MC simulations in the isobaric – isothermal ensemble, i.e. where the pressure (P) is kept constant instead of the volume (V). The box shape is allowed to fluctuate in order to remove stresses caused by the simulation box geometry [41]. In addition to normal MC translation and rotation moves, we also allow the box volume and shape to fluctuate using trial volume changes. For the initial configuration, the entire box is filled with the crystal found in the NVT simulations. Since the pressure is fixed at zero, these simulations are performed in the isotension-isothermal ensemble.

Distance dependence of the Coulomb interactions for cut-off

Electrostatic forces can be long range in nature. This implies that the energy of a molecule can, in principle, depend on the structure of the material at arbitrarily large distance. In practice, this means that it is not fully safe to cutoff the potential energy at a finite distance and specialized numeric techniques are necessary [41]. In two dimensions, an interaction which is proportional to $r^{-\alpha}$, with

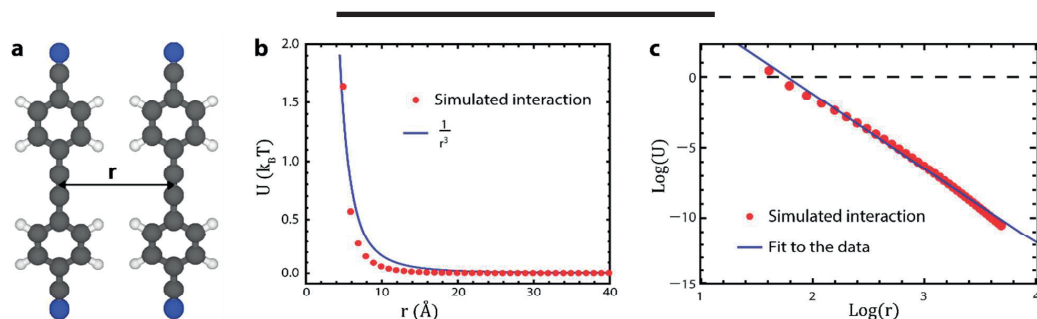


Figure 6.10. Distance dependence of the Coulomb interactions. a. Definition of the lateral distance between two molecules of 2. b. The coulomb interaction between the molecules as a function of distance (red). For comparison a plot of r^{-3} is presented (blue). c. Double logarithmic plot of the energy-distance relationship (red), together with a fit (blue). The slope of the fit (-5.27) indicates that the interaction decays faster than r^{-5} .

α an integer, is considered to be a short range interaction when $\alpha > 2$, while for $\alpha \leq 2$ it is considered a long range interaction [42,43]. The molecules in our model are charge neutral so there is no net monopole-monopole interaction between the molecules. Hence, the interaction between two molecules has overall only dipole (r^{-3}), quadrupole (r^{-5}) and higher order interactions. To verify this, we calculated the energy between two molecules **2** with the same orientation (fig. 6.10a). The calculated Coulomb interaction at different distances is given in figure 6.10b. The interaction between the molecules decays faster than the fitted r^{-3} curve. Figure 6.10c shows a double logarithmic plot of the interaction together with a linear fit. The slope is found to be -5.27 showing that the interaction between the two molecules decays faster than r^{-5} . In our model, we therefore neglected electrostatic forces if the center-to-center distance between a pair of molecules was larger than 30 Å as the potential energy is zero at this distance.

6.9 REFERENCES

- [1] L. Bartels, *Nat. Chem.* **2**, 87 (2010).
- [2] M. O. Blunt, J. C. Russell, N. R. Champness, and P. H. Beton, *Chem. Commun. (Camb)*. **46**, 7157 (2010).
- [3] Y. Yamamoto, H. Nishihara, and K. Aramaki, *J. Electrochem. Soc.* **140**, 436 (1993).
- [4] F. I. Bohrer, C. N. Colesniuc, J. Park, M. E. Ruidiaz, I. K. Schuller, A. C. Kummel, and W. C. Trogler, *J. Am. Chem. Soc.* **131**, 478 (2009).
- [5] W. R. Browne and B. L. Feringa, *Nat. Nanotechnol.* **1**, 25 (2006).
- [6] C. Joachim, J. K. Gimzewski, and A. Aviram, *Nature* **408**, 541 (2000).
- [7] J. V Barth, G. Costantini, and K. Kern, *Nature* **437**, 671 (2005).
- [8] T. A. Pham, F. Song, M.-T. Nguyen, and M. Stöhr, *Chem. Commun.* **50**, 14089 (2014).
- [9] J. Adisoejoso, K. Tahara, S. Lei, P. Szabelski, W. Rzyśko, K. Inukai, M. O. Blunt, Y. Tobe, and S. De Feyter, *ACS Nano* **6**, 897 (2012).
- [10] P. A. Korevaar, S. J. George, A. J. Markvoort, M. M. J. Smulders, P. a. J. Hilbers, A. P. H. J. Schenning, T. F. a. De Greef, and E. W. Meijer, *Nature* **481**, 492 (2012).
- [11] P. A. Korevaar, C. Grenier, A. J. Markvoort, A. P. H. J. Schenning, T. F. A. de Greef, and E. W. Meijer, *Proc. Natl. Acad. Sci. U. S. A.* **110**, 17205 (2013).
- [12] H. Cui, Z. Chen, S. Zhong, K. L. Wooley, and D. J. Pochan, *Science* **317**, 647 (2007).
- [13] M. Müller and D.-W. Sun, *Phys. Rev. Lett.* **111**, 267801 (2013).
- [14] J. Shang, Y. Wang, M. Chen, J. Dai, X. Zhou, J. Kuttner, G. Hilt, X. Shao, J. M. Gottfried, and K. Wu, *Nat. Chem.* **7**, 389 (2015).
- [15] C.-A. Palma, P. Samori, and M. Cecchini, *J. Am. Chem. Soc.* **132**, 17880 (2010).
- [16] N. Martsinovich and A. Troisi, *J. Phys. Chem. C* **114**, 4376 (2010).
- [17] A. G. Slater (née Phillips), P. H. Beton, and N. R. Champness, *Chem. Sci.* **2**, 1440 (2011).
- [18] T. Yokoyama, S. Yokoyama, T. Kamikado, Y. Okuno, and S. Mashiko, *Nature* **413**, 619 (2001).
- [19] J. P. Rabe and S. Buchholz, *Science* **253**, 424 (1991).
- [20] T. A. Pham, F. Song, and M. Stöhr, *Phys. Chem. Chem. Phys.* **16**, 8881 (2014).
- [21] A. Kasperski and P. Szabelski, *Adsorption* **19**, 283 (2012).
- [22] S. Vijayaraghavan, D. Eciya, W. Auwärter, S. Joshi, K. Seufert, M. Drach, D. Nieckarz, P. Szabelski, C. Aurisicchio, D. Bonifazi, and J. V Barth, *Chemistry* **19**, 14143 (2013).
- [23] S. Clair, S. Pons, A. P. Seitsonen, H. Brune, K. Kern, and J. V. Barth, *J. Phys. Chem. B* **108**, 14585 (2004).
- [24] A. Ciesielski, A. R. Stefankiewicz, F. Hanke, M. Persson, J.-M. Lehn, and P. Samori, *Small* **7**, 342 (2011).
- [25] S. Mannsfeld and T. Fritz, *Phys. Rev. B* **69**, 1 (2004).
- [26] S. C. B. Mannsfeld and T. Fritz, *Phys. Rev. B - Condens. Matter Mater. Phys.* **71**, 1 (2005).
- [27] T. J. Roussel, E. Barrena, C. Ocal, and J. Faruado, *Nanoscale* **6**, 7991 (2014).
- [28] O. Berger, A. Kaniti, C. T. van Ba, H. Vial, S. A. Ward, G. A. Biagini, P. G. Bray, and P. M. O'Neill, *ChemMed Chem* **6**, 2094 (2011).
- [29] T. M. Fasina, J. C. Collings, J. M. Burke, A. S. Batsanov, R. M. Ward, D. Albesa-Jove, L. Porres, A. Beeby, J. A. K. Howard, A. J. Scott, W. Clegg, S. W. Watt, C. Viney, and T. B. Marder, *J. Mater. Chem.* **15**, 690 (2005).
- [30] B. J. Coe, J. L. Harries, J. A. Harris, B. S. Brunshwig, S. J. Coles, M. E. Light, and M. B. Hursthouse, *Dalton Trans.* 2935 (2004).
- [31] W.-H. Soe, C. Manzano, A. De Sarkar, N. Chandrasekhar, and C. Joachim, *Phys. Rev. Lett.* **102**, 176102 (2009).
- [32] J. van der Lit, M. P. Boneschanscher, D. Vanmaekelbergh, M. Ijäs, A. Uppstu, M. Ervasti, A. Harju, P. Liljeroth, and I. Swart, *Nat. Commun.* **4**, 2023 (2013).
- [33] G. Kresse and J. Furthmüller, *Phys. Rev. B* **54**, 11169 (1996).

- [34] P. E. Blöchl, *Phys. Rev. B* **50**, 17953 (1994).
- [35] W. D. Cornell, P. Cieplak, C. I. Bayly, I. R. Gould, K. M. Merz, D. M. Ferguson, D. C. Spellmeyer, T. Fox, J. W. Caldwell, and P. A. Kollman, *J. Am. Chem. Soc.* **117**, 5179 (1995).
- [36] C. A. Hunter and J. K. M. Sanders, *J. Am. Chem. Soc.* **112**, 5525 (1990).
- [37] S. L. Price and A. J. Stone, *J. Chem. Phys.* **86**, 2859 (1987).
- [38] C. Fonseca Guerra, J.-W. Handgraaf, E. J. Baerends, and F. M. Bickelhaupt, *J. Comput. Chem.* **25**, 189 (2004).
- [39] H. Dibowski and F. P. Schmidtchen, *Tetrahedron* **51**, 2325 (1995).
- [40] N. Metropolis, A. W. Rosenbluth, M. N. Rosenbluth, A. H. Teller, and E. Teller, *J. Chem. Phys.* **21**, 1087 (1953).
- [41] D. Frenkel and S. Berend, *Understanding Molecular Simulation: From Algorithms to Applications* (2001).
- [42] T. Dauxois, S. Ruffo, E. Arimondo, and M. Wilkens, *Dynamics and Thermodynamics of Systems with Long-Range Interactions* (Springer Berlin Heidelberg, Berlin, Heidelberg, 2002).
- [43] A. Campa, T. Dauxois, T. Dauxois, D. Fanelli, and S. Ruffo, *Physics of Long-Range Interacting Systems* (Oxford University Press, 2014).

7

Summary

Summary

This thesis contains a broad range of topics all of which concern some aspect of AFM and STM. The first part of this thesis describes some fundamental aspects of AFM. Namely, the construction of instrumentation to operate it and the forces covering the contrast formation. In the second part I use the technique to study the geometric and electronic structure of various molecular systems.

The **first** introductory chapter provides an overview of the principles and techniques used throughout this thesis.

The **second** chapter of my thesis describes the fabrication of a new liquid nitrogen (LN_2) tank for the cryostat of our low temperature microscope. Due to limitations in LHe hold time as well as a small leak that presented itself at low temperatures a new LN_2 tank had to be build. Calculations were made to estimate the hold time of the LN_2 and compared to the actual performance after placement. A 50% increase in LN_2 hold time was predicted and achieved though the increased volume of the tank. In addition, the LHe holdtime increased by 16% allowing for longer microscope operation. The manufacturer of the low temperature microscope has expressed interest in commercializing our new LN_2 tank.

The **third** chapter concerns the contrast forming mechanism of sub-molecular AFM. The forces governing the contrast in atomically resolved atomic force microscopy have recently become a topic of intense debate. In this chapter, we show that the electrostatic force is essential to understand the contrast in AFM images of polar molecules. Specifically, we imaged strongly polarized molecules with negatively and positively charged tips. Large differences in the contrast are observed above the polar groups. By taking into account the electrostatic forces between tip and molecule, the observed contrast differences can be reproduced using a molecular mechanics model. We assess the height dependence of the various force components.

In the **fourth** chapter small ribbons made of graphene play a central role. Graphene nanostructures, where quantum confinement opens an energy gap in the band structure, hold promise for future electronic devices. To realize the full potential of these materials, atomic scale control over the contacts to graphene and the graphene nanostructure forming the active part of the device is required. The contacts should have a high transmission and yet not modify the electronic properties of the active region significantly to maintain the potentially exciting physics offered by the nanoscale honeycomb lattice. In this chapter, we show how contacting an atomically well-defined GNR to a metallic lead by a chemical bond via only one atom significantly influences the charge transport through the GNR but does not affect its electronic structure. Specifically, we find that creating well-defined contacts can suppress inelastic transport channels.

In the **fifth** chapter the same graphene ribbons are studied in a different manner since semiconducting GNRs are envisioned to play an important role in future electronics. This requires the GNRs to be placed on a surface where they may become strained. Theory predicts that axial strain, i.e. in-plane bending of the GNR, will cause a change in the band gap of the GNR. This may negatively affect device performance. Using the tip of a STM we controllably bent and buckle atomically well-defined narrow armchair GNR and

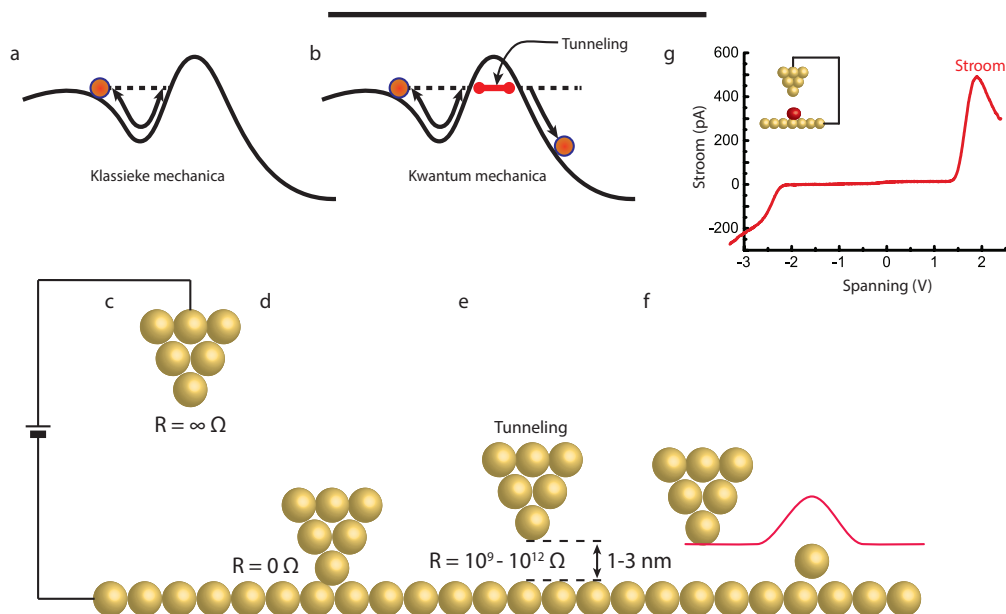
subsequently probed the changes in the LDOS. These experiments show that the band gap of 7-ac-GNR is very robust to in-plane bending and out-of-plane buckling.

The **sixth** chapter describes the self-assembly of molecules on weakly interacting surfaces. If organic molecules are to be used as the active component in devices, self-assembly represents the most attractive route to control the geometric structure and therefore part of the device performance. High-resolution STM measurement combined with DFT and MC calculations are used to study the stability of self-assemblies of molecules with bonding motifs spanning (nearly) the entire range of intermolecular interaction strengths. Our atomistic model reproduces the experimentally observed crystal structures with sub-Ångström precision in all cases. In addition, it is able to identify metastable structures through thermodynamic analysis. This model will allow for a-priori predictions of the structure of molecular self-assemblies on weakly interacting surfaces.

Samenvatting in het Nederlands

De relatie tussen de atomaire structuur en de elektronische eigenschappen van moleculen is van cruciaal belang in de nanowetenschappen en voor toepassingen. In dit proefschrift beschrijf ik het onderzoek dat ik heb gedaan met behulp van twee verschillende technieken: Raster Tunnel Microscopie (RTM, STM in het Engels) en Atomaire Kracht Microscopie (AKM, AFM in het Engels). Deze technieken stelde mij in staat om te kijken naar zowel de atomaire structuur als de elektronische eigenschappen van verschillende moleculen. Door de moleculen op oppervlakken met een zwakke wisselwerking te plaatsen is er een grote kans dat deze eigenschappen niet verstoord worden. Ik zal eerst kort uitleggen wat voor een soort metingen er gedaan kunnen worden met beide microscopen en vervolgens de inhoud van de hoofdstukken in dit proefschrift kort toelichten.

De RTM maakt gebruik van het 'tunneling' principe om 'hoogte' plaatjes te maken van atomaire vlakke kristal oppervlakte. Het tunneling principe is een wet voor extreem lichte deeltjes. Deze wet beschrijft de rare eigenschap van deze deeltjes om door obstakels heen te komen die te hoog zijn. Een simpel voorbeeld hiervan staat in het figuur 7.1. Volgens de klassieke mechanica kan de bal niet over de tweede heuvel in figuur 7.1a rollen. De kwantum mechanica voorspelt echter dat er een kans is dat de zeer lichte bal door de berg heen kan tunnelen (fig 7.1b, rode lijn). Hoe groot de kans is dat de bal door de berg heen komt hangt af van de hoogte en breedte van de berg.



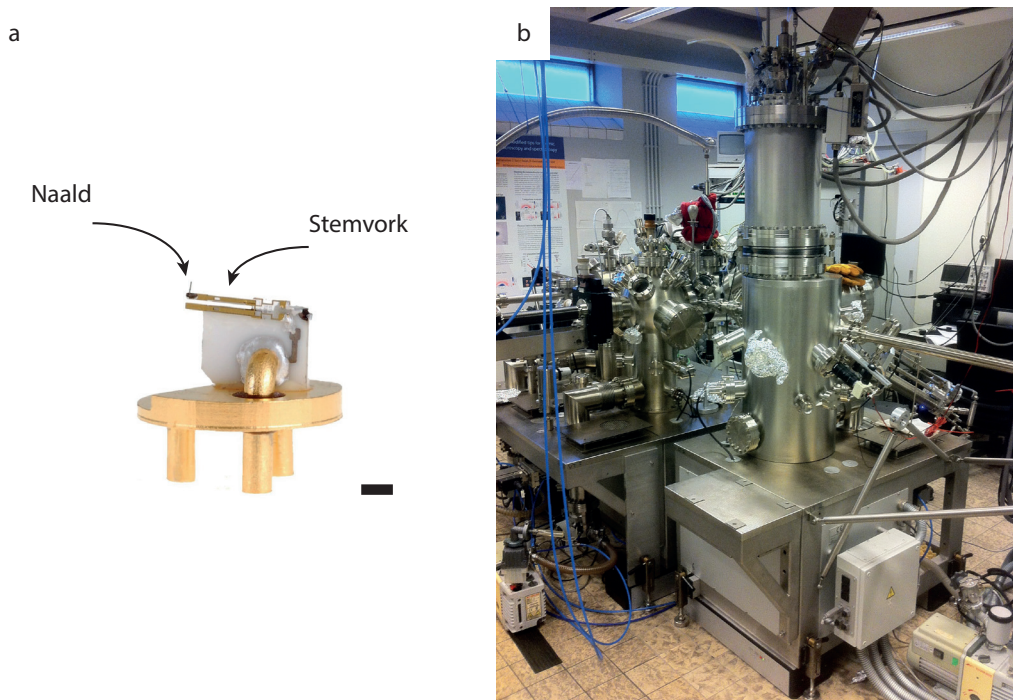
Figuur 7.1 a-b. Verschil tussen klassieke en quantum mechanica. c-e. Weerstand tussen naald en oppervlak bij verschillende afstanden. f. Hoogte profiel van RTM over een enkel adsorbaat bij constante stroom. g. Stroom-Spanning curve boven een molecuul met twee punten van lage weerstand bij -2.2V en +1.5 V.

In het hart van de microscoop wordt een scherpe (vaak van het metaal Wolfram gemaakte) naald naar het metaal oppervlak met daarop het te bestuderen molecuul gebracht. Op de naald staat een kleine spanning ten opzichte van het oppervlak. Wanneer de naald ver van oppervlak is verwijderd zal er geen stroom lopen; met andere woorden, de weerstand tussen de naald en het oppervlak is oneindig groot (fig. 7.1c). Als de naald in fysiek contact is met het oppervlak zal er een hele grote stroom lopen omdat de weerstand door het metaal heel laag is (fig. 7.1d). Echter, vlak voordat de naald fysiek in contact komt met het oppervlak daalt de weerstand heel hard (fig. 7.1e). Dit betekent dat vlak voordat de naald in contact komt er een hele kleine stroom loopt welke sterk afhangt van de afstand tussen de naald en het oppervlak. Deze stroom wordt de tunnelstroom genoemd, omdat hij gebaseerd is op het tunneling principe vanuit de kwantum mechanica. De hoeveelheid stroom die tussen de naald en het oppervlak loopt, is enkele pico-, nanoampère (1 biljoenste/miljardste ampère) bij een afstand van 1-3 nanometer. Door de naald over een oppervlak te rasteren terwijl de stroom constant wordt gehouden kan een afbeelding van het oppervlak verkregen worden. In figuur 7.1f geeft de rode lijn de beweging van de naald aan wanneer hij een obstakel tegenkomt. Een molecule dat op een atomair vlak oppervlak ligt wordt door de RTM waargenomen als een bult.

Wanneer de RTM naald boven een molecuul wordt geplaatst kan de weerstand als functie van de spanning worden gemeten door middel van een stroom-spanningscurve (I-V curve) getoond in figuur 7.1g. Sommige moleculen vertonen een lagere weerstand bij een bepaalde spanning. De elektronen tunnelen op deze spanning door een elektronische toestand van het molecuul. Dit uit zich in een snellere toename van de stroom bij een bepaalde spanning. Deze observatie stelt ons dus in staat om iets te leren over de elektronische eigenschappen van dat molecuul. In mijn proefschrift worden deze I-V metingen Scanning Tunneling Spectroscopie (STS) genoemd omdat ze een spectrum opleveren van de elektronische eigenschappen van een molecule.

De andere techniek waar ik veel gebruik van heb gemaakt is AKM. Deze techniek gebruikt de kracht die een naald, die eindigt in één enkel atoom, ondervindt in de buurt van een oppervlak. Deze kracht kan gebruikt worden om de afstand tot het oppervlak te controleren net als de tunnel stroom in RTM. Een scherpe naald wordt bevestigd aan het eind van een hele kleine stemvork (figuur 7.2a). Wanneer de stemvork wordt aangeslagen zal de naald samen met de armen van de stemvork gaan trillen. De frequentie van deze trilling is bepaald door de stemvork (eigen-frequentie). De beweging die de naald maakt is altijd van/naar het oppervlak. Wanneer de naald ver van het oppervlak is ondervindt zij geen enkele kracht en zal de stemvork trillen op zijn eigen-frequentie. Wanneer de naald heel dicht bij het oppervlak is kan het zijn dat de naald en het oppervlak elkaar gaan aantrekken of juist afstoten. Hierdoor zal de frequentie van de aangeslagen stemvork afnemen (bij aantrekking) of juist toenemen (bij afstoting) t.o.v. zijn eigen frequentie. Deze verandering in eigen-frequentie wordt gemeten en kan worden gebruikt om de afstand tussen naald en oppervlak constant te houden. Het eindresultaat van een AKM meting is een hoogteplaatje van een oppervlak, maar nu op basis van de kracht tussen de naald en het oppervlak. Het voordeel van AKM ten opzichte van RTM is dat het te onderzoeken oppervlak niet elektrisch geleidend hoeft te zijn.

In mijn proefschrift gebruik ik AKM om de atomaire structuur van moleculen te meten. Hiervoor moet ik (het verschil in) krachten heel dicht bij de moleculen meten. Wanneer ik dat met een naald zou doen die eindigt met een metaal atoom springen de moleculen snel naar de naald. De reden hiervoor is dat een schone metaal naald heel reactief is; met andere



Figuur 7.2. AKM sensor van het qPlus type. Schaalaanduiding $\sim 1\text{mm}$. b. UHV opstelling in Ornstein Laboratorium met lage temperatuur microscoop op de voorgrond.

woorden hij wil graag een binding vormen met andere atomen. De truc die wij gebruiken is de naald te laten eindigen met één enkel koolmonoxide molecuul. Deze wordt precies op het punt van de naald geplaatst. Hiervan wordt zij niet alleen scherper maar duwt zij ook geen moleculen meer weg.

Om het mogelijk te maken om individuele moleculen te bestuderen op een schoon en atomair vlak kristal oppervlak maak ik voor al mijn werk gebruik van een Ultra Hoog Vacuüm (UHV) opstelling. Wanneer een schoon oppervlak aan de buitenlucht blootgesteld zou worden is het al na 1 nanoseconde bedekt met een laag moleculen (voornamelijk water en zuurstof uit de lucht). Door in UHV te werken kan deze tijd worden verlengd tot enkele weken. De druk in ons vacuüm systeem is ongeveer 10^{-10} mbar, een 10 biljoenste van de atmosferische druk. Om te zorgen dat alle moleculen ook stil blijven liggen op een oppervlak koelen wij dit tot 5 graden boven het absolute nulpunt. Dit komt neer op -268 graden Celsius, het kookpunt van vloeibaar helium. Een foto van de huidige opstelling staat in figuur 7.2b.

In het eerste hoofdstuk van dit proefschrift geef ik een uitgebreide introductie van alle bovengenoemde technieken. Ik ga verder in op contrastvormingsmechanisme van AKM, als introductie voor het onderzoek beschreven in hoofdstuk 3.

Hoofdstuk 2 beschrijft het ontwerp, de bouw en het testen van een nieuwe vloeibare stikstof tank voor de helium cryostaat van onze lage temperatuur microscoop. De cryostaat,

die het koelvermogen levert aan de machine, bestaat uit een binnentank gevuld met vloeibaar helium (-268°C) en een buitentank gevuld met vloeibaar stikstof (-195°C). Deze nieuwe stikstoftank is groter dan de originele waardoor de binnentank minder vaak gevuld dient te worden. Daarnaast verving deze tank de oude lekkende tank. Inmiddels is ook de fabrikant van de lage temperatuur microscoop geïnteresseerd in het ontwerp van deze tank.

Hoofdstuk 3 beschrijft onderzoek dat ik heb gedaan om een beter begrip te krijgen op het contrastvormingsmechanisme van atomaire resolutie AKM. Met name heb ik gekeken naar de invloed van elektrostatische krachten op het contrast. Elektrostatische krachten zijn krachten tussen geladen deeltjes en kunnen aantrekkend of afstotend zijn. Door onze AKM metingen te vergelijken met simpele berekeningen hebben we verschillende contrastkenmerken kunnen toeschrijven aan deze kracht.

Hoofdstuk 4 beschrijft onderzoek dat gedaan is op hele smalle linten van grafeen. Grafeen bestaat uit een enkele laag koolstofatomen in een honingraat geometrie. Grafeen is een veelbelovend materiaal voor toekomstige elektronica omdat het heel goed stroom geleidt. Wanneer het in dunne linten wordt gegroeid wordt het plots halfgeleidend. De stroken die ik onderzocht heb zijn exact 7 koolstofatomen breed en vertonen een bijzondere elektronische toestand aan hun uiteinde. Ik heb veranderingen in deze elektronische toestand bestudeerd nadat één van de uiteinden chemisch gebonden werd aan een goud oppervlak met behulp van een stroompuls.

In Hoofdstuk 5 worden dezelfde grafeen linten gebruikt als in hoofdstuk 4. In dit hoofdstuk bekijken we of het ombuigen van deze stroken (mechanische spanning) een effect heeft op de elektronische eigenschappen van de stroken. De naald van de RTM wordt gebruikt om de stroken op verschillende manieren om te buigen. De gemeten verschillen in elektronische eigenschappen zijn klein. Dit is belangrijk omdat dergelijke stroken in de toekomst bijvoorbeeld gebruikt kunnen worden in elektronische circuits waar altijd enige vervorming optreedt.

Hoofdstuk 6 beschrijft een methode om te voorspellen hoe moleculen op een oppervlakte ten opzichte van elkaar zullen gaan liggen. Dit proces van zelf-assemblage is belangrijk voor toepassingen waar reeksen moleculen op een goed gedefinieerde manier moeten liggen. Met behulp van een computermodel kunnen we de supra-moleculaire structuren voorspellen. Er kan zelfs een idee gevormd worden over de relatieve stabiliteit van verschillende moleculaire structuren.

List of Publications

This thesis is based on the following publications:

- J. van der Lit, F. Di Cicco, P. Hapala, P. Jelinek, I. Swart, Sub-Molecular resolution of molecules by AFM: The influence of the electrostatic force, *Physical Review Letters*, *accepted*, 2016
- J. van der Lit, J. L. Marsman, R. S. Koster, P. H. Jacobse, S. A. den Hartog, N. J. van der Heijden, D. Vanmaekelbergh, R. J.M. Klein Gebbink, L. Filion, I. Swart, Modelling the Self-Assembly of Organic Molecules on Weakly Interacting Surfaces, *Journal of Physical Chemistry C*, 17, 052013, 2015
- J. van der Lit, P.H. Jacobse, D. Vanmaekelbergh, I. Swart, Bending and Buckling of Narrow Armchair Graphene Nanoribbons via STM manipulation, *New Journal of Physics*, 17, 053013, 2015
- J. van der Lit, M. P. Boneschanscher, D. Vanmaekelbergh, M. Ijäs, A. Uppstu, M. Ervasti, A. Harju, P. Liljeroth, I. Swart, Suppression of electron-vibron coupling in graphene nanoribbons contacted via a single atom, *Nature Communications*, 4, 2023, 2013

Other publications by the author:

- W. van der Stam, F. Rabouw, J. Geuchies, A. Berends, S. Hinterding, R. Geitenbeek, J. van der Lit, S. Prévost, A. Petukhov, C. de Mello Donegá, Formation of Ultrathin 2D Cu_{2-x}S Nanosheets Studied by In-situ Small-Angle X-ray Scattering, *submitted*
- N. J. van der Heijden, P. Hapala, J. A. Rombouts, J. van der Lit, D. Smith, P. Mutombo, M. Švec, P. Jelinek, I. Swart, Chemical Recognition of Organic Molecules using Atomic Force Microscopy, *submitted*
- P. Hapala, M. Švec, O. Stetsovych, J. van der Lit, N.J. van der Heijden, M. Ondráček, P. Mutombo, I. Swart, P. Jelínek, Reconstructing the electrostatic field of molecules from high-resolution scanning probe images, *submitted*.
- S. K. Hämäläinen, N. J. van der Heijden, J. van der Lit, S. A. den Hartog, P. Liljeroth, I. Swart, Intermolecular contrast in atomic force microscopy images without intermolecular bonds, *Physical Review Letters*, 113, 186102, 2014
- A. Boerke, J. van der Lit, F. Lolicato, T. A. E. Stout, J. B. Helms, B. M. Gadella, Removal of GPI-anchored membrane proteins causes clustering of lipid microdomains in the apical head area of porcine sperm, *Theriogenology*, 81, 613, 2014
- M. Ijäs, M. Ervasti, A. Uppstu, P. Liljeroth, J. van der Lit, I. Swart, A. Harju, Electronic states in finite graphene nanoribbons: Effect of charging and defects, *Physical Review B*, 88, 075429, 2013
- M. P. Boneschanscher, J. van der Lit, Z. Sun, I. Swart, P. Liljeroth, D. Vanmaekelbergh, Quantitative atomic resolution force imaging on epitaxial graphene with reactive and nonreactive AFM probes, *ACS Nano*, 11, 10216, 2012

List of Presentations

Jan 2013	Graphene nanoribbons, Can one atom make the difference? Physics@FOM 2013, Veldhoven, The Netherlands (oral)
Mar 2013	Graphene nanoribbons, Can one atom make the difference? DPG-Frühjahrstagung 2013, Regensburg, Germany (oral)
Apr 2013	Graphene nanoribbons, Can one atom make the difference? Dutch SPM day 2013, Eindhoven, The Netherlands (oral)
May 2013	Graphene nanoribbons, Can one atom make the difference? Graphene day 2013, Utrecht, The Netherlands (oral)
Sep 2013	Graphene nanoribbons, Can one atom make the difference? Debye lunch lecture, Utrecht, The Netherlands (oral)
Aug 2013	Suppression of electron-vibron coupling in graphene nanoribbons contacted via a single atom nc-afm summerschool, Porquerolles, France (poster) Prize for best presentation
Dec 2013	Graphene nanoribbons CBN meeting 2013, Regensburg, Germany (invited oral)
July 2014	Modifying the Electronic Properties of Atomically Well-Defined GrapheneNanoribbons by Inducing Strain ICN+T, Vail, USA (oral)
Mar 2015	A predictive model for the self-assembly of organic molecules on weakly interacting surfaces DPG-Frühjahrstagung 2015, Berlin, Germany (oral)
Aug 2015	Sub-molecular contrast: Pauli vs Coulomb nc-afm 2015, Cassis, France (oral)
Jan 2016	Sub-molecular contrast: Pauli vs Coulomb Physics@FOM 2016, Veldhoven, The Netherlands (oral)

Acknowledgements

Het is gedaan. It is done. Welcome at the end. It has been a wonderful experience over the past four years and I would like to thank some of the many people who have helped me along the way.

Ingmar, baas, een betere begeleider had ik niet kunnen wensen. Jouw kennis en persoonlijke betrokkenheid maakte mijn promotie tot een fantastische tijd. Je deur stond altijd open voor een gesprek en een grap. Jij hebt mij geleerd structuur aan te brengen in mijn werk. Hoe jij overleeft als wetenschapper zonder koffie te drinken, is mijn nog steeds een raadsel. Ik vind het een eer om jou eerste aio geweest te zijn. **Daniël**, jouw wetenschappelijk inzicht, interesse in mijn werk en vermogen om tijdens een goede meting altijd even in de kelder te komen kijken (zolang je maar niets aanraakt), waardeer ik enorm. Onze gedeelde passie voor curries bij de Taj Mahal heeft geleid tot veel gezellige avonden. **Hans**, bedankt voor de koffie en een gezellig praatje iedere ochtend (behalve vrijdag). Veel van de technische kennis die ik de afgelopen vier jaar heb opgedaan, heb ik aan jou te danken. Jouw tijd zit er ook bijna op, veel plezier met alle vrije tijd die je te wachten staat. **Peter Liljeroth**, your willingness to take me on as a Master's student that could work on the machine in Utrecht while you were in Helsinki was a win-win situation. I enjoyed the weeks in Helsinki working on your machines and all our joined projects.

I would also like to thank my collaborators who have helped to make my research a success. Grown-up DFT from Finland provided by the group of **Ari Harju** and the AFMulator calculations done in both the group of **Pavel Jelinek** in Prague and (again) in Finland. Especially, I would like to thank **Prokop** and **Sampsä** for all their work and discussions about the model. **Laura** en **Jolien** van de SCM groep wil ik bedanken voor hun samenwerking in de (bijna) eindeloze race om ons paper af te krijgen. De OCC groep, met name **Emma**, wil ik bedanken voor de beschikbare zuurkast en al alle hulp als ik weer eens proefjes kwam doen.

Weinig mensen die floreren op een continue stroom *Sultans of Swing* en *Cut your Teeth*. **Herman**, **Ward** en **Fredje**, we hebben gelachen en gehuild. Spareribs, casino, pokon en wetenschap, onze werkkamer was een vruchtbare plek. Dank voor alle gezelligheid. **Jaco**, als harde werker heb jij het verdiend om nu ook in OL158 te zitten. Zorg goed voor Herman en veel succes met jouw promotie. **Mark**, jij hebt mij geïntroduceerd in de basement-way van onderzoek doen. Jouw kennis en kunde gaven mij een vliegende start in het lab. **Nadine**, jouw enthousiasme op het lab waardeer ik enorm. Jouw eerste klus als aio was het lab toegankelijk maken voor mensen kleiner dan 1.70m, nu is het bijna ondenkbaar dat langere mensen er nog kunnen werken. Dank dat je mijn paranimf wil zijn en veel succes met jouw promotie. De rest van de basement boys en girls: **Marlou**, **Petertje**, bedankt voor de samenwerking. Beide waren jullie eerst (mijn) student en nu aio, veel succes. Ook mijn andere studenten, **Stephan** and **Francesca**, both of you have contributed to this thesis. It

even resulted in your names on different publications. In both cases the work was not your main topic of your project, which makes it even better.

The CMI group is one of the few chemistry groups I had not done any work at during my studies. I'm very happy I saved the best for last. I would like to thank all my colleagues, **Robin, Anne, Relinde, Maryam, Annalisa, Federico, Joep, Mathijs, Chenghui, Allen, Winston, Chun Che, Tim, Carlo, Elleke, Andries, Joop, Harold and Onno** for all the fun times. Zonder assistentie vanuit de technische werkplaats zou mijn onderzoek onmogelijk zijn geweest. **Marcel, Manfred en Gerard** bedankt voor jullie inzet wanneer er weer iets "vandaag, liever gister" klaar moest. '**Grote**' **Stephan** bedankt voor de introductie in Python en het creëren van de Python/Matrix verbinding.

Iedere vrijdag was het om vijf uur (soms eerder) 'Prime Time'. De beste remedie om je trubbels te vergeten, bier en een worst/kaas scenario. De lange lijst van mensen in de Whatsapp groep: **Ammie, Frank, Bienneke, Chris, Paul, Janne-Mieke, Tim, Lil, Nikki, Petor, Winnie, Tiemen, Timo, Marjon, Laurens, Alen, Arjan, Robin, Remi, Arno en Jeroen**: Bedankt voor alle gezelligheid in de kroeg, op feestjes of festivals! **Petor**, het is jammer dat je nu helemaal in Deutschland zit, maar ik vind het heel fijn dat je mijn paranimf wilt zijn. Onze gedeelde passie voor het bierbrouwen heeft ons veel plezierige zondagen gebracht. Mocht het niks worden met de Wissenschaft kunnen we altijd nog een brouwerij starten. **Jeroen**, bedankt voor alle lol die we tijdens onze opleiding samen hebben gehad. Als 'partner-in-crime' of als getuige, ik ben blij dat jij er altijd bent met goed advies! Onze wens voor een gedeelde publicatie is gelukkig werkelijkheid geworden. **Paul en Frank** onze skwasj sessies waren een goed begin van de dag. **Timo**, onze receptuur voor de heartstopper heeft zich in de jaren geperfectioneerd. Samen Star Trek (OS) kijken maakt onze avonden nog steeds tot een succes. **Victor, Matthia, Hilde en Matti en Sylvester** heel erg bedankt voor de fantastische weekendjes weg en alle gezelligheid die we met elkaar hebben.

Dick, Annelies, Ernst en Nancy, het is fijn om zo'n lieve schoonfamilie te hebben. Ouders, broers, aanhang, Opa en Oma, jullie fysieke bijdrage aan dit proefschrift is moeilijk aan te wijzen. Ik ben jullie allemaal erg dankbaar voor alle leuke tijden die we samen hebben. **Pa en Ma**, het is heerlijk dat er altijd een bordje bloemkool met een balletje klaarstaat als ik kom eten! **Daan, Thijs en Thomas, Kirsten, Tanja, Opa Harry en Oma Elly** bedankt voor jullie steun tijdens mijn opleiding en interesse in mijn werk.

Tot slot, mijn allerliefste **Els**, Vrouw! Het beste plekje in mijn proefschrift is voor jou. Het is onmogelijk om alles wat jij voor mij betekent te vangen in één alinea. Jouw hulp tijdens mijn promotie was onmisbaar, of het nou ging om het nakijken van mijn teksten of het vullen van '*de baby*'. Jij bent er altijd voor mij en ik hoop er nog heeeeeeel lang voor jou te zijn! Ik hou van jou..... tot in de blubber.

Curriculum Vitae

Joost van der Lit was born in Bilthoven on the 21th of March in 1986. In 2004 he graduated from the St. Gregorius College in Utrecht and started his Chemistry studies at the University of Utrecht. During his studies he spend 6 months travelling Australia and New Zealand and one year as treasurer of the Utrechtse Scheikunde Studentenvereniging 'Proton'. After obtaining his bachelor degree in 2009 he followed the Master's programme Nanomaterials: Chemistry and Physics. His thesis research entitled "Oxidative cleavage of fatty-acids using Fe based catalysts" and literature study entitled "Surface Synthesis in UHV" were performed in the Organic Chemistry and Catalysis group.

In 2012 Joost started his PhD project at the Condensed Matter and Interface group under the supervision of Daniel Vanmaekelbergh and Ingmar Swart. The main results of his work are described in this thesis, have been published in peer-reviewed journals and have been presented at (inter)national conferences. During his PhD he supervised three Master's students and two bachelor courses.

Next to spending every Friday evening in cafe Jan Primus with friends, Joost enjoys brewing his own beer.

And he makes it fast with one more thing
'We are the Sultans... We are the Sultans of Swing'

